DISS. ETH NO. 22622

Quantum Harmonic Oscillator State Synthesis by Reservoir Engineering

A thesis submitted to attain the degree of

DOCTOR OF SCIENCE of ETH ZÜRICH

(Dr. sc. ETH ZÜRICH)

presented by

DANIEL KIENZLER

Dipl. Phys., Humboldt Universität zu Berlin

born on 19.03.1983

citizen of
Germany

Accepted on the recommendation of

Prof. Dr. J. P. Home
Dr. D. M. Lucas
Prof. Dr. J. Faist

2015

Abstract

This thesis describes novel experiments on the dissipative preparation of harmonic oscillator state superpositions, their analysis and subsequent manipulation with unique spin-oscillator couplings. In addition I describe the setup of a trapped ion experiment together with the design and fabrication process of a segmented ion trap.

Following the proposals [CPBZ93, PCZ96] we prepare superpositions of energy eigenstates of the motion of a trapped $^{40}Ca^{+}$ ion by environment engineering. The process is implemented by artificial dissipation in form of an effective zero temperature bath combined with tailored spin-oscillator couplings. Using this technique we create coherent, squeezed and displaced-squeezed states of motion.
From the structure of the coherent couplings used in the environment engineering we devise novel spin-oscillator couplings, which operate directly in the eigenbasis of the prepared states. These are used to analyze the prepared states, enabling a phase sensitive measurement. This allows us to give a lower bound on the fidelities of the created states with a fidelity of 0.90(2) for a coherent state with a displacement of $|\alpha| = 2.00(1)$ and a fidelity of 0.88(2) for a vacuum squeezed state with squeezing amplitude of $r = 1.45(3)$ [KLK^{+}15].
The novel couplings were used further to manipulate the created states. With this squeezed number states ($r = 1.2(1)$) up to the fourth excited state and a superposition state of the squeezed ground state and second excited squeezed number state were created.
An additional analysis of the prepared squeezed vacuum states based on a spin-state dependent force was implemented. This allowed us to directly measure the phase and quadratures of the squeezed state and led to the creation of 'squeezed Schrödinger's cat' states [LKdC^{+}15, Lo].

The ion trap built as part of this thesis was designed to trap linear mixed species ion crystals composed of $^{40}Ca^{+}$ and $^{9}Be^{+}$ ions. It features two optimized zones for shuttling and separating ion strings, which connect three zones for manipulation of the ions by laser beams. Segmented bias electrodes close to the trap serve to compensate electrical stray fields optimally in all zones of the trap. The heating rate for a single $^{40}Ca^{+}$ ion at an axial trap frequency of $2\pi \times 2\,\mathrm{MHz}$ was measured to be 10 quanta/s.

This is the second edition of the thesis, released on Wednesday 13$^{\mathrm{th}}$ May, 2015, with minor correction. The first edition of the thesis was released on Sunday 8$^{\mathrm{th}}$ March, 2015, which was the basis of the doctoral defense.

Zusammenfassung

Die hier vorgelegte Abhandlung beschreibt Experimente zur dissipativen Preparation von Superpostitionszuständen des harmonischen Oszillators sowie deren Analyse und Manipulation durch einzigartige Spin-Oszillator Kopplungen. Des Weiteren beschreibe ich den experimentellen Aufbau eines Ionen-Fallen-Experiments sowie das Design und den Fabrikations-Prozess einer segmentierten Ionen-Falle.

Den Ansätzen von [CPBZ93, PCZ96] folgend, prepariere wir Superpositionszustände der Energie-Eigenzustände der Bewegung eines gefangenen $^{40}Ca^{+}$ Ions durch 'Environment Engineering'. Diese Technik wird umgesetzt durch eine künstliche Dissipation in Form eines Null-Temperatur Bades kombiniert mit speziell angepassten Spin-Oszillator Kopplungen. Wir verwenden diese Technik um kohärente, gequetschte und versetzt-gequetschte Bewegungszustände zu erzeugen.
Aus der Struktur der kohärenten Kopplungen die im 'Environment Engineering' Anwendung finden, leiten wir neuartige Spin-Oszillator Kopplungen ab, die direkt in der Eigenbasis der präparierten Zustände agieren. Wir verwenden diese Kopplungen um die präparierten Zustände zu analysieren, was uns eine phasensensitive Messung ermöglicht. Dies erlaubt uns eine untere Grenze für die Güte der von uns präparierten Zustände anzugeben. Für einen kohärenten Zustand mit einem Versatz von $|\alpha| = 2.00(1)$ messen wir eine Güte von 0.90(2). Für einen gequetschten Zustand mit einer Quetsch-Amplitude von $r = 1.45(3)$ messen wir eine Güte von 0.88(2) [KLK^{+}15].
Des Weiteren verwenden wir die neuartigen Kopplungen um die präparierten Zustände zu manipulieren. Mit einem gequetschten Vakuum-Zustand als Startpunkt erzeugen wir angeregte Zustände bis zum vierten gequetschten Nummerzustand und einen Superpositionszustand aus dem gequetschten Vakuumzustand und dem ersten angeregten gequetschten Nummerzustand.
Eine zusätzliche Analyse speziell für die gequetschen Vakuumzustände wurde umgesetzt. Diese ermöglicht eine direkte Messung der Phase und der Quadraturen eines gequetschen Zustandes und erzeugt neuartige 'gequetsche Schrödinger's Katze'-Zustände [LKdC^{+}15, Lo].

Als Teil dieser Arbeit wurde eine Ionenfalle gefertigt. Sie wurde designt um lineare Ionen-Kristalle zu fangen, die aus $^{40}Ca^{+}$ und $^{9}Be^{+}$ Ionen bestehen. Die Falle besitzt zwei Zonen die für das Bewegen und Spalten von Ionen-Ketten optimiert wurden. Diese verbinden drei Zonen zur Manipulation der Ionen mit Laserstrahlen. Segmentierte Kompensationselektroden nahe der Falle dienen der optimalen Kompensation von elektrischen Streufeldern in allen Zonen der Falle. Die gemessene Heizrate der Falle für ein einzelnes $^{40}Ca^{+}$ Ion mit einer axialen Fallenfrequenz von $2\pi \times 2\,\mathrm{MHz}$ beträgt 10 Quanten/s.

Acknowledgements

I would like to thank:
The whole TIQI group. All work presented in this thesis would not have been possible without the contributions from every, past and present, group member. It has been a most exciting time with a lot of fun in and around the lab.

Jonathan Home for his constant support throughout this work, his ability to inspire and fascinate for the work we are doing. For getting me through a tough but most rewarding beginning of building the trap, the vacuum system, the lasers, the new labs (and air-conditioning system), the month of loading and a lot more. And also for getting me go further than I would have been able alone, greatly improving my work.
Ben Keitch, for his support over the years, working on the control-system, a major part of our experiment. For his knowledge about (rf) electronics, that helped to prevent so many blunders.
Hsiang-Yu Lo who has dedicated much of his time to our laser systems and spent long nights in the lab working on our experiments.
Frieder Lindenfelser who worked for his Master's thesis on our stabilization cavities and the calcium laser setup, for building the first set of beryllium ovens for our setup and for proof-reading most parts of this thesis.
Florian Leupold who continued working on our stabilization cavities, getting everything ready for us to load our trap.
Ludwig de Clercq, his infamous EVIL, which made life in the lab more fun, but also much easier. And of course his new DAC system, which shall not be named here.
Vlad Negnevitsky, his work on the EVIL and his major impact on the DDS system.
Joseba Alonso for useful discussions about almost everything we did in the lab, and working with us on loading beryllium.
The contribution of the Masters students to this project: Martin Sepiol as the first Masters student I supervised (may he forgive me), followed by Karin Fisher and Christa Flühmann.
Matteo Marinelli, who first simulated the dissipative state preparation and set up the quantum-Monte Carlo code.
Our past and present secretaries Lisa Artel and Mirjam Bruttin. Without them nothing would have worked. Nothing.
Dominik Wild, who tested our first calcium ovens.
Roland Habluetzel, who put an amazing coil-winder for beryllium ovens to work, making this horrible task so much easier. And who tested the beryllium ovens.
Martin Paesold, who has worked with us in the beginnings and made a laser-safety sign, which was finally put on the lab door last week.
Mario Rusev, who worked on the control system in the early days.
The mechanical workshop, who made an uncountable number of parts, many of them on short notice.
The Esslinger group who helped us out time and again with optics and more.

David Lucas from the Oxford ion trapping group sharing some of his long experience in ion trapping with us, especially while trying to load calcium for the first time. Also for examining this thesis and pointing out many mistakes to me.

Peter Krüger, Lucia Hackermüller and Igor Lesanovsky for teaching me in Nottingham about cold atoms, lasers, vacuum and quantum physics, which all proved to be extremely helpful in Zürich.

Contents

1 Introduction **1**
- 1.1 Quantum Information . . . 2
- 1.2 Quantum Computing . . . 4
- 1.3 Dissipation as an Obstacle . . . 5
- 1.4 Dissipation as a Resource . . . 5
- 1.5 This work . . . 6

2 Theoretical Description **9**
- 2.1 The Calcium Ion . . . 9
- 2.2 The Beryllium Ion . . . 10
- 2.3 Paul Trap . . . 11
  - 2.3.1 Pseudopotential Approximation . . . 12
  - 2.3.2 Micromotion . . . 14
- 2.4 Trapped Ion Quantum Physics . . . 17
  - 2.4.1 Coherent Interaction . . . 19
  - 2.4.2 Dissipation, Master Equation . . . 21
- 2.5 Dissipative State Preparation . . . 24
  - 2.5.1 Ground State Cooling . . . 25
  - 2.5.2 Displaced Squeezed State Cooling . . . 25
  - 2.5.3 Generalized Fock State Ladders . . . 27

3 Apparatus **29**
- 3.1 General Design Considerations . . . 29
- 3.2 Trap . . . 30
  - 3.2.1 Trap Simulation . . . 31
  - 3.2.2 Trap Design . . . 36
  - 3.2.3 Fabrication . . . 40
- 3.3 UHV Chamber and Surroundings . . . 46
  - 3.3.1 Trap mount and Atomic Source Ovens . . . 46
  - 3.3.2 UHV Chamber . . . 48

3.3.3 Imaging System . . . 55
3.3.4 Resonators . . . 56
3.3.5 Magnetic Field Coils . . . 59
3.4 Laser Setup . . . 61
3.4.1 Laser Light Sources . . . 61
3.4.2 Beam Delivery . . . 69
3.5 Computer Control . . . 71

4 Experimental Techniques and Characterization Measurements 75
4.1 $^{40}Ca^{+}$ Dipole Transitions at 119 Gauss . . . 75
4.2 Ion Loading . . . 76
4.3 Experimental Sequence . . . 78
4.3.1 Doppler Cooling . . . 78
4.3.2 Internal State preparation . . . 80
4.3.3 Resolved Motional Sideband Cooling . . . 80
4.3.4 Fluorescence Detection . . . 83
4.4 Micromotion Compensation . . . 85
4.5 Spin Coherence . . . 87
4.6 Heating Rate . . . 90
4.7 Motional Coherence . . . 91
4.8 Trapping Potentials . . . 93

5 Environment Engineering 95
5.1 Implementation of the Pumping Technique . . . 95
5.1.1 Coherent Manipulations . . . 96
5.1.2 Optical Pumping . . . 99
5.2 Analysis of Prepared States . . . 100
5.2.1 Steady/Dark state . . . 100
5.2.2 Energy Eigenstate Analysis . . . 100
5.2.3 Analysis in the Engineered Basis . . . 101
5.2.4 Fits to Rabi oscillation data . . . 106
5.2.5 Limits to the Squeezed State Size . . . 107
5.2.6 Squeezed States - Further Discussion . . . 110
5.2.7 Analysis of the States using a Spin-State Dependent Force 111

6 Control in the Engineered Basis 115
6.1 Ladder states . . . 115
6.2 Superposition state . . . 116

7 Summary and Outlook 121
7.1 Summary . . . 121
7.2 Outlook . . . 123
7.2.1 Determination of the Wigner Function by Measurement in the Displaced Number State Basis . . . 123

7.2.2 Engineering Multiple Reservoirs 124
7.2.3 Coupling of a Quantum System to a Reservoir 127
7.2.4 Nitrogen Cooling of the Trap 128

A Appendix **129**
A.1 Abbreviations 129

Bibliography **131**

Chapter 1

Introduction

Quantum physics has been a greatly successful theory, explaining phenomena where classical physics failed, thus extending our understanding of nature but also catalysing a vast number of technological inventions. The quantum revolution started with the groundbreaking work of M. Planck in 1900, who postulated energy-'quanta' to introduce the Planck-law describing the spectrum of black body radiation and A. Einstein generalizing Planck's concept and using these energy-'quanta' to explain the photo-electric effect. This lead in the 1920s to the development of a full theory of quantum mechanics. The experiments at that time were performed on ensembles of particles, always measuring many quantum states at once. A technological revolution followed, and devices using emergent phenomena from quantum physics were invented.

Today researchers work towards a second technological jump. Devices are constructed that use quantum states and their properties directly rather than emergent phenomena. A foundation was laid by experiments performed in the 1970s and 1980s by Serge Haroche and David J. Wineland among others. Both received the Nobel Price in 2012 'for ground-breaking experimental methods that enable measuring and manipulation of individual quantum systems' [Nob12]. These experiments with individual quantum systems are continued by researchers, gaining better control over quantum-matter. Not restricted to the domain of atom spectroscopy, experiments are performed with a wide variety of physical systems, ranging from solid state devices featuring superconducting circuitry [BHW$^+$04] to color-centers in diamonds [WJ06, WON$^+$07]. The most prominent and extensively worked on goal of this research is a large-scale quantum computer, which should outperform its classical counterpart in several computational tasks by using quantum physics directly [Ben95]. Other applications, and possibly closer to completion, are quantum communication [GT07] and quantum enhanced metrology [GLM06, GLM11] in the domains of time measurement [SM99, MYH08], magnetic fields [OSRT13] and gravitation [KLM$^+$01, GMM$^+$08]. Recently even large companies like Google and

Microsoft started to invest in this field of research.

With this technology-focused research one might think that quantum physics is perfectly understood. But even after more than hundred years since Planck's and Einstein's breakthrough, quantum physics still poses conceptual difficulties to the research community. The transition from the microscopic world, governed by the laws of quantum physics to the macroscopic world described with classical physics is a difficult domain to understand. This is equally true for couplings between microscopic and macroscopic systems. In fact this might be the biggest challenge for the technologies under development, as the interaction of quantum devices with the (macroscopic, classical) environment perturbs their hard to maintain quantum properties. It is therefore essential to gain better understanding of these harmful processes and develop techniques to protect quantum systems against them.

1.1 Quantum Information

From a quantum information perspective every quantum state may be used to encode information. In this picture the decay of a quantum state is synonymous to the loss of the information it carries. Understanding decoherence in the context of quantum information is understanding what happens to the information: How it gets lost and if it is ultimately lost or just encoded in a different way or system. This understanding could possibly allow retrieval of the information, thereby battling information loss. An example of an active technique to preserve the information a quantum state carries is the *spin-echo*, developed by Hahn [Hah50] in the field of nuclear magnetic resonance, which today is often used in quantum information experiments. Another example is the Quantum Zeno effect, first observed by Itano *et al.* [IHBW90], defying intuition and resolving Zeno's paradox by hindering the evolution of a quantum system through constant measurement, thus preserving its initial state.
Contrary to this active approach another possibility is to construct quantum states robust against certain decay. This can be done by choosing convenient methods of encoding the information (which is also done in encoding classical information). A basic example is a *magnetic field independent qubit* with trapped ions [Lan05] or a *sweet spot* of a superconducting qubit [VAC+02, KYG+07]. More complex versions of encoding are for instance *decoherence-free subspaces* realised with trapped ions in [KMR+01, MKV+09], where the preservation of the information is bought at the expense of another resource: system size.
In most proposals quantum information is encoded in the quantum counterpart to the classical bit: a system which has two possible states, either 0 or 1. The quantum version, the *qubit*, is described by a quantum superposition of two states, $|0\rangle$ and $|1\rangle$. A general qubit would then be described by the

wavefunction

$$|\Psi\rangle = \alpha\,|0\rangle + \beta\,|1\rangle\,, \tag{1.1}$$

with α and β being complex numbers and $|\alpha|^2 + |\beta|^2 = 1$. In the classical case only the two states $\alpha = 1$, $\beta = 0$ and $\alpha = 0$, $\beta = 1$ exist. This is often also called a *spin*, as the mathematical description is identical, even if not necessarily a physical spin is used to encode the qubit. A possible choice might be two polarization states, horizontal and vertical, of a photon.
Different encodings of quantum information are possible though, even with continuous systems. These are typically more complex, but could possibly offer more flexible systems or encoding schemes. An example is the quantum-mechanical harmonic oscillator, where two qubit states would be encoded in complementary position and momentum states of the oscillator [GKP01].
The harmonic oscillator also offers something a spin system does not provide: a counterpart in the classical world. A spin is a system which may only take two states, unseen in classical physics and also only first described by P. A. M. Dirac in 1928 [Dir28]. The harmonic oscillator though exists in both the quantum and the classical world. A prominent classical example being the pendulum, intensively studied for clocks in the 18th and 19th century. With the harmonic oscillator the quantum-classical divide may be studied by exploring the differences of the two domains, or the transition from one to the other.
First experiments were performed by cooling a single ion to its motional ground state in a harmonic potential in 1995 [MMK$^+$95] and cooling an ensemble of $\sim 10^5$ neutral atoms to its motional ground state, forming a *Bose-Einstein condensate* also in 1995 [AEM$^+$95, DMA$^+$95]. Recent experiments were able to cool mechanical systems consisting of $\sim 10^{12}$ atoms to its motional ground state [TDL$^+$11].
Seminal experiments performed by the Wineland group studied the quantum harmonic oscillator with the motional states of trapped ions. They were able to prepare fundamental, non-classical states of motion like the coherent and squeezed state [MMK$^+$96]. Also a state of motion analogous to the infamous *Schrödinger's cat* [Sch35] was created, where an ion's wavepacket was split and the two parts separated at maximum by a distance more than ten times their size [MMKW96]. At the same time analysis methods for the motional states were developed to determine their energy eigenstate populations and to reconstruct their Wigner functions, giving a pictorial representation of the wavefunction [LMK$^+$96]. With the formidable control of the newly created states, the influence of several sources of decoherence was studied by coupling them to certain reservoirs [MKT$^+$00, TKK$^+$00, TMK$^+$00], forming a better understanding of the decay of quantum states.
All these experiments relied on ground state cooling of the ion's motion followed by a subsequent *coherent* manipulation of the ground state to form a desired state. After the preparation this state is bound to decay due to its

unavoidable coupling to the natural environment. The novel experiments described in this thesis also deal with the creation of harmonic oscillator states, although from a different angle. Here the desired states are prepared by engineering a coupling to an environment, which drives the ion's motion directly into those states.

1.2 Quantum Computing

First hints to quantum computing were given by R. P. Feynman [Fey82]. His thought was fueled from the difficulties of simulating quantum physics on computers. Due to the superposition nature of quantum states (such as the one given in equation 1.1) the simulation of a quantum system scales exponentially with the problem size, i.e. the time and memory it takes to simulate a composite quantum system of n particles grows exponentially with the number of single quantum systems, so x^n with x being a real number larger than one. With a device that is able to form the same superposition states as quantum systems the scaling would drop to a polynomial one: n^y instead of x^n (with y another real number larger than one). The principal solution is simple: Using a quantum system to simulate quantum physics.
D. Deutsch developed the idea of an universal quantum computer [Deu85], allowing the use of quantum physics also for other computational problems. Algorithms were developed for the quantum computer that beat their counterparts for classical computers in performance, with the important example of P. Shor's algorithm for prime factorization [Sho94].
With the inherent fragility of quantum states the need for an error correction was clear. In classical computers error correction can be easily performed by comparing copies of supposedly identical results. In quantum physics though the *non-cloning theorem* forbids the implementation of classical error correction based on copies [Die82, WZ82]. The discovery of quantum error correction [Sho95, Ste96] (an overview is given in [DMN13, LB13]) provided a solution to this problem, by circumventing the non-cloning theorem, giving quantum computing a realistic perspective and driving the development of experiments.

Ion traps have a leading role in quantum computing as they show highest fidelities for the logical operation, quantum gates, for single and two ions [HAB$^+$14]. A full scalable method set was shown [HHJ$^+$09], as well as the entanglement of 14 ions [MSB$^+$11]. These gates are performed with lasers and microwave fields interacting with the ions' electronic states and motion. A main task for trapped ion quantum computing today is realising larger scale systems. Two non-exclusive proposals exist relying on moving the ions in arrays of ion traps [WMI$^+$98, KCW02] and using photonic interconnects between ion traps [DBMM04] to build larger scale systems. Both proposals need multiple ion species to provide a decoupling of two ingredients. The proposal by Wineland *et al.* [WMI$^+$98, KCW02] uses a 'logic' ion to carry the quantum information

and an accompanying 'refrigerator' ion to keep the logic ion cooled close to its motional ground state despite heating from the transport through the trap array. The proposal by Duan *et al.* [DBMM04] needs one ion species to build up remote entanglement as a resource by a postselection process. The second species carries the information, which gets transferred on the entangled pair only after the entanglement is produced.
Less demanding possibilities for experiments than a universal quantum computer are *quantum simulators*. In these experiments a physical model system (e.g. a cloud of cold atoms) is used to mimic a system of interest (e.g. a solid state system). The model system is chosen for better control over the system's degrees of freedom and its better measurement possibilities than the system of interest. This allows to study the physics of the system of interest with the model system, advancing knowledge of the system of interest. A prominent experiment is the simulation of the Mott-insulator with cold atoms [GME$^+$02]. Recent examples with trapped ions are simulations of spin chains [RGL$^+$14, JLH$^+$14].

1.3 Dissipation as an Obstacle

Experiments in quantum physics evolve around the aim to create complex quantum states and controlling them. A major struggle is the decay of these states as they experience a coupling to the outside world. More precisely the coherence of a quantum state decays. This decoherence may be driven by different processes. An important source of decoherence is the dissipation of energy eigenstates, whereby typically a photon or phonon is emitted into the environment, carrying the quantum information of the previous state, and thus destroying it. Understanding dissipation is fundamental to reaching the goal of a large-scale quantum computer. But studying dissipation also means studying the quantum-classical divide, as by dissipation a quantum state turns into a classical state [Zur91].
Trapped ions are one of the quantum technologies that feature the best isolation from harmful environments. This is partly the reason why trapped ions exhibit very high fidelities for quantum operations.
The apparatus built as part of this thesis is aiming to investigate complex structures for quantum computing. The experiments described on the other hand are fundamental in nature and study the synthesis of a quantum state by a dissipative process.

1.4 Dissipation as a Resource

Dissipation is not in principle harmful. It may also be used to create a desirable effect. In fact any cooling process relies on artificially introduced dissipation, transferring the heat of a system into a cold bath, thereby reducing the

system's temperature and entropy. This is routinely done in laser cooling of atoms. In a normal cooling process though the final state is still a thermal state, not a superposition state with a well defined phase. Fundamental theoretical work was performed in the 1990s and 2000s to utilize dissipation for the preparation and protection of quantum states [CBPZ93, PCZ96, CMdMFD01, DMK+08, KBD+08] and for quantum computing itself [VWC09]. Recent experiments have started to implement these proposals and use dissipation as a tool to create and stabilize quantum states [KMJ+11, LGR+13, SHL+13]. Here dissipation is introduced deliberately to drive the quantum system into a desired state. This technique may be summarised by the term *dissipative state preparation*. The dissipation used is artificial. It is engineered to produce to the desired state. For this process to work the engineered dissipation must overcome the natural dissipative processes that harm the quantum state, in the same way as a cooling process needs to overcome heating from the environment.

1.5 This work

As part of this thesis a new complex experimental apparatus was constructed, with a main part being a micro-fabricated, segmented ion trap. The trap together with the full setup aim to provide a system with which it is possible to push the complexity boundary of quantum computing with trapped ions, while at the same time relying on existing and proven technologies. The principle architecture follows the proposal for a scalable quantum computer by D. Wineland *et al.* [WMI+98, KCW02], focussing on multiple species and the fast transport of ions through an array of ion traps. The fabrication techniques for the trap are based on those used by R. Blakestad [Bla10] with different realizations of several technical aspects. The apparatus was built to trap and manipulate two ion species, calcium and beryllium, allowing for sympathetic cooling of the *logic ion*, e.g. a beryllium ion, by cooling the *refrigerator ion*, e.g. a calcium ion [BDS+03]. The two species aspect also allows quantum simulation experiments to be implemented more easily than with only one species. The experimental apparatus is described in chapter 3. The apparatus was characterized by standard experiments described in chapter 4.

The main and novel experiments performed as part of this thesis are not directly related to the quantum computing aspect the trap was built for, but realize a technique of environment engineering to create and stabilize quantum states of a harmonic oscillator. These experiments profit from the low heating rate of the trap but are not using any of the special aspects of the trap discussed above. For these experiments dissipation is introduced by engineering a coupling of the ion's motion to its spin. The form of the coupling determines the properties of the created state. The technique was proposed in [CPBZ93, PCZ96]. It is similar to ground state cooling, used to prepare the

ground state of the harmonic oscillator, but is able to prepare superposition states. The states prepared are coherent, squeezed and displaced-squeezed states (see [Sch01] for an introduction). The coherent state is a displaced ground state and serves as a proof of principle, as it is easily prepared by other means. The main focus is on the squeezed state, which is a special quantum state, allowing to partially reduce (squeeze) the natural measurement uncertainty of quantum states. The displaced squeezed state is a combination of the two. From the preparation technique also a novel analysis method was developed, which allowed for the first time a phase and thus a fidelity measurement for squeezed motional states prepared with trapped ions. From estimations we see that the method should perform better than a traditional, non-dissipative approach, which is not the case with other experiments [KMJ$^+$11, LGR$^+$13, SHL$^+$13] using dissipative state preparation. This shows that dissipative state preparation may outperform tradition methods, and thus is well worth further research. The method is very general and can be used in other physical systems featuring a harmonic oscillator and a spin as long as the coupling between the two can be implemented. Systems like superconducting qubits and opto-mechanical systems are clear candidates. The experiments are described in chapter 5.

As stated above the experiments are using one ion and only one of its three motional modes. Thus the experiments performed here are only a first step to future experiments. Introducing an increased number of ions and motional modes will allow for a variety of states to be prepared and phenomena to be studied. Especially the second ion species will allow experiments to be implemented in an elegant way. Possible future experiments and technical improvements are discussed in chapter 7.
A theoretical introduction to the topics of the thesis is given in chapter 2.
The work for this thesis was carried out in close collaboration with H.-Y. Lo, whose thesis will be published at a later point in time. For details on certain topics the text references his future work.

Chapter 2

Theoretical Description

2.1 The Calcium Ion

The $^{40}Ca^{+}$ ion was used for most experiments in this thesis. It is a widely used choice in trapped ion experiments. It has no nuclear spin, which reduces the number of electronic levels as there is no hyperfine structure. The $^{40}Ca^{+}$ electronic level structure is shown in figure 2.1. It has two possible choices for a pseudospin/qubit transition. The first, not yet used in our system, is a Raman transition connecting the two $S_{1/2}$ states [Web05]. A second is a so-called optical qubit on the quadruple transition connecting the $S_{1/2}$ to the $D_{5/2}$ levels, which is the choice for the experiments described in this thesis. For Doppler cooling and fluorescence detection it features the dipole transition $S_{1/2}$ to $P_{1/2}$ which is driven with a laser at 397 nm and a repumper at 866 nm recycling population decaying from the $P_{1/2}$ to the $D_{3/2}$ state. A main feature of $^{40}Ca^{+}$ are the comparably easily obtainable wavelengths, which are used to manipulate the ions electronic state. Today all are accessible using commercially available diode lasers, including the wavelengths used to photo-ionize the neutral Ca atom. The absence of a hyperfine structure is a drawback for high fidelity experiments as no magnetic field independent transition exists [Lan05], which makes dealing with magnetic field noise an important technical goal. In the experiments described in this thesis the $^{40}Ca^{+}$ ion is used in an uncommonly high magnetic field of $\simeq 119$ G. This choice was made in order to utilize a field independent qubit transition in $^{9}Be^{+}$. As this regime is not well studied experimentally, simulation with full optical Bloch equations for the fluorescence detection/Doppler cooling system of the optical transitions between the levels $S_{1/2}$, $P_{1/2}$ and $D_{3/2}$ was performed by H.-Y. Lo. A full description will be given in the PhD-thesis of H.-Y. Lo.

(a) $^{40}Ca^{+}$ level scheme.

(b) $^{9}Be^{+}$ level scheme.

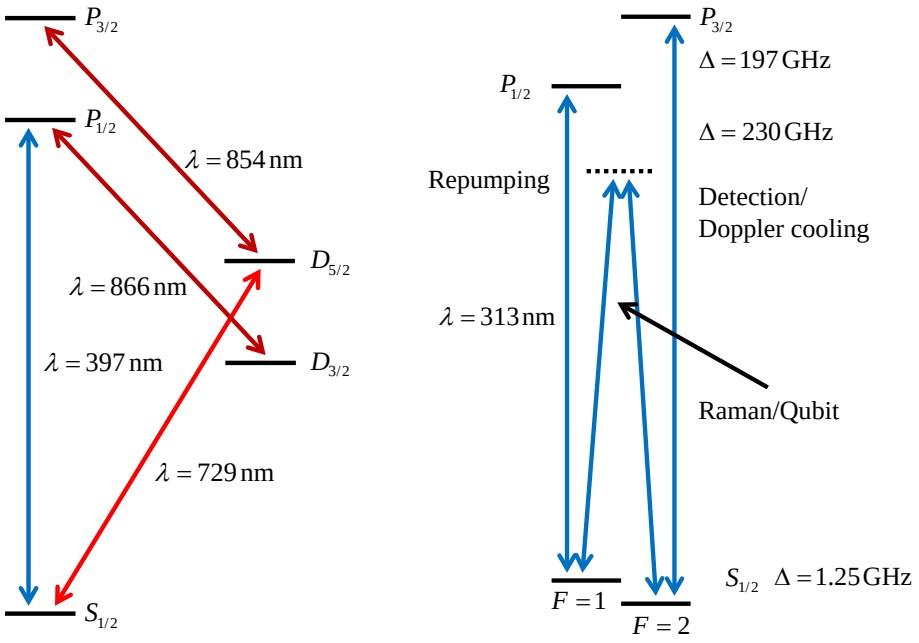

Figure 2.1: The level schemes with all relevant levels for the ion species $^{40}Ca^{+}$ and $^{9}Be^{+}$ used in the experiments in this thesis.

2.2 The Beryllium Ion

The $^{9}Be^{+}$ ion species was chosen for this experiment for its low mass, allowing for high trap frequencies. It has a nuclear spin of 3/2, giving it a hyperfine structure, and thus the possibility for a field-independent qubit transition. In this setup two clock states with the lowest magnetic field may be used: the $F = 2$, $m_F = 0$ to $F = 1$, $m_F = 1$ transition at 119.4 G or the the $F = 2$, $m_F = 1$ to $F = 1$, $m_F = 0$ transition at 119.6 G [Lan05]. In our experiments these levels are connected via a Raman transition detuned from the $P_{1/2}$ level by 230 GHz. An additional difference to $^{40}Ca^{+}$ is the absence of low-lying D levels. This results in a closed cycling transition for cooling and detection. It also means that the only laser wavelength needed for $^{9}Be^{+}$ is 313 nm[1]. The level scheme of $^{9}Be^{+}$ is shown in figure 2.1. In this thesis no experiments with $^{9}Be^{+}$ are presented. They will be covered in the PhD thesis of H.-Y. Lo. For the design of the experimental setup, especially the trap, the choice of $^{9}Be^{+}$ as

[1]Several frequency components are needed though, which are too far apart to be bridged by acousto-optical modulators. Our setup features 4 fibre laser to produce 3 destinct laser frequencies by frequency summation and second harmonic generation [LAK+14].

the high-fidelity qubit is of high importance and will be discussed in the coming chapters. In this context the principal concern regarding $^9Be^+$ relates to its mass, which is a factor 9/40 less than that of $^{40}Ca^+$.

2.3 Paul Trap

In an ion trap charged particles can be confined. Due to *Earnshaw's theorem* it is not possible to create confining potentials along all three spacial dimensions with only static electric fields. In a *linear Paul trap* a static potential is applied along the linear axis (also called the axial direction, here defined as the z axis). This creates a confining potential along the axial direction and an anti-confining potential in the radial plane perpendicular to the axial direction. To provide confinement in the radial direction an oscillating field is applied, which forms a *pseudopotential*. The trap built as part of this thesis is a linear Paul trap, and thus the following derivations are done with this geometry in mind. Several other geometries exist. An overview was given by W. Paul himself in [Pau90].
Constraining the potential to only quadratic terms the overall potential close to the center may be written as

$$\Phi(x,y,z) = \frac{1}{2}U_{\mathrm{dc}}\left(-\alpha_{\mathrm{dc}}x^2 - \beta_{\mathrm{dc}}y^2 + \gamma_{\mathrm{dc}}z^2\right) + \frac{1}{2}U_{\mathrm{rf}}\cos\left(\Omega_{\mathrm{rf}}t\right)\ \left(\alpha_{\mathrm{rf}}x^2 - \beta_{\mathrm{rf}}y^2\right) \tag{2.1}$$

where U_{dc} (U_{rf}) would be the static[2] (rf, radio frequency) voltage applied to the electrodes and α_{dc}, β_{dc}, γ_{dc}, α_{rf} and β_{rf} are factors depending on the geometry of the electrodes, here all taken to be positive. Here the coordinate system is already chosen such that x and y align with the principal axes of the pseudopotential (see below). In the general case a rotation angle would have to be included ($x' = \cos(\alpha)\,x - \sin(\alpha)\,y$ and $y' = \sin(\alpha)\,x + \cos(\alpha)\,y$), leading to cross-terms $\sim xy$ after squaring. The principal axes are solely defined by the static potential (α_{dc} and β_{dc}). Due to Laplace's equation α_{rf} and β_{rf} must be equal and thus the resulting pseudo-potential is rotationally symmetric.
As all three axes of the potential are independent, the equations of motion may be derived separately for each axis. In one dimension for a single ion of mass m and charge $+1e$ the equation of motion for the ions position u is obtained from

$$\ddot{u} = \frac{F(t)}{m} = -\frac{e}{m}\frac{\mathrm{d}\Phi}{\mathrm{d}u}. \tag{2.2}$$

[2] 'dc' officially means *direct current*. In the ion trapping community though it is common to use it synonymously for static fields and the electrodes that are used to form the static fields ('dc electrodes'). This is inherited from the fact, that these electrodes are typically fed with dc signals in contrast to the rf electrodes were rf signals are applied. This sometimes inaccurate convention is used throughout the text to adhere to the convention.

For the axial direction of the trap this is just the harmonic oscillator with an oscillation frequency of

$$\omega_z = \sqrt{\frac{e\,\gamma_{\mathrm{dc}} U_{\mathrm{dc}}}{m}}. \tag{2.3}$$

The equation of motion for the radial axes is given by

$$\ddot{u}_{\pm} = \pm\frac{e}{m}\left\{\delta_{\mathrm{dc}}\,U_{\mathrm{dc}} + \delta_{\mathrm{rf}}\,U_{\mathrm{rf}}\cos\left(\Omega_{\mathrm{rf}}\,t\right)\right\}\,u_{\pm} \tag{2.4}$$

with $u_+ \equiv x$ and $u_- \equiv y$ and $\delta_{\mathrm{dc/rf}} \equiv \alpha_{\mathrm{dc/rf}}$, $\beta_{\mathrm{dc/rf}}$ respectively. This differential equation is of the form of Mathieu's differential equation [LBMW03] with Mathieu parameters

$$a_u = -\frac{4\,e\,\delta_{\mathrm{dc}}\,U_{\mathrm{dc}}}{m\,\Omega_{\mathrm{rf}}^2} \quad \text{and} \quad q_u = -\frac{2\,e\,\delta_{\mathrm{rf}}\,U_{\mathrm{rf}}}{m\,\Omega_{\mathrm{rf}}^2} \tag{2.5}$$

and may be solved as such with an exponential series [LBMW03]. Linear Paul traps are commonly operated in a regime where $|a_u|, q_u^2 \ll 1$ are fulfilled. For other values of the Mathieu parameters the solutions to the equation have unstable areas. With this the solution to equation 2.4 may be given as a first order approximation of the full solution as

$$u_{\pm}(t) \simeq A\cos\left(\omega_{\mathrm{rf},\pm}t\right)\left(1 - \frac{q_u}{2}\cos\left(\Omega_{\mathrm{rf}}t\right)\right) \tag{2.6}$$

with A fixed by initial conditions and $\omega_{\mathrm{rf},\pm}$ a low frequency of the so-called *secular* motion given by

$$\omega_{\mathrm{rf},\pm} = \sqrt{a_u + \frac{q_u^2}{2}}\,\frac{\Omega_{\mathrm{rf}}}{2}. \tag{2.7}$$

Further simplifying this result by neglecting the influence of the static potential ($a_u \to 0$) the following is obtained:

$$\omega_{\mathrm{rf}} = \frac{\sqrt{2}\,e\,\delta_{\mathrm{rf}}\,U_{\mathrm{rf}}}{m\,\Omega_{\mathrm{rf}}}. \tag{2.8}$$

2.3.1 Pseudopotential Approximation

The pseudopotential approximation for rf ion traps as derived in [Deh68] is useful for building an intuition for the rf confinement and as a tool in the simulation of ion traps (as done in section 3.2.1).
The equation of motion of a particle with charge e and mass m in an oscillating electric field is given by

$$m\ddot{z} = F(t) = eE_0\cos(\Omega_{\mathrm{rf}}\,t) \tag{2.9}$$

with a solution

$$z(t) = \bar{z} + \zeta(t) \tag{2.10}$$

with $\bar{z} = \text{const}$ the time averaged rest position and

$$\zeta(t) = -\zeta_0 \cos(\Omega_{\text{rf}} t), \text{ with } \zeta_0 = \frac{eE_0(\bar{z})}{m\Omega_{\text{rf}}^2}, \tag{2.11}$$

the oscillating *mircomotion*. Time-averaging the force over an oscillation period $1/\Omega_{\text{rf}}$ gives zero:

$$\langle F(t) \rangle_{\text{av}} = \langle eE_0 \cos(\Omega_{\text{rf}} t) \rangle_{\text{av}} = 0, \tag{2.12}$$

meaning that the charged particle oscillated around the fixed average position $\bar{z}$. Assuming now a non-vanishing gradient for the electric field, i.e. $\partial E_0/\partial z \neq 0$ and developing the field around the average rest-position $\bar{z}$ as

$$E_0(z) \simeq E_0(\bar{z}) + \left.\frac{\partial E_0(z)}{\partial z}\right|_{z=\bar{z}} (z - \bar{z}) \tag{2.13}$$

This may be re-written with the solution given by equation 2.10 to

$$E_0(z) \simeq E_0(\bar{z}) + \frac{\partial E_0(\bar{z})}{\partial \bar{z}} \zeta(t). \tag{2.14}$$

Using this expression to estimate the averaged force we get

$$\langle F(t) \rangle_{\text{av}} = e \left\langle E_0(\bar{z}) \cos(\Omega_{\text{rf}} t) + \frac{\partial E_0(\bar{z})}{\partial \bar{z}} \zeta(t) \cos(\Omega_{\text{rf}} t) \right\rangle_{\text{av}}. \tag{2.15}$$

The first term again averages to zero, while the second gives

$$\langle F(t) \rangle_{\text{av}} = e \frac{\partial E_0(\bar{z})}{\partial \bar{z}} \langle \zeta(t) \cos(\Omega_{\text{rf}} t) \rangle_{\text{av}} = e \frac{\partial E_0(\bar{z})}{\partial \bar{z}} \left(-\frac{\zeta_0}{2} \right), \tag{2.16}$$

resulting in the non-zero net-force $\bar{F}(\bar{z})$ as

$$\bar{F}(\bar{z}) = -e \frac{\partial E_0(\bar{z})}{\partial \bar{z}} \frac{eE_0(\bar{z})}{m\Omega_{\text{rf}}^2}, \tag{2.17}$$

using equation 2.10 to replace ζ_0. This expression allows to introduce a *pseudopotential* $\Psi(\bar{z})$ with

$$\bar{F}(\bar{z}) = -e \frac{\partial \Psi(\bar{z})}{\partial \bar{z}} \text{ with } \Psi(\bar{z}) \equiv \frac{eE_0^2(\bar{z})}{4m\Omega_{\text{rf}}^2}. \tag{2.18}$$

Notably the confinement of the ion is proportional to the square of the averaged field, and inversely proportional to the ions mass m and the square of the drive frequency Ω_{rf}. The secular frequency is then given by

$$\omega_{\mathrm{rf}} = \frac{e\, E_0(\bar{u})}{\sqrt{2}\, m\, \Omega_{\mathrm{rf}}}, \tag{2.19}$$

which is equivalent to the result from approximating the solution to Mathieu's equation with $E_0(\bar{u}) = 2\delta_{\mathrm{rf}} U_{\mathrm{rf}}$ (see equation 2.8).
Looking now at the averaged kinetic energy of the micromotion using equation 2.11

$$\langle W_{\mathrm{mm}}(z)\rangle_{\mathrm{av}} = \langle \frac{1}{2} m \dot{\zeta}^2 \rangle_{\mathrm{av}} = \frac{1}{2} m\, \Omega_{\mathrm{rf}}^2\, \zeta_0^2\, \frac{\Omega_{\mathrm{rf}}}{2\pi} \int_{-\pi/\Omega_{\mathrm{rf}}}^{\pi/\Omega_{\mathrm{rf}}} \sin\left(\Omega_{\mathrm{rf}} t\right) \mathrm{d}t, \tag{2.20}$$

We arrive at the result [Deh68]

$$\langle W_{\mathrm{mm}}(z)\rangle_{\mathrm{av}} = \frac{e^2 E_0(\bar{z})^2}{4 m \Omega_{\mathrm{rf}}^2} = e\Psi(\bar{z}), \tag{2.21}$$

showing that the averaged kinetic energy of the micromotion is the pseudopotential energy. With this concept it is now easy to see that a static field in addition to the pseudopotential leads to additional micromotion. This will be discussed in the next section.

2.3.2 Micromotion

In this section two kinds of micromotion are investigated, *excess* and *intrinsic* micromotion. We are focussing on the behavior of the two ion species, which have different mass.
An ion in a harmonic potential under the influence of a stray electric field will have a new equilibrium position u_0, which can be found by equating the force F_{st} exerted by the electric field and the restoring force of the harmonic potential well F_{pot} as

$$F_{\mathrm{st}} = e\, E_{\mathrm{st}} = m\, \omega^2 u_0 = F_{\mathrm{pot}} \tag{2.22}$$

with the ion's charge being $+1e$, the stray electric field E_{st}, the ion's mass m and its motional frequency ω in the harmonic potential. This results in the equilibrium position u_0 to be

$$u_0 = \frac{e\, E_{\mathrm{st}}}{m\, \omega^2} \tag{2.23}$$

If now the potential is the pseudopotential, the motional frequency can be rewritten with equation 2.8

$$u_0 = \frac{m\, E_{\mathrm{st}}\, \Omega_{\mathrm{rf}}}{2\, e\, \delta_{\mathrm{rf}}^2\, U_{\mathrm{rf}}^2}. \tag{2.24}$$

This assumes that

$$a_i \ll q_i^2, \tag{2.25}$$

i.e. the static part of the trapping fields in the radial plane is negligible. In this case the ion's equilibrium position is proportional to the ion's mass

$$u_0 \sim m. \tag{2.26}$$

As done in [BMB+98], using this result equation 2.6 may be modified to

$$u(t) \simeq A\left(u_0 + \cos\left(\omega_{\mathrm{rf}} t\right)\right)\left(1 - \frac{q_u}{2}\cos\left(\Omega_{\mathrm{rf}} t\right)\right). \tag{2.27}$$

The electric field leads to an additional contribution to the oscillating motion of the ion at the trap drive frequency Ω_{rf}. This so-called *excess* micromotion can be of significant magnitude and lead to adverse effects for trapped ions [BMB+98, Hom13]. For the experiments in this thesis the only effect that matters is from an effective modulation of the laser beam, creating sidebands in the spectrum of the laser as seen by the ion at the rf drive frequency Ω_{rf}. The laser field in the rest frame of the ion is then given by

$$\mathbf{E}(t) \simeq \mathrm{Re}\left\{\mathbf{E}_0 \exp\left(i\,\mathbf{k}\cdot\mathbf{u} - i\,\omega_{\mathrm{laser}}\,t\right)\right\} \tag{2.28}$$

with ω_{laser} the frequency of the laser, $\mathbf{E}_0$ the amplitude of the electric field of the laser beam, $\mathbf{k}$ the wave vector of the laser beam and $\mathbf{u}$ the position of the ion, now in three dimensions. As discussed in [BMB+98] the resulting line shape is

$$L \propto \sum_{n=-\infty}^{\infty} \frac{J_n^2(\beta)}{(\omega_{\mathrm{ion}} - \omega_{\mathrm{laser}} + n\Omega_{\mathrm{rf}})^2 + (\gamma/2)^2)} \tag{2.29}$$

with ω_{ion} the frequency of the ion's transition, J_n are Bessel functions of the first kind and β the modulation of the ion's motion as given by

$$\beta = \left|\frac{1}{2}\sum_{i=x,y} k_i u_{0,i} q_i\right| \tag{2.30}$$

with the single components of $\mathbf{k}$, $\mathbf{u}_0$ and the corresponding q-values (eq. 2.5). With the q-values' mass dependence of $q \sim 1/m$ and equation 2.26, the modulation is mass-independent

$$\beta_{\mathrm{ex}} \sim 1. \tag{2.31}$$

In case that the condition stated in equation 2.25 is not fulfilled, a mass dependence may arise. Also there is still a difference in the modulation for different

species, as the modulation depends also on the k-vector, where different fluorescence wavelength of the species enter.

A second type micromotion exists, attributed *intrinsic*, which may arise from a phase shift of the rf drive between rf-electrodes (which is unlikely for our trap geometry) or a residual rf field along the axial direction (which can arise from badly aligned electrodes) [BMB+98, ABLW11]. This micromotion can not be compensated easily.
Investigating here only the influence of a homogenous rf field along the axial direction, we start by writing down the superposition of the trapping field and a rf field:

$$E_{\text{total}} = -\gamma_{\text{dc}} U_{\text{dc}} z + E_{\text{rf}} \cos(\Omega_{\text{rf}} t). \tag{2.32}$$

This is using the definitions of equation 2.1 with $\alpha_{\text{dc}} = \beta_{\text{dc}} = 0$. The equation of motion is then given by

$$m\ddot{z} = F_z(t) = -e\gamma_{\text{dc}} U_{\text{dc}} z + eE_{\text{rf}} \cos(\Omega_{\text{rf}} t) \tag{2.33}$$

for an ion of mass m and charge $+1e$. This is a harmonic oscillator driven by a sinusoidal driving force with the general solution

$$z(t) = A\cos(\omega_z t + \varphi) + \frac{eE_{\text{rf}}}{m(\omega_z^2 - \Omega_{\text{rf}}^2)} \cos(\Omega_{\text{rf}} t) \tag{2.34}$$

with the replacement $\omega_z = \sqrt{e\,\gamma_{\text{dc}} U_{\text{dc}}/m}$ (which was already given in equation 2.3), and the parameters A and φ defined by initial conditions. The first term describes the secular motion. The second term describes the influence of the driving field. As $\Omega_{\text{rf}} \gg \omega_z$ the driven motion $z_{\text{drv}}(t)$ may be written as

$$z_{\text{drv}}(t) = -\frac{eE_{\text{rf}}}{m\Omega_{\text{rf}}^2} \cos(\Omega_{\text{rf}} t) \tag{2.35}$$

This means that the modulation index from intrinsic micromotion β_{in} has a mass dependence as

$$\beta_{\text{in}} \sim \frac{1}{m}. \tag{2.36}$$

Again the same dependence for the k-vector of the laser beams applies. Although this is an unwanted effect, recent experiments from the NIST ion storage group show that even in presence of strong modulation effects high fidelity quantum control can be successfully performed [Lei14].

2.4 Trapped Ion Quantum Physics

For the quantum physics investigated in this thesis a single trapped ion may be described as a simple spin-plus-motion system, where only one mode of the ion's motion is considered for the motional part and a two-level system represents the electronic degree of freedom. The motion is well described by a *harmonic oscillator* with its energy-eigenstates $\{|n\rangle\}, n \in \mathbb{N}$, with a lowest energy-eigenstate, the *ground state* $|0\rangle$. These states form the Hilbert space $\mathcal{H}_{\text{motion}}$. The two-level system is represented by a pseudo-spin with the two states spin-down $|\downarrow\rangle$ and spin-up $|\uparrow\rangle$, forming the Hilbert space $\mathcal{H}_{\text{spin}}$. This spin-plus-motion system has a convenient pictorial representation as a *state ladder*, given in figure 2.2. It forms the combined Hilbert space

$$\mathcal{H}_{\text{ion}} = \mathcal{H}_{\text{spin}} \otimes \mathcal{H}_{\text{motion}} \tag{2.37}$$

with states

$$|\downarrow, n\rangle \equiv |\downarrow\rangle \otimes |n\rangle \text{ and} \tag{2.38}$$
$$|\uparrow, n\rangle \equiv |\uparrow\rangle \otimes |n\rangle\,, \text{ with } n \in \mathbb{N}. \tag{2.39}$$

We are then given a toolbox of operations we may use to manipulate this system, all implemented with laser light. This toolbox consists of coherent and dissipative manipulations, depicted in the state ladder in figure 2.2. The coherent manipulations used here are in essence: A carrier operation rotating only the spin, leaving the motional state untouched:

$$|\downarrow, n\rangle \leftrightarrow |\uparrow, n\rangle\,. \tag{2.40}$$

A red sideband operation, which flips the spin from down to up and reducing the number of motional quanta by one or flips the spin from up to down by increasing the number of motional quanta by one. Written in short:

$$|\downarrow, n\rangle \leftrightarrow |\uparrow, n-1\rangle\,. \tag{2.41}$$

Finally a blue sideband operation, doing the inverse of the red sideband:

$$|\downarrow, n\rangle \leftrightarrow |\uparrow, n+1\rangle\,. \tag{2.42}$$

Similar transitions exist for the other motional modes and also higher order sidebands exist. All of them are well resolved and far off-resonant from the transitions discussed here, thus they may be neglected in the further discussion. An important feature of coherent operations is that they are reversible: Every operation may be undone by a suitable 'anti-operation', simply by changing the phase of the laser by π and repeating the operation. No information about the system gets lost. Everything may be described by unitary dynamics. The dissipative manipulation contrasts this behaviour. It may dissipate the spin

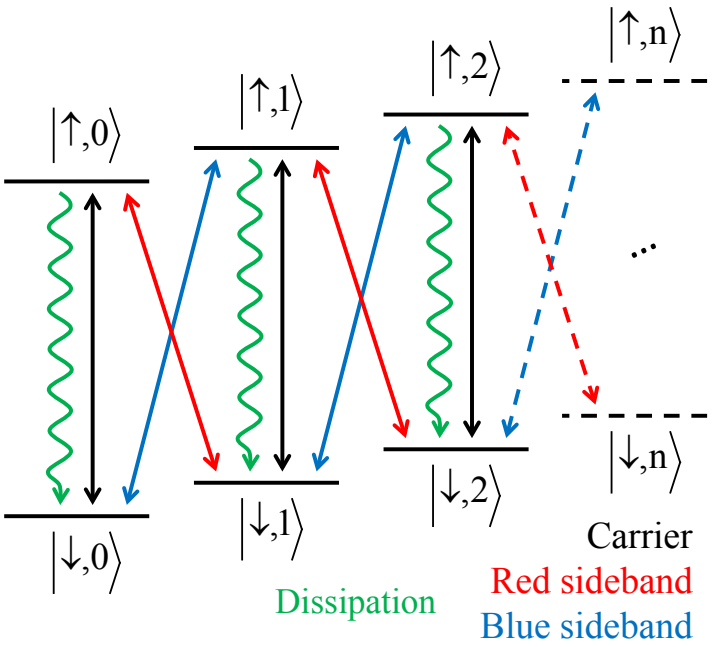

Figure 2.2: State ladder for the spin-plus-motion system. The state ladder shows levels for the spin-plus-motion states. Changing the spin goes from up to down or vice versa, changing the motion goes from left to right or vice versa. The toolbox for manipulating these states is drawn with arrows, the coherent manipulation are the straight arrows, black for the carrier, red for the red sideband, blue for the blue sideband. The dissipation is drawn as wiggly green line. The dissipation is only one-way, from spin-up to spin-down, in contrast to the coherent manipulation, which is always reversible.

from up to down only, essentially resetting it, again without changing the motional state[3]:

$$|\uparrow, n\rangle \rightarrow |\downarrow, n\rangle \,. \tag{2.43}$$

This process is *irreversible*, the ion emits a photon in this process and the information about the previous state is lost. This tool may be used to extract entropy from the system, something not possible with the coherent manipulations. The coherent manipulations are derived and discussed in section 2.4.1. The dissipation and its uses is treated in section 2.5.

[3]This only holds for strong confinement, leading to the Lamb-Dicke approximation. See section 2.4.1

2.4.1 Coherent Interaction

To describe the ion quantum mechanically only the axial direction of motion z and only two electronic states are considered here. All experiments described in this thesis are performed with the axial mode of motion. Effects from the radial modes of motion may be neglected most of the time as these are far off-resonant. The same holds for the two electronic states. This derivation follows [WMI+98], making simplifications where applicable in the context of this thesis.
The ion's motion is very well described by the Hamiltonian for the quantum mechanical harmonic oscillator

$$\hat{H}_{\mathrm{m}} = \hbar\,\omega_{\mathrm{m}}\,\hat{a}^{\dagger}\,\hat{a} \tag{2.44}$$

with the motional frequency ω_{m} and the ion's mass m, the destruction and creation operators $\hat{a}$ and $\hat{a}^{\dagger}$ and the energy-eigenstates $\{|n\rangle\}$. The position operator for the ion is given by

$$\hat{z} = z_0(\hat{a} + \hat{a}^{\dagger}) \text{ with } z_0 = \sqrt{\frac{\hbar}{2m\omega_{\mathrm{m}}}}, \tag{2.45}$$

where z_0 is the root-mean-square (rms) spread of the ground state wavefunction. For a $^{40}Ca^{+}$ ion with a motional frequency $\omega_{\mathrm{m}} = 2\pi \times 2\,\mathrm{MHz}$ the wavefunction extend is $z_0 \simeq 8\,\mathrm{nm}$.
The internal states with the energy splitting $E = \hbar\omega_0$ will be described as a pseudo-spin with states $|\uparrow\rangle$ and $\langle\downarrow|$ and the spin-flip operators $\hat{\sigma}_+ = |\uparrow\rangle\langle\downarrow|$ and $\hat{\sigma}_- = |\downarrow\rangle\langle\uparrow|$ and the Hamiltonian is given by

$$\hat{H}_{\mathrm{internal}} = \hbar\,\omega_0\,\hat{\sigma}_z \text{ with } \hat{\sigma}_z = |\downarrow\rangle\langle\downarrow| - |\uparrow\rangle\langle\uparrow| \tag{2.46}$$

In general the motional splitting is much smaller than the splitting of the internal states $\omega_0 \gg \omega_{\mathrm{m}}$. The ion's interaction with a laser field may be formulated in the interaction Hamiltonian

$$\hat{H}_{\mathrm{I}} = \hbar\,\Omega\,(\hat{\sigma}_+ + \hat{\sigma}_-)\left(e^{i(kz-\omega t+\Phi)} + e^{-i(kz-\omega t+\Phi)}\right) \tag{2.47}$$

where ω is the frequency of the laser, Φ its phase, k is the projection of its k-vector onto the motional axis of ion under consideration and Ω the Rabi frequency. Moving to the interaction picture by

$$\hat{H}'_{\mathrm{I}} = U_0^{\dagger}(t)\,\hat{H}_{\mathrm{I}}\,U_0(t) \tag{2.48}$$

with $U_0(t) = e^{-i(H_0/\hbar)t}$ and $\hat{H}_0 = \hat{H}_{\mathrm{m}} + \hat{H}_{\mathrm{internal}}$ and making the rotating-wave approximation by neglecting terms with $\exp(\pm i(\omega + \omega_{\mathrm{m}}))$ one finds

$$\hat{H}'_{\mathrm{I}}(t) = \hbar\,\Omega\,\hat{\sigma}_+ \exp\left[i\eta\left(\hat{a}\,e^{-i\omega_{\mathrm{m}}t} + \hat{a}^{\dagger}\,e^{i\omega_{\mathrm{m}}t}\right)\right] e^{i(\Phi-\delta t)} + \mathrm{h.c.} \tag{2.49}$$

with $\eta \equiv kz_0$ the *Lamb-Dicke parameter* and $\delta = \omega - \omega_0$ the detuning of the laser's frequency from the internal transition. This Hamiltonian has resonances for $\delta = (n' - n)\,\omega_z$. Assuming only a small detuning $\Delta \ll \omega_z$ from one of these, Rabi frequencies for transitions changing the motional quantum number from n to n' and flipping the spin can be calculated as

$$\Omega_{n',n} \equiv \Omega \left| \langle n' | \, e^{i\eta(\hat{a}+\hat{a}^\dagger)} \, |n\rangle \right| \tag{2.50}$$

$$= \Omega \, e^{-\eta^2/2} \sqrt{\frac{n_<!}{n_>!}} \eta^{|n'-n|} \, L_{n_<}^{|n'-n|}(\eta^2), \tag{2.51}$$

with $n_<(n_>)$ the lesser (greater) of n and n' and L_n^α the generalized Laguerre polynomial. These Rabi frequencies may be in principle calculated analytically, but may be simplified by making the *Lamb-Dicke approximation*. If the ion's motional amplitude is small compared to the wavelength of the optical transition it follows that $\eta \ll 1$ (for $^{40}\mathrm{Ca}^+$ $\eta \simeq 0.05$) and the exponential term in equation 2.51 may be expanded in orders of η. Taking only the lowest order results in

$$\Omega_{n',n} = \Omega \, \eta^{|n'-n|} \sqrt{\frac{n_<!}{n_>!}} \frac{1}{|n'-n|!} \tag{2.52}$$

As all experiments of this thesis are well described using this approximation it will be used from here on if not noted otherwise. All coherent manipulations in this thesis make use of only the three strongest transitions. The first being the carrier, rotating the spin but leaving the motional state the same ($\delta = \Delta$, $n' = n$) with the Hamiltonian

$$\hat{H}_{\mathrm{car}} = \hbar \, \Omega \left(\hat{\sigma}_- \, e^{-i(\Delta t + \Phi)} + \hat{\sigma}_+ \, e^{i(\Delta t + \Phi)} \right). \tag{2.53}$$

The second is the first red sideband transition ($\delta = -\omega_{\mathrm{m}} + \Delta$, $n' = n - 1$) with

$$\hat{H}_{\mathrm{rsb}} = \hbar \, \eta \, \Omega \left(-i \, \hat{a}^\dagger \, \hat{\sigma}_- \, e^{-i(\Delta t + \Phi)} + i \, \hat{a} \, \hat{\sigma}_+ \, e^{i(\Delta t + \Phi)} \right), \tag{2.54}$$

and the third the first blue sideband transition ($\delta = \omega_{\mathrm{m}} + \Delta$, $n' = n + 1$) with

$$\hat{H}_{\mathrm{bsb}} = \hbar \, \eta \, \Omega \left(-i \, \hat{a} \, \hat{\sigma}_- \, e^{-i(\Delta t + \Phi)} + i \, \hat{a}^\dagger \, \hat{\sigma}_+ \, e^{i(\Delta t + \Phi)} \right). \tag{2.55}$$

With zero detuning ($\Delta = 0$) these Hamiltonians lead to Rabi oscillations between the states $|\downarrow, n\rangle \leftrightarrow |\uparrow, n'\rangle$ with $n' = n$ for the carrier, $n' = n - 1$ for the red sideband and $n' = n + 1$ for the blue sideband. The Rabi frequencies for these oscillations are given by

$$\Omega_{n,n'} = \Omega_{n',n} = \Omega e^{-\eta^2/2} \eta^{|n'-n|} \sqrt{\frac{n_>!}{n_<!}} L_{n<}^{|n'-n|}(\eta^2) \tag{2.56}$$

with $n_>$ ($n_<$) the greater (lesser) of n' and n, and $L_n^\alpha(X)$ the generalized Laguerre polynomial. In the Lamb-Dicke limit this may be simplified to

$$\Omega_{n,n'} = \Omega_{n',n} = \Omega\eta^{|n'-n|}\frac{\sqrt{n_>!/n_<!}}{|n'-n|!}, \tag{2.57}$$

resulting in the Rabi frequency for the carrier $\Omega_{\text{car}} = \Omega$ and the motional state dependent Rabi frequencies for the first sidebands $\Omega_{\text{rsb}} = \eta\sqrt{n}\Omega$ and $\Omega_{\text{bsb}} = \eta\sqrt{n+1}\Omega$, which are suppressed with respect to the carrier by η. Higher order sidebands are suppressed by η^j with j the order of the respective sideband, and thus difficult to address.
Driving one of the transitions (carrier, red or blue sideband) for a time $t = 2\pi/\Omega_{\text{trans}}$ with Ω_{trans} the Rabi frequency of the respective transition, results in a full rotation of the spin, returning it to its initial state. This would commonly be described as a '2π pulse' on the respective transition. Equally we will use definitions of a 'π pulse' and a '$\pi/2$ pulse' for pulse lengths that either invert ('flip') the spin state ($t = \pi/\Omega_{\text{trans}}$) or rotate it by $\pi/2$ ($t = \pi/(2\Omega_{\text{trans}})$), commonly used to create equal superpositions of $|\downarrow\rangle$ and $|\uparrow\rangle$.

The red sideband Hamiltonian is fully analogous to the *Jaynes-Cummings Hamiltonian*, which describes the dynamics of a two-level system coupled to a single radiation mode [HR06]. In trapped ion physics the radiation mode is replaced by the motional mode of the ion and the coupling strength can be tuned changing the laser power. This is also true for the counterpart, the blue sideband Hamiltonian which is analogous to the *anti-Jaynes-Cummings Hamiltonian*. In this thesis these names will be used interchangeably, also emphasising that the presented experiments have wide applicability across different physical implementations in which Hamiltonians of the Jaynes-Cummings type occur.

2.4.2 Dissipation, Master Equation

To introduce dissipation, its effect combined with the coherent manipulations must be described. We start out by formulating the general spin-motion Hamiltonian

$$\hat{H} = \hbar\Omega\left(\hat{K}\,\hat{\sigma}_+ + \hat{K}^\dagger\,\hat{\sigma}_-\right), \tag{2.58}$$

with the new, general motional operator $\hat{K}$. By specifying this operator we may formulate any of the coherent operations introduced in section 2.4.1, even combinations of them. For the following derivation $\hat{K}$ is assumed to be a general operator acting only on $\mathcal{H}_{\text{motion}}$.
The dissipation is a decay of the upper spin state $|\uparrow\rangle$ into the spin-down state $|\downarrow\rangle$ with a rate Γ. It is described by the *Lindblad operator*

$$\hat{L} = \sqrt{\Gamma}\hat{\sigma}_-\,. \tag{2.59}$$

With the density matrix formalism an arbitrary, mixed state in the ions Hilbert space $\mathcal{H}_{\text{ion}} = \mathcal{H}_{\text{spin}} \otimes \mathcal{H}_{\text{motion}}$ is written as

$$\hat{\rho}_{\,\text{ion}} = \hat{\rho}_{\,\text{spin}} \otimes \hat{\rho}_{\,\text{motion}}. \tag{2.60}$$

The time evolution of the ion's state $\hat{\rho} \equiv \hat{\rho}_{\,\text{ion}}$ under the action of the spin-motion Hamiltonian and the dissipation is described by a Master equation in Lindblad form as

$$\frac{\mathrm{d}\hat{\rho}}{\mathrm{d}t} = \frac{i}{\hbar}\left[\hat{H}\,,\hat{\rho}\right] + \hat{L}\,\hat{\rho}\,\hat{L}^{\dagger} - \frac{1}{2}\left\{\hat{L}^{\dagger}\,\hat{L}\,,\hat{\rho}^{\dagger}\right\}_{+}. \tag{2.61}$$

The first term on the right-hand side describes the unitary evolution of the system and is, together with the left-hand side, similar to the *von Neumann equation*. It should be noted though that the Hamiltonian $\hat{H}$ needs in principle to be renormalised for its coupling to the environment, which leads to energy-level shifts. The other terms on the right-hand are sometimes summarised as *Dissipator* $\mathcal{D}(\hat{\rho}\,)$ or *Lindblad superoperator* describing the non-unitary evolution of the system, with the decay of coherences $|{\uparrow}\rangle\langle{\downarrow}|$ and $|{\downarrow}\rangle\langle{\uparrow}|$ at a rate $\Gamma/2$, and *quantum jumps* from the upper to the lower spin state $|{\uparrow}\rangle\langle{\uparrow}| \rightarrow |{\downarrow}\rangle\langle{\downarrow}|$ at a rate Γ. See [HR06, BP02] for a derivation and discussion of the Lindblad equation.

Adiabatic Elimination

Equation 2.61 may be simplified to describe the experimental situation more efficiently by restricting the discussion to the regime where the dissipation is much stronger than the coherent driving: $\Omega \ll \Gamma$. Introducing the partial matrix elements $\hat{\rho}_{ij} = \langle i|\,\hat{\rho}_{\text{ion}}\,|j\rangle$ with $\{i,j\} \in \{\uparrow,\downarrow\}$ the full density matrix is re-written as

$$\hat{\rho}_{\text{ion}} = \hat{\rho}_{\downarrow\downarrow}\,|{\downarrow}\rangle\langle{\downarrow}| + \hat{\rho}_{\downarrow\uparrow}\,|{\downarrow}\rangle\langle{\uparrow}| + \hat{\rho}_{\uparrow\downarrow}\,|{\uparrow}\rangle\langle{\downarrow}| + \hat{\rho}_{\uparrow\uparrow}\,|{\uparrow}\rangle\langle{\uparrow}|\,, \tag{2.62}$$

where here and from now on the tensor product symbol $\otimes$ is omitted for simplicity. Inserted into the Master equation 2.61 a system of four coupled differential equations can be found

$$\frac{\mathrm{d}\hat{\rho}_{\downarrow\downarrow}}{\mathrm{d}t} = -i\Omega\left(\hat{K}^{\dagger}\,\hat{\rho}_{\uparrow\downarrow} - \hat{\rho}_{\downarrow\uparrow}\,\hat{K}\right) + \Gamma\hat{\rho}_{\uparrow\uparrow} \tag{2.63}$$

$$\frac{\mathrm{d}\hat{\rho}_{\uparrow\uparrow}}{\mathrm{d}t} = -i\Omega\left(\hat{K}\,\hat{\rho}_{\downarrow\uparrow} - \hat{\rho}_{\uparrow\downarrow}\,\hat{K}^{\dagger}\right) - \Gamma\hat{\rho}_{\uparrow\uparrow} \tag{2.64}$$

$$\frac{\mathrm{d}\hat{\rho}_{\uparrow\downarrow}}{\mathrm{d}t} = -i\Omega\left(\hat{K}\,\hat{\rho}_{\downarrow\downarrow} - \hat{\rho}_{\uparrow\uparrow}\,\hat{K}\right) - \frac{\Gamma}{2}\hat{\rho}_{\uparrow\downarrow} \tag{2.65}$$

$$\frac{\mathrm{d}\hat{\rho}_{\downarrow\uparrow}}{\mathrm{d}t} = -i\Omega\left(\hat{K}^{\dagger}\,\hat{\rho}_{\uparrow\uparrow} - \hat{\rho}_{\downarrow\downarrow}\,\hat{K}^{\dagger}\right) - \frac{\Gamma}{2}\hat{\rho}_{\downarrow\uparrow} \tag{2.66}$$

To derive a differential equation for only $\hat{\rho}_{\downarrow\downarrow}$ from eq. 2.63, the boundary condition is formulated by assuming the system initially in the lower spin state

$\hat{\rho}\,(t=0) = \hat{\rho}_{\downarrow\downarrow}\,|\downarrow\rangle\,\langle\downarrow|$. Experimentally this is achieved by optical pumping. With this and the initial statement $\Omega \ll \Gamma$ equations 2.64, 2.65 and 2.66 are solved by using an integrating factor. This is done in the following starting from equation 2.65. Taking the term $\frac{\Gamma}{2}\hat{\rho}_{\uparrow\downarrow}$ to the left side and multiplying the equation with the integrating factor $e^{\Gamma/2\,t}$ one gets

$$e^{\Gamma\,t/2}\,\frac{\mathrm{d}\hat{\rho}_{\uparrow\downarrow}}{\mathrm{d}t} + \frac{\Gamma}{2}e^{\Gamma\,t/2}\,\hat{\rho}_{\uparrow\downarrow} = -ie^{\Gamma\,t/2}\,\Omega\left(\hat{K}\,\hat{\rho}_{\downarrow\downarrow} - \hat{\rho}_{\uparrow\uparrow}\,\hat{K}\right) \tag{2.67}$$

Associating $M(t) = e^{\Gamma\,t/2}$ and using the inverse product rule this simplifies to

$$\frac{\mathrm{d}}{\mathrm{d}t}\left(e^{\Gamma\,t/2}\,\hat{\rho}_{\uparrow\downarrow}\,(t)\right) = -ie^{\Gamma\,t/2}\,\Omega\left(\hat{K}\,\hat{\rho}_{\downarrow\downarrow}\,(t) - \hat{\rho}_{\uparrow\uparrow}\,(t)\hat{K}\right). \tag{2.68}$$

Integrating the equation in t and dividing by the integrating factor afterwards one retrieves

$$\hat{\rho}_{\uparrow\downarrow}\,(t) = -i\Omega e^{-\Gamma\,t/2}\int_0^t e^{\Gamma\,t'/2}\,\left(\hat{K}\,\hat{\rho}_{\downarrow\downarrow}\,(t') - \hat{\rho}_{\uparrow\uparrow}\,(t')\hat{K}\right)\mathrm{d}t'. \tag{2.69}$$

Now integrating by parts gives

$$\begin{aligned}\hat{\rho}_{\uparrow\downarrow}\,(t) = -i\frac{2\Omega}{\Gamma}&\left(\left(\hat{K}\,\hat{\rho}_{\downarrow\downarrow}\,(t) - \hat{\rho}_{\uparrow\uparrow}\,(t)\hat{K}\right) - e^{\Gamma\,t/2}\,\hat{K}\right)\\ &+ i\frac{2\Omega}{\Gamma}e^{-\Gamma\,t/2}\int_0^t e^{\Gamma\,t'/2}\,\left(\hat{K}\,\frac{\mathrm{d}\hat{\rho}_{\downarrow\downarrow}\,(t')}{\mathrm{d}t'} - \frac{d\hat{\rho}_{\uparrow\uparrow}\,(t')}{dt'}\hat{K}\right)\mathrm{d}t'.\end{aligned} \tag{2.70}$$

The second term on the right side will be neglected as it turns out by integrating once more to have an additional factor of $1/\Gamma$ and thus will be small. Following these steps for all three differential equations 2.64, 2.65 and 2.66 we retrieve

$$\hat{\rho}_{\uparrow\downarrow}\,(t) \simeq -i\frac{2\Omega}{\Gamma}\left[\left(\hat{K}\,\hat{\rho}_{\downarrow\downarrow}\,(t) - \hat{\rho}_{\uparrow\uparrow}\,(t)\hat{K}\right) - e^{-\Gamma\,t/2}\hat{K}\right] \tag{2.71}$$

$$\hat{\rho}_{\downarrow\uparrow}\,(t) \simeq -i\frac{2\Omega}{\Gamma}\left[\left(\hat{K}^\dagger\,\hat{\rho}_{\uparrow\uparrow}\,(t) - \hat{\rho}_{\downarrow\downarrow}\,(t)\hat{K}^\dagger\right) + e^{-\Gamma\,t/2}\hat{K}^\dagger\right] \tag{2.72}$$

$$\hat{\rho}_{\uparrow\uparrow}\,(t) \simeq -i\frac{\Omega}{\Gamma}\left(\hat{K}\,\hat{\rho}_{\downarrow\uparrow}\,(t) - \hat{\rho}_{\uparrow\downarrow}\,(t)\hat{K}^\dagger\right). \tag{2.73}$$

The terms proportional to $\exp\left(-\Gamma\,t/2\right)$ can be neglected as $t \gg 1/\Gamma$ for the time of interest. Inserting these results in equation 2.63 and neglecting all terms that are smaller than Ω^2/Γ results in the desired equation

$$\frac{\mathrm{d}\hat{\rho}_{\downarrow\downarrow}}{\mathrm{d}t} = \frac{4\Omega^2}{\Gamma}\hat{K}\,\hat{\rho}_{\downarrow\downarrow}\,\hat{K}^\dagger - \frac{1}{2}\frac{4\Omega^2}{\Gamma}\left\{\hat{K}^\dagger\,\hat{K}\,,\hat{\rho}_{\downarrow\downarrow}\right\}_+. \tag{2.74}$$

This result is reminiscent of the non-unitary part of the Lindblad equation 2.61 with $\hat{K}$ in the role of a new Lindblad operator $\hat{L}'$ and the decay rate $4\Omega^2/\Gamma$ with

$$\hat{L}' = \frac{2\Omega}{\sqrt{\Gamma}}\hat{K}\,. \tag{2.75}$$

As no unitary part exists the steady state of this process is simply given by

$$\hat{K} \, |\psi\rangle = 0. \tag{2.76}$$

As shown in the next section, this feature may be exploited to prepare quantum states via dissipation.

2.5 Dissipative State Preparation

Noticeable the steady state $|\psi\rangle$ of equation 2.74 must obey

$$\hat{K} \, |\psi\rangle = 0. \tag{2.77}$$

This steady state is a *dark state* [AGMO76], as no excitation is driven for this state. This is important, as this provides the possibility to stabilize pure states. By constructing the necessary couplings $\hat{\sigma}_- \, \hat{K}$ in the lab, it is thus possible to drive the system from an arbitrary[4] initial state into a desired state $|\psi\rangle$. This is the essence of dissipative state preparation (DSP), also in other systems, not just for motional states.
A steady state could also be a statistical mixture of states, e.g. in the case of a cooling process balancing a heating process, in which case the phase would be random. The additional requirement that the state must be dark is essential to the scheme. It must also be unique[5]. As discussed by Carvalho *et al.* [CMdMFD01], the stabilization of a specific state through this *engineered environment* essentially makes this state a new *pointer state* [Zur91, Zur03], thus stabilizing it against other influences. This theoretical statement has a clear experimental consequence: If the state is perturbed during the DSP (an ion maybe by a collision with a molecule in the background gas), it will get driven to the pointer state nonetheless, it might take a longer time, but it will reach, in principle, unit fidelity eventually. Thus the state is not only prepared, but also *protected* as long as the engineered environment is in effect. A second consequence from the statement is, that the engineered environment must be dominating the dynamics. It must drive the system into the final state faster than any other process can perturb it. The time constant of the pumping process Γ_{DSP} can be seen from equation 2.74 to be

$$\Gamma_{\mathrm{DSP}} = \frac{2\Omega^2}{\Gamma} \tag{2.78}$$

[4] In the experiments described in chapter 5, the ion needs to be first cooled via Doppler cooling into the Lamb-Dicke regime before the dissipative state preparation is possible. This is not a very strong restriction though, as Doppler cooling is in general fast and reliable.

[5] de Matos Filho and Vogel [dMFV96] proposed a scheme to stabilize Schrödinger-cat states [MMKW96], with the drawback of the scheme, that two versions of the protected state could mix under the influence of a perturbing (natural) environment and that the final state depends on the initial state. A possible counter to this mixing is proposed in section 7.2.2

This sets limits on the fidelities of the states created by this technique. In principle it would be best if the process is fast, and thus the final state fidelity higher. So the coherent coupling Ω should be strong and the decay Γ fast. In the experimental implementation though other processes not covered by this simple description come into play. For the squeezed states prepared limiting factors are discussed in section 5.2.6.
In the following sections the experimental implementation of the scheme is laid out. Section 2.5.1 describes the often used technique of motional sideband cooling of trapped ions to prepare the motional ground state, which is a basic example of DSP. In section 2.5.2 the fundamental implementation of the main experiments performed as part of this thesis is described, where energy-eigenstate superpositions are prepared by DSP. The final section (2.5.3) describes a new concept developed from the DSP experiments, which allows fast measurements of the created states' fidelity and manipulations directly in the eigenbasis of the newly created states.

2.5.1 Ground State Cooling

To cool an ion to the motional ground state is probably the simplest example of dissipative state preparation. It was first performed by D. J. Wineland and co-workers in 1995 [MMK+95] and is used in many trapped ion experiment. It is necessary for most experiments relying on the motion of the ion, which includes most experiments in trapped ion quantum computing.
To fulfill equation 2.77 for the motional ground state, $\hat{K}$ needs to be the destruction operator $\hat{a}$ of the harmonic oscillator as

$$\hat{a}\ |0\rangle = 0. \tag{2.79}$$

To implement the couplings $\hat{\sigma}_+ \hat{K} = \hat{\sigma}_+ \hat{a}$ is now straight forward, as this is simply the red sideband, which means that the general spin-motion Hamiltonian (equation 2.58) needs to be replaced with the red sideband Hamiltonian (equation 2.54). A description of the experimental procedures of ground state cooling is given in section 4.3.3.

2.5.2 Displaced Squeezed State Cooling

Ground state cooling can now be extended to other motional states prepared as final states as proposed by Cirac *et al.* [CPBZ93]. Assuming a unitary operation $\hat{U}$, equation 2.79 can be modified to

$$\hat{U}\,\hat{a}\,\hat{U}^\dagger\,\hat{U}\ |0\rangle = 0, \tag{2.80}$$

without loss of generality. Now thinking of Ψ with

$$\Psi = \hat{U}\ |0\rangle \tag{2.81}$$

as a desired state to be prepared, the engineered couplings needed for the DSP are given by

$$\hat{\sigma}_+ \hat{K} = \hat{\sigma}_+ \hat{U} \hat{a} \hat{U}^\dagger . \tag{2.82}$$

For the experiments described in this thesis the unitary transformation is chosen as

$$\hat{U} = \hat{S}(\xi)\hat{D}(\alpha) \tag{2.83}$$

with the displacement and squeezing operators defined as

$$\hat{D}(\alpha) \equiv e^{\alpha\hat{a}^\dagger - \alpha^*\hat{a}} \quad \hat{S}(\xi) \equiv e^{\left(\xi^*\hat{a}^2 - \xi\hat{a}^{\dagger 2}\right)/2}, \tag{2.84}$$

where α is the complex displacement in phase space and ξ is the complex squeezing amplitude (see e.g. [Sch01]). With this, the prepared state is a *displaced squeezed state*[6] (DSS) defined as

$$|\psi_{\mathrm{DSS}}\rangle = \hat{S}(\xi)\hat{D}(\alpha)|0\rangle . \tag{2.85}$$

To implement the Hamiltonian for a DSS, equation 2.82 is used and the motional operator $\hat{K}$ is then written as

$$\hat{K}_{\mathrm{DSS}} = \hat{S}(\xi)\hat{D}(\alpha)\hat{a}\,\hat{D}(\alpha)^\dagger\hat{S}(\xi)^\dagger \tag{2.86}$$

Applying the Baker-Campbell-Hausdorff formula once gives

$$\hat{K}_{\mathrm{DSS}} = \hat{S}(\xi)\,(\hat{a} - \alpha\mathbb{1}_m)\,\hat{S}(\xi)^\dagger \tag{2.87}$$

and applying it a second time results in

$$\hat{K}_{\mathrm{DSS}} = \cosh r\ \hat{a} + e^{i\Theta}\sinh r\ \hat{a}^\dagger - \alpha\,\mathbb{1}_m . \tag{2.88}$$

The spin-motion Hamiltonian used for environment engineering is then written as

$$\hat{H}_{\mathrm{ee}} = \hbar\,\Omega\left(\cosh(r)\ \hat{a} + e^{i\Theta}\sinh(r)\ \hat{a}^\dagger - \alpha\,\mathbb{1}_m\right)\hat{\sigma}_+ + \mathrm{h.c.}, \tag{2.89}$$

which consists of components of the carrier ($\mathbb{1}_m\,\hat{\sigma}_+$), red sideband ($\hat{a}\,\hat{\sigma}_+$), and blue sideband ($\hat{a}^\dagger\,\hat{\sigma}_+$) Hamiltonians with defined phase relationships, which are the coupling terms of the basic Hamiltonians introduced in section 2.4.1. Other states may be stabilized using this technique as described by Carvalho *et al.* [CMdMFD01], although with the expense of more terms, also including higher orders of $\hat{a}$ and $\hat{a}^\dagger$.
The experiments demonstrating the preparation of different versions of DSSs are described in chapter 5.

[6] A second definition of the DSS is possible with first the squeezing, second the displacement operator applied, in some sense a 'squeezed displaced state': $|\psi_{\mathrm{SDS}}\rangle = \hat{D}(\alpha)\hat{S}(\xi)|0\rangle$. The two states $|\psi_{\mathrm{SDS}}\rangle$ and $|\psi_{\mathrm{DSS}}\rangle$ are not the same for given α and ξ, but with redefined α' and ξ' it is possible to describe the same state. In this thesis only the definition given in the main text is used.

2.5.3 Generalized Fock State Ladders

The transformation $\hat{U}$ introduced for the DSS may also be viewed in a more general context: as a basis transformation. With the energy eigenstates forming the energy-eigenstate basis $B = \{|0\rangle, |1\rangle, ...\}$, the basis $B_{\hat{U}}$ may be formulated, which is connected to B by the unitary transformation $\hat{U}$ and its eigenvectors are $\hat{U}\ |n\rangle = |n\rangle_{\hat{U}}$. An operator $\hat{O}$ acting in the natural basis B is transformed according to $\hat{O}_{\hat{U}} = \hat{U}\,\hat{O}\,\hat{U}^\dagger$. The transformed basis $B_{\hat{U}}$ will also be called *engineered basis* in this thesis. With this a transformed version of the Jaynes-Cummings-Hamiltonian/red sideband Hamiltonian, given in equation 2.54, may be formulated as

$$\hat{H}_- = \hbar\Omega\left(\hat{K}^\dagger\,\hat{\sigma}_- + \hat{K}\,\hat{\sigma}_+\right) \tag{2.90}$$

with $\hat{K} = \hat{U}\,\hat{a}\,\hat{U}^\dagger$ and $\hat{K}^\dagger = \hat{U}\,\hat{a}^\dagger\,\hat{U}^\dagger$. Also formulating a transformed anti-Jaynes-Cummings Hamiltonian (blue sideband Hamiltonian, equation 2.55)

$$\hat{H}_+ = \hbar\Omega\left(\hat{K}\,\hat{\sigma}_- + \hat{K}^\dagger\,\hat{\sigma}_+\right). \tag{2.91}$$

Applying these Hamiltonians to eigenstates of $B_{\hat{U}}$ will display the same dynamics as the original versions applied to the energy eigenstates: for a pure eigenstate we get single-frequency Rabi-oscillations. For instance if applied to an ion in the spin down state and the ground state of the transformed basis $|\downarrow, 0\rangle_{\hat{U}}$ will lead to single frequency Rabi oscillations between the states $|\downarrow, 0\rangle_{\hat{U}}$ and $|\uparrow, 1\rangle_{\hat{U}}$. This is analog to Rabi-flopping on the blue sideband of an ion driving the transition $|\downarrow, 0\rangle \leftrightarrow |\uparrow, 1\rangle$.
There is a fundamental difference though of the energy eigenstates to the DSSs. The energy eigenstates have no well defined phase, which makes the phase of the laser for the Rabi flops irrelevant. For the DSS both the displacement and the squeezing define a phase and the phase of the Hamiltonians must be matched to the state. This is at first an experimental challenge, but also provides an opportunity: A successful measurement of single frequency Rabi oscillations verifies the stable phase relationship between the state and the laser. As the laser's phase stability may be proven otherwise (e.g. by a Ramsey experiment, described in section 4.5 or a measurement of is linewidth by comparison to a second laser of similar or better linewidth) this results in a verification of the state's phase. As the Rabi flops also verify the populations and stability of the state, a fidelity can be derived from the measurement. This technique is used experimentally in section 5.2.3, resulting in the first quoted fidelity measurement of squeezed motional states of trapped ions.
A Fidelity measurement is in principle also possible by performing a full motional state tomography [PWC+96]. This is a very time-consuming measurement though. The presented technique reduces the measurement time by a large amount. The shortcoming of this technique compared to a full state tomography is that it is hard to make any evaluation of the part of the state that

does not match the desired state. A full state tomography characterizes the whole state, and thus does not display this problem. A possibility to overcome this shortcoming, but still simplify traditional motional state tomography is presented as outlook in chapter 7.

A second application of these Hamiltonians is apparent: As the DSP presented here only creates displaced squeezed ground states, the transformed Hamiltonians 2.90 and 2.91 can be used to create excited versions of these states and superposition of them. By first preparing the ground state of the engineered basis and subsequently applying $\hat{H}_+$ for a given amount of time the state $|\uparrow, 1\rangle_{\hat{U}}$ may be prepared as

$$\exp\left(-\frac{2\pi i\,\hat{H}_+}{\hbar\Omega}\right)|\downarrow, 0\rangle_{\hat{U}} = |\uparrow, 1\rangle_{\hat{U}}\ . \tag{2.92}$$

Experiments were performed to create squeezed states of $n = 4$ and a superposition-state of $n = 0$ and $n = 2$. The experimental details and an analysis of the final states are given in chapter 6.

Chapter 3

Apparatus

This chapter describes the experimental apparatus built as part of this thesis and used for the experiments covered in later chapters. In detail it describes the simulation and fabrication of the wafer trap, the vacuum chamber including the optical system for imaging and detecting ions and the helical resonator used to supply the radio frequency drive for the trap. Also described are the laser setup creating the required frequencies and the delivery of the laser beams to the trap.

3.1 General Design Considerations

The apparatus was built with the goal of performing experiments covering quantum computation and simulation at high fidelities. A scalable approach is pursued to quantum computation based on the 'quantum charge-coupled device' (qccd) architecture' of D. Wineland proposed in [WMI+98, KCW02], where a segmented trap array is used to shuttle, split and combine ion strings, have them interacting with laser light in dedicated zones and store them in others. The multi-species approach facilitates this idea as one species may be used as 'refrigerator' ions for sympathetic cooling to keep the motion of the ions cold but at the same time leave the internal quantum state of the 'logic' ions undisturbed [KKM+00, Hom13]. For quantum simulation the two species setups also offers advantageous routes, as independent control of each species can be combined with interactions between species to form complex, dynamical quantum systems. To address the high fidelities in quantum computing $^{9}Be^{+}$ was chosen to be the 'logic' ion, as with its hyperfine structure a field independent qubit transition is available, which offers long coherence times in the presence of magnetic field noise [Lan05]. In this scenario $^{40}Ca^{+}$ would serve as the refrigerator ion. For quantum simulation on the other hand the full independent control and readout is a considerable advantage over systems with e.g. only one ion having the possibility of a spin readout, necessitating quan-

tum logic readout [SRL+05] for the other species as often the case for atomic clocks based on ions [CHK+10]. The two species approach is technically demanding as the different properties of both species need to be considered. A major point are the different optical frequencies needed to address and detect both species. Two laser systems are needed including optics for delivering the laser light to the ion, as no standard components exist that cover all used wavelengths (mainly NIR and UV). To detect both species an imaging system was built. Its main component is a multi-element lens, capable of imaging $^{9}Be^{+}$ and $^{40}Ca^{+}$ simultaneously. To make better use of the multiple zones of the trap the imaging system is doubled, imaging different zones of the trap. The constant offset magnetic field of $\sim 119\,\mathrm{G}$ chosen for the field independent transition for $^{9}Be^{+}$ put $^{40}Ca^{+}$ in a non-traditional regime. Also the high mass ratio of 9:40 is not well studied, mainly affecting the trapping fields and sympathetic cooling. Of major importance is micromotion compensation, which is also needed for single species experiments but is of higher importance for multiple species and longer traps. The mass difference of two species leads to a stronger displacement of the lighter species, deforming the linear chain of ions and introducing couplings between the radial and axial modes of motion. In long traps the stray field in general changes along the trap axis, requiring different compensation fields along the trap. Therefore segmented bias electrodes were used in the trap to give best control over stray fields. During the design phase of the experiment the possibility of cooling the trap with LN_2 was investigated. This could reduce heating rates by a considerable amount [DOS+06] and would be expected to reduce collision rates of trapped ions with background gas molecules, which is of importance for experiments with long chains of ions. A cold finger was not implemented at the time of construction but the setup allows for a upgrade at later time without changing the construction much. The details are discussed in the outlook chapter in section 7.2.4.

3.2 Trap

As seen in section 2.3 and equation 2.19 the strength of the radial confinement depends on the rf drive frequency, the applied amplitude of the rf drive voltage and the trap geometry. Smaller dimensions for the trap electrodes provide stronger confinement. The size and distance of the dc electrodes from the ion also changes how much dc voltage has to be applied to provide axial confinement. For the trap constructed as part of this thesis this is not an issue because the voltages are in the range of volts to tens of volts, which are easily generated. The more important impact is on the possibility of splitting an ion chain, for which closer electrodes allow for the needed higher harmonic components to be stronger (section 3.2.1).
These considerations would say that ion traps should be made as small as pos-

sible. This is countered by the so-called anomalous heating. It describes noise that heats trapped ions, stronger than what Johnson–Nyquist noise from finite resistance of the trap electrodes and accompanying circuitry predicts. The following scaling for the heating rate from the ground state can be derived assuming fluctuating patch potentials on the electrodes: $\bar{n} \propto d^{-\gamma}$, $\gamma = 4$ with d the minimal electrode-ion distance [TKK$^+$00, DOS$^+$06]. Experimentally this is difficult to confirm as too many factors are involved in building ion traps, hence every ion trap might have different base values. In an experiment with a trap with movable electrodes a scaling of $\gamma = 3.5(1)$ was observed [DOS$^+$06]. Recent research has shown reduction of heating rates with cooling traps [DOS$^+$06, LGA$^+$08] and cleaning electrode surfaces [AGH$^+$11, HCW$^+$12]. To keep the heating rate at an acceptable level but still have good confinement we chose a slightly larger electrode ion distance (184 µm) than for the trap described in [Jos10] (electrode ion distance: 141 µm, heating rate: 0.25 quanta/ms for a single $^9Be^+$ ion with a trap frequency of 3 MHz, spectral noise density: $\omega S_E(\omega) = 2.2 \times 10^{-5}\,\mathrm{m^2\,V^{-2}\,s^{-2}}$), which has been used for experiments with $^{24}Mg^+$ and $^9Be^+$ ions. This would yield a predicted reduction of a factor of 2.5 of the heating rate assuming the $d^{-3.5}$ scaling of the heating rate with distance. As mentioned this can only be seen as a rough orientation, since experience has shown large fluctuations of heating rates for different ion traps, not following any particular scaling law closely [DNM$^+$11].

3.2.1 Trap Simulation

To simulate a Paul trap the static confinement and the rf confinement needs to be calculated. As shown in section 2.3 the rf confinement can be described by a static pseudo-potential calculated from the potential Φ_{rf} with the time dependent term $\cos\omega_{\mathrm{rf}}t$ set to 1, yielding the result

$$\Phi_{\mathrm{pp}}(x,y,z) = |q|\,\frac{|\nabla\Phi_{\mathrm{rf}}(x,y,z)|^2}{4m\Omega_{\mathrm{rf}}^2}. \tag{3.1}$$

A simple approach is to solve Laplace equation in a region of space for a given trap geometry numerically for one dc electrode i set to a normalized electrical potential (1 V) and all other electrodes to ground. If this is performed for all N dc electrodes this yields the norm-potentials $\tilde{\Phi}_i(x,y,z)$ with $i \in \{1,...,N\}$ (the $\tilde{}$ indicating the normalized version). For the pseudo-potential all rf electrodes are set to (1 V) and all dc electrodes set to ground again calculating the potential $\tilde{\Phi}_{\mathrm{rf}}$. From this the pseudo-potential $\tilde{\Phi}_{\mathrm{pp}}$ is calculated according to equation 3.1 with $m = 1$ amu, $\Omega_{\mathrm{rf}} = 2\pi \times 1$ MHz and $q = 1e$. To calculate now the full potential for a single charged ion of mass m, with a set of dc voltages U_i, the rf voltage U_{rf} and the rf frequency ω_{rf} applied to the electrodes, the superposition of the potentials is formed with the voltages as

weights and scaling the pseudo-potential with the given values as follows

$$\Phi(x,y,z) = \sum_{n=1}^{N} \frac{U_i}{1\,\mathrm{V}}\,\tilde{\Phi}_i(x,y,z) + \frac{1\,\mathrm{amu}}{m}\left(\frac{U_{\mathrm{rf}}}{1\,\mathrm{V}}\frac{2\pi\times 1\,\mathrm{MHz}}{\omega_{\mathrm{rf}}}\right)^2 \tilde{\Phi}_{\mathrm{pp}}(x,y,z). \tag{3.2}$$

This way a trap geometry only needs to be simulated once and may then be analysed with different settings for the dc voltages, the rf voltage, ion species (mass) and rf frequency. This result can now be analysed to calculate the trap frequencies and other properties of the trap.
For a given trap geometry the required static potentials were calculated by the boundary element method [SPM+10] to solve the Laplace equation for the given electrode geometry.[1]
Two main aspects of the trap were analysed: the radial confinement and the possibility to realize large quartic terms for splitting of ion chains. Further the capacitance of the trap was calculated from the simulation.

Radial Confinement

As derived in section 2.3, the confinement of the pseudopotential is depending on the mass of the ion. This results in two different sets of frequencies for the two species. In general high radial trap frequencies are preferred, as this helps with cooling the ions, lowers anomalous heating and allows for longer axial chains. As can be seen from equation 2.19 the radial frequencies depend on the applied voltage, the geometry, the mass of the ion, and the frequency of the applied rf voltage. The limit to the applied rf voltage is usually fixed to a value which does not lead to electrical breakdown and potentially damages the trap. For our trap dimensions a voltage below $800\,\mathrm{V_{p\text{-}p}}$ is assumed to be safe, using $740\,\mathrm{V_{p\text{-}p}}$ in the simulations to drive the trap. The mass is also fixed by the choice of the ion species and the geometry is fixed by the heating rate consideration for the electrode ion distance and by the manufacturing process in terms of electrode shape. This leaves the rf frequency as the only free parameter, where decreasing the rf frequency increases the trap frequencies. Looking at the stability criteria for rf traps (see e.g. [LBMW03]), its clear that Ω_{rf} can not be reduced arbitrarily. From past experience a conservative value of $\omega_{\mathrm{radial}}/\Omega_{\mathrm{rf}} \leq 0.2$ has proven to be safe for micro-fabricated ion traps used with multiple species [Win11]. From the simulation a stable point of operation was found to be 90 MHz for the drive frequency, see fig. 3.1 for the simulated frequency dependence. This results in secular frequencies of 17.4 MHz (3.9 MHz) for $^{9}\mathrm{Be}^{+}$ ($^{40}\mathrm{Ca}^{+}$) with $\omega_{\mathrm{radial}}/\Omega_{\mathrm{rf}} = 0.19$ (0.04). From the simulation it is also possible to extract the angle of the radial modes. An example of a simulated potential is shown in figure 3.2.

[1] The simulation code was developed in the NIST ion storage group, using the boundary element package of fastlab (www.fast-lab.org).

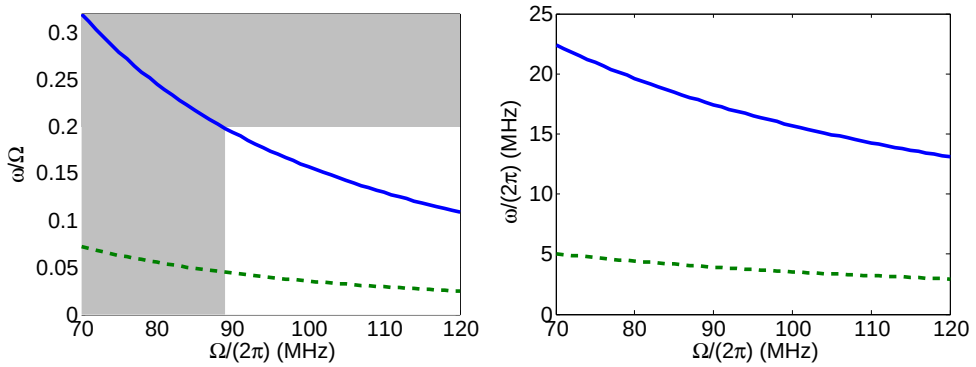

Figure 3.1: Results for the simulation of radial secular frequency in dependence of the drive frequency Ω_{rf} The blue lines are for $^{9}\mathrm{Be}^{+}$, the green dashed lines for $^{40}\mathrm{Ca}^{+}$. The left plot shows the ratio of the secular frequency ω_{rf} to the drive frequency Ω_{rf} vs the drive frequency. The grey area is excluded due to the chosen stability boundary of $\omega_{\mathrm{rf}}/\Omega_{\mathrm{rf}} \leq 0.2$. The right plot shows the secular frequency vs the drive frequency.

Splitting of Ion Chains

To split an ion chain potentials have to be shaped to change the potential with the combined ion string from a single well to a double well with the two separated strings [HS06]. This operation can be described by time dependent quadratic and quartic potentials

$$\Phi(z,t) = a_2(t)\, z^2 + a_4(t)\, z^4, \tag{3.3}$$

where x is the position, t is the time, $a_2(t)$ and $a_4(t)$ are the time dependent strengths of the quadratic and quartic potentials. $a_2(t)$ is positive for t smaller than a critical time t_{c}, negative for $t > t_{\mathrm{c}}$ and zero for $t = t_{\mathrm{c}}$, $a_4(t)$ only changes monotonous and slowly with time and is positive for all t. The single well is formed for $t < t_{\mathrm{c}}$ and the double well for $t > t_{\mathrm{c}}$. When $t = t_{\mathrm{c}}$ the confinement is only given by the quartic term, which is the moment of lowest confinement in the sequence. To keep this confinement high is key to stability and low motional heating during the separation of ions.
At least five electrodes are needed to form the double well. The electrode geometry is depicted in figure 3.3 and the separation sequence in figure 3.4. As shown in [HS06] the size of these trap electrodes and their distance to the ion determines the strength of the quartic term. As the distance of the electrodes to the ions is already fixed by the constraints from the heating rate as discussed in section 3.2, the only free parameter left to control it the electrode width. To optimize the width of the three separation electrodes several traps with different widths were simulated. For each simulated trap voltage configurations of $V_1 = V_5 = 2\,\mathrm{V}$ and $V_2 = V_4 = -2\,\mathrm{V}$ were used, changing V_3 to determine the voltage were a_2 changes sign, and extract a_4 for

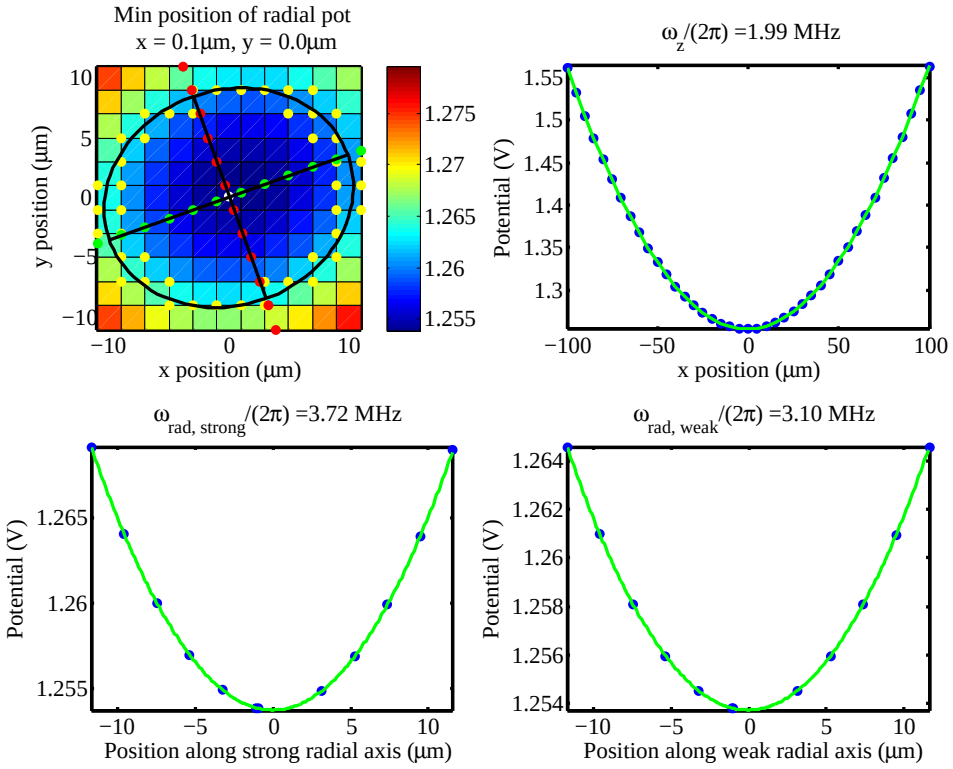

Figure 3.2: Sample results of the trap simulation. The plot in the top left shows the superimposed pseudo- and static potential in the radial plane with the yellow point used for fitting an ellipse, the black lines showing the result of the ellipse fit. From this fit the potential along the strong and weak radial trapping axes gets extracted from the data (green and red points). In the top right the potential along the axial direction is shown with a fitted parabola and the resulting trap frequency. The bottom plots show the extracted potential along the radial axes with parabolic fits and their resulting trapping frequencies.

this setting. From this the trap frequency was calculated. Figure 3.5 shows the result of the simulation, which gives an optimal finger width of 155 µm for the otherwise unchanged trap geometry. It should be noted that the drop of the confinement is not very large for non-optimal finger widths, as the trap frequency drops by only $\sim 13\,\mathrm{kHz}$ for a finger with 45 µm larger or smaller than the optimum. For comparison the trap frequency for two $^{40}Ca^{+}$ ions was calculated with the same voltage bounds as [KRS+14] giving the voltage configuration $V_1 = V_5 = 10\,\mathrm{V}$, $V_2 = -9.915\,\mathrm{V}$, $V_3 = -1.6\,\mathrm{volt}$ and $V_4 = -10\,\mathrm{V}$, where the difference of V_2 and V_4 is due to the center of the separation zone being not in the center of the trap array, leading to a slight asymmetry. This

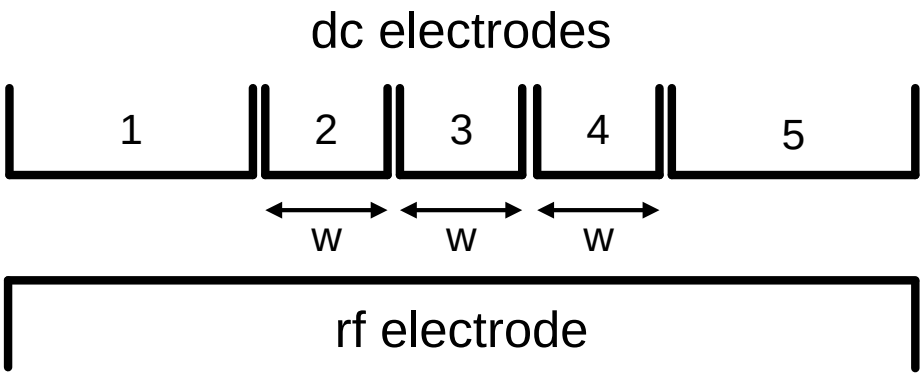

Figure 3.3: Electrodes needed for splitting. For the optimization the width w of electrodes 2, 3 and 4 are varied.

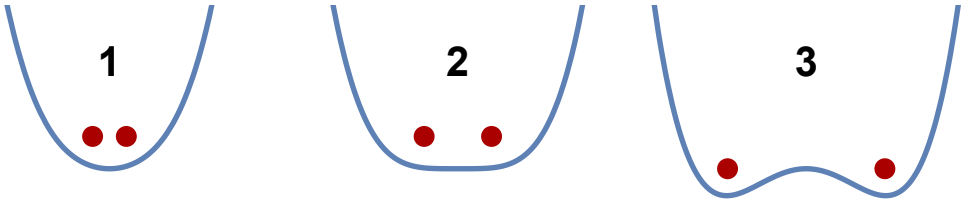

Figure 3.4: Schematic of the changing potential to split an ion chain. At the start (1) the ions reside in a single, mainly quadratic well, which is changed to a mainly quartic well (2), and finally to a double well with the ions in separate wells (3).

configuration results in a trap frequency of

$$\omega_{z,\text{quartic}} = 2\pi \times 250\,\text{kHz}, \tag{3.4}$$

which is comparable to values used in recent experiments that achieved splitting of ion chains [BGL+12, KRS+14].

Capacitance Estimation

An estimation of the trap's capacitance was made by using the trap simulation. As the first step in the simulation is to divide the trap into small polygons and calculate their surface charged given a certain potential, the capacitance of the trap electrodes could be extracted. The capacitance of the rf electrodes to ground (all other DC electrodes) was calculated to $\simeq 2\,\text{pF}$. For the dc electrodes the values range from $\simeq 1\,\text{fF}$ for the smallest electrodes to $\simeq 20\,\text{fF}$ for the larger electrodes. With assumed 350 V peak rf voltage at 90 MHz this results in a peak current of $\simeq 400\,\text{mA}$ for the rf electrode and $\simeq 4\,\text{mA}$ to

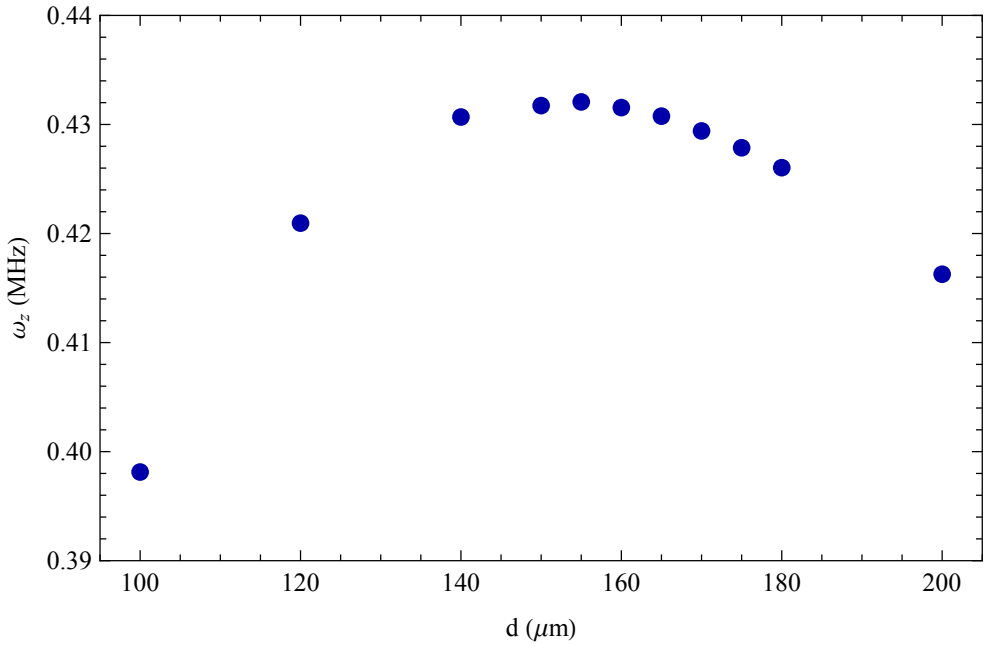

Figure 3.5: Simulation result for traps with different electrode width. For two $^9Be^+$ ions in the purely quartic potential the lower trap frequency is given. Voltage configurations of $V_1 = V_5 = 2\,\mathrm{V}$ and $V_2 = V_4 = -2\,\mathrm{V}$ were used, changing V_3 to determine the voltage were a_2 changes sign, and extract a_4 for this setting.

$\simeq 0.2\,\mathrm{mA}$ for the dc electrodes. This is of importance for the wirebonding as 400 mA is a considerable current.

3.2.2 Trap Design

Trap Wafers

The trap wafers are segmented to feature two loading zones, three experimental/interaction/storage zones and two shuttling and separation zones, see figures 3.7 for the geometry. Two loading zones were used for multiple reasons. With one oven for each species and the need of a backup oven for each in case of failure four ovens are needed. Collimating their atomic beams into the same zone without obstructing imaging or laser beam access was not possible. Two loading zones circumvent this problem. Putting them at opposing ends of the trap array might be advantageous for complex experiments with multiple ions from both species in multiple zones, as the ions could be loaded in the order needed without reordering them. Another possibility is to separate the loading of the two species. The 235 nm UV light used for the photo-ionization of $^9Be^+$ is observed to induce charging of the trap electrodes, which make loading of $^{40}Ca^+$ difficult or impossible. To keep the setup flexible and be prepared for

(a) 'exploded' view of the trap stack.

(b) CAD drawing of the fully assembled trap on the filter board.

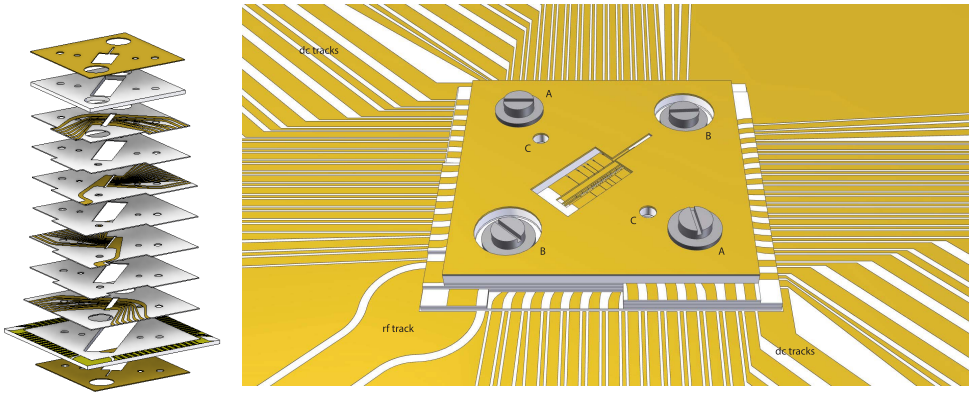

Figure 3.6: Drawing of the full trap stack. An 'exploded' view is shown in (a) with the different layers from top to bottom: top mask wafer, spacer, top shim wafer, spacer, top trap wafer, spacer, bottom trap wafer, spacer, bottom shim wafer, filterboard, bottom mask wafer. In (b) a drawing of the fully assembled trap on the filter board is shown. 'A' denotes the screws clamping all stack layers, 'B' the screws only clamping the trap wafers. 'C' are holes used for alignment pins.

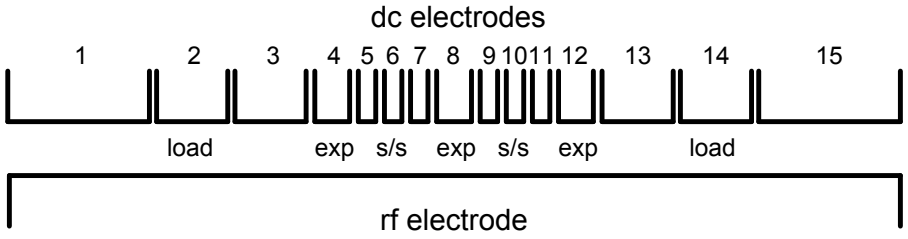

Figure 3.7: Schematic top view of the trap electrodes. The functional zones of the trap are labeled: 'load' for the loading zones, 'exp' for the experimental zones and 's/s' for the shuttling and separation zones. The widths of the dc electrodes are: Electrode 1: 1000 µm, 2 and 3: 500 µm, 4: 300 µm, 5 to 7: 155 µm, 8: 300 µm, 9 to 11: 155 µm, 12: 300 µm, 13 and 14: 500 µm, 15: 1000 µm with 20 µm gaps between the electrodes.

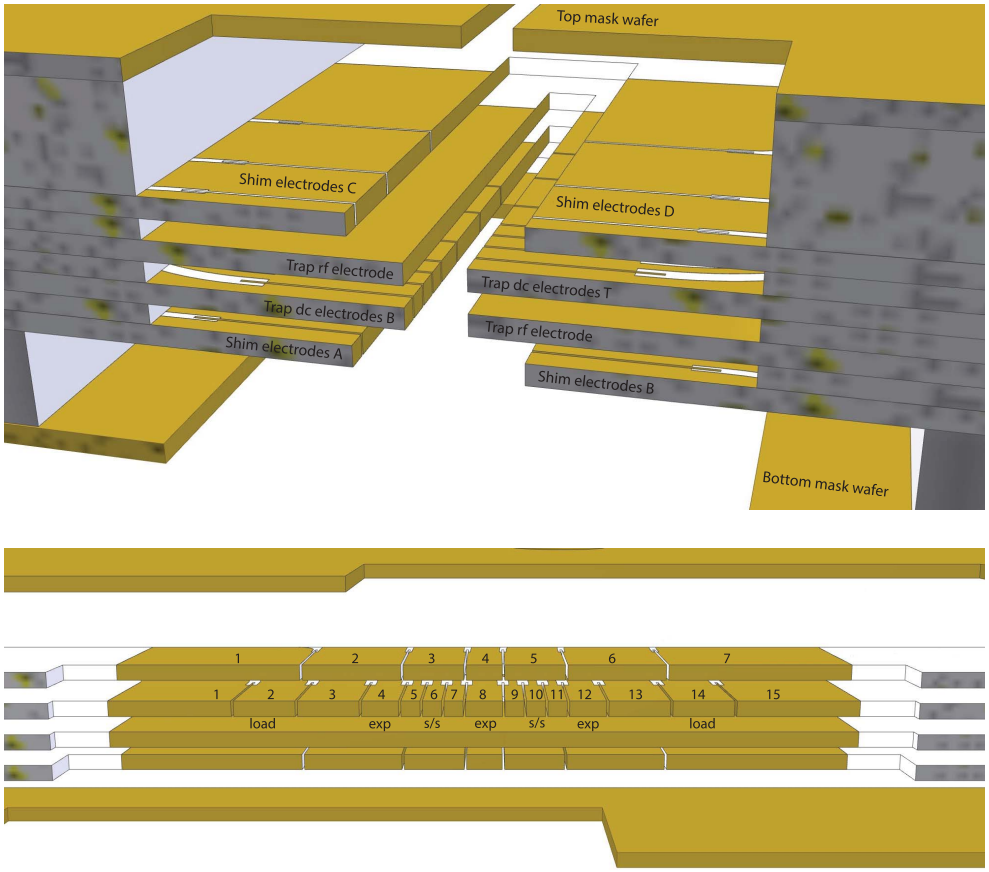

Figure 3.8: Drawing of the trap, cut transverse to the trap axis in the top picture, along the trap axis in the bottom picture. Layers are labeled with the naming convention and numbering scheme for the different electrodes The functional zones of the trap are labeled: 'load' for the loading zones, 'exp' for the experimental zones and 's/s' for the shuttling and separation zones.

all possible cases one atomic source oven for each species was installed on each end of the trap (see also 3.3.1).

Shim Wafers

To null stray electric fields transverse to the trap axis a common approach is to use two bias electrodes. With this approach only one point along the trap axis can be optimally compensated. This is fine as long as the used length of the trap axis is small compared to the change of the stray field along the axis. For long trap arrays this is not a given and compensation for single zones of the trap array is advantageous. Additionally mixed species crystals suffer more severe from micromotion, as discussed in section 2.3.2. To gain more control

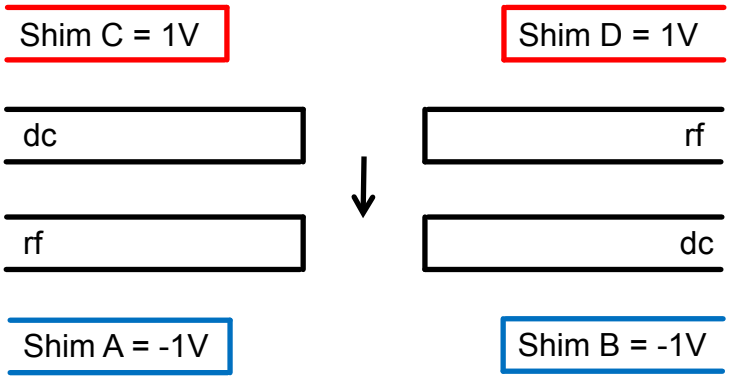

Figure 3.9: Schematic of the shim field simulation. Depicted is a cut view perpendicular to the trap axis. To estimate the produced field by the shim electrodes, they were set to two different configurations (see text), one depicted here. The dc and rf electrodes were set to 0 V. The resulting field in the trap center is depicted as the black arrow.

over the micromotion in different zones of the trap, segmented bias wafers were added to the trap. As can be seen in figure 3.8 there are seven segments along the trap, each composed of four shim electrodes. This segmentation does not mirror the dc electrode segmentation but provides control for each functional unit as labeled in figure 3.7, i.e. experimental zones, separation/shuttling zones, loading zones. This provides reasonable control without having too many dc connections. Strictly only one electrode per segment would have been enough to compensate together with differential voltages on the dc electrodes, but having dedicated shim electrodes and not applying any other voltages to the dc electrodes than those needed for confinement makes the operation of the trap easier when waveforms are used for shuttling ions, as these waveforms are then allowed to stay fixed once optimized, and the day-to-day drifting stray fields are compensated only with the shim electrodes.
To characterize the strength of the fields created by the shim electrodes, these were calculated for two configurations aiming to produce a field perpendicular (parallel) to the trap wafer. For the center of the trap with voltages applied to the shim electrodes (here all shim electrodes along the trap are used and for one quadrant set to the same voltage, i.e. shim electrodes A1 to A7 are set to U_A, B1 to B7 to U_B and so on): $U_A = U_C = +1\,\mathrm{V}, U_B = U_D = -1\,\mathrm{V}$: $E_y = 24.6\,\mathrm{V\,m^{-1}}, E_z = 0.08\,\mathrm{V\,m^{-1}}$ and for $U_A = U_B = -1\,\mathrm{V}, U_C = U_D = +1\,\mathrm{V}$: $E_y = -426\,\mathrm{V\,m^{-1}}, E_z = 0.2\,\mathrm{V\,m^{-1}}$. The geometry for the second voltage configuration is depicted in figure 3.9.

Mask Wafers

To prevent coating of the trap electrodes with $^{9}Be^{+}$ or $^{40}Ca^{+}$ during loading from the atomic source ovens the setup features first a collimation of the atomic beam described in 3.3.1 and a aperture on the trap. This mask wafer, see figure 3.6, has a narrow slit along the direction of the trap axis cutting out all atoms that might hit the trap electrodes. This wafer makes imaging impossible from the side of the wafer, which is why the imaging system may only cover the opposite part of the trap, up to the middle, the blocked part is then imaged with the second imaging system from the other side. For the second loading zone the same mask wafer was installed, limiting the imaging for the second imaging system in the same way, but being covered by the first imaging system. The mask wafers were gold coated and grounded to prevent surface charges to accumulate.

3.2.3 Fabrication

Fabrication of the trap was done following the recipe of R. Blakestad [Bla10] with minor adjustments. The trap is made of a stack of Alumina (Al_2O_3) wafers, which are first laser machined to define the main slot of the linear trap and individual dc electrodes as well as additional features like alignment holes, clearance holes for mounting screws etc. These wafers are then coated with patterns of gold to define the electrodes and contacting tracks. This is done in two steps: First thermal evaporation of gold, then electrolytic deposition to thicken the gold. In a next step the wafers get cut to their final shape using a dicing saw, followed by a cleaning step. Finally the wafer stack gets assembled on a carrier board (also called filter board) and the single electrodes get connected by wire-bonding. The laser machining was performed by Beat Lüscher from Fachhochschule Nordwestschweiz[2]. All other steps were performed at ETHZ, mainly in the research clean room FIRST[3].

Substrate As a substrate material aluminum oxide (Al_2O_3, poly-crystalline) wafers[4] were chosen. Physical dimensions are 2.00(2) inch square and a thickness of $5.0(5) \times 10^{-3}$ inch (127 µm). Both sides of the wafers were polished which is essential for the gold deposition on both faces of the wafer. Initial tests were also taken out with poly-crystalline aluminum nitride (AlN) as it has a more then 5.5 times better heat conductivity ($170\,\mathrm{W\,m^{-1}\,K^{-1}}$), which would have helped with LN_2 cooling of the trap. A drawback is the 5 times worse loss tangent (0.0005 at 1 MHz). The surface roughness of the laser machined edges was poor (judging from light microscopy inspection), which is why this approach was dropped again.

[2] Fachhochschule Nordwestschweiz, http://www.fhnw.ch/technik/ippe/dienstleistung
[3] www.first.ethz.ch
[4] CoorsTek, two-side polished substrate, material name: Superstrate

Laser-Machining To define the structure a picosecond laser-machining technique was used with a wavelength of 355 nm. Initial tests to cut large features (e.g. clearance holes) which do not require critical alignment using a 1 µm wavelength pulsed laser failed. After both laser machining steps the wafers had hair-line cracks and were extremely brittle. Thus the whole structure was cut with the picosecond laser, which took approximately 15 h for a single wafer. After process optimization clean cuts where achieved with a finger separation of 19 µm.

Cleaning To clean the cut wafers a rigorous procedure was used. First a piranha etch (sulfuric acid 95-98% and hydrogen peroxide 30%, 3:1) was done at 95 °C for one hour with the wafer suspended in the etch to clean both top and bottom surface. This was followed by a rinse in (successively) ultrapure water, Acetone, Isopropanol, ultrapure water. The first ultrapure water step is necessary as a direct contact of the residual Piranha etch on the wafer with Acetone would cause a violent reaction. Ultrasonic cleaning broke long fingers off the main wafer and thus could not be applied. In order to avoid damage the etch and rinse liquids were only agitated by hand.

Thermal Evaporation To deposit a first layer of gold for the electrodes and their connection tracks an electron beam evaporation machine was used. Shadow masks were used to define the patterns in two steps on each side of the wafers. In the first step only the electrodes were evaporated, in the second only the electrode connections. The masks were laser-machined from Kapton foil[5] by LaserMicronics[6]. For both deposition steps first a titanium adhesion layer of ≈ 40 nm followed by a gold layer of 1 µm was evaporated. The evaporation was carried out with the wafer rotating and tilted by 13° relative to the atomic beam to coat top and all side faces, including those between the fingers. Although Kapton for the evaporation masks has the advantage of very clean laser-machining cuts it lead to a complication of the process which was not not anticipated. This was strong outgassing in the evaporation chamber partially oxidised the titanium layer which led to bad adhesion of the gold layer, visible by blisters forming on the gold layer in minutes to hours. This was countered by long pumping times before deposition (10 h) as the outgassing reduces over time. Also a thicker titanium layer than common was used as this also lead to better adhesion. For future processes the use of steel masks is recommended (as done by R. Blakestad [Bla10]).

Electroplating To thicken the evaporated gold and close possible gaps electroplating of gold was used. A prior cleaning step with oxygen plasma showed no effect and was left out in the final processing. A single wafer was mounted

[5] DuPont, Kapton 500 HN, thickness: 127 µm
[6] http://www.lasermicronics.de/

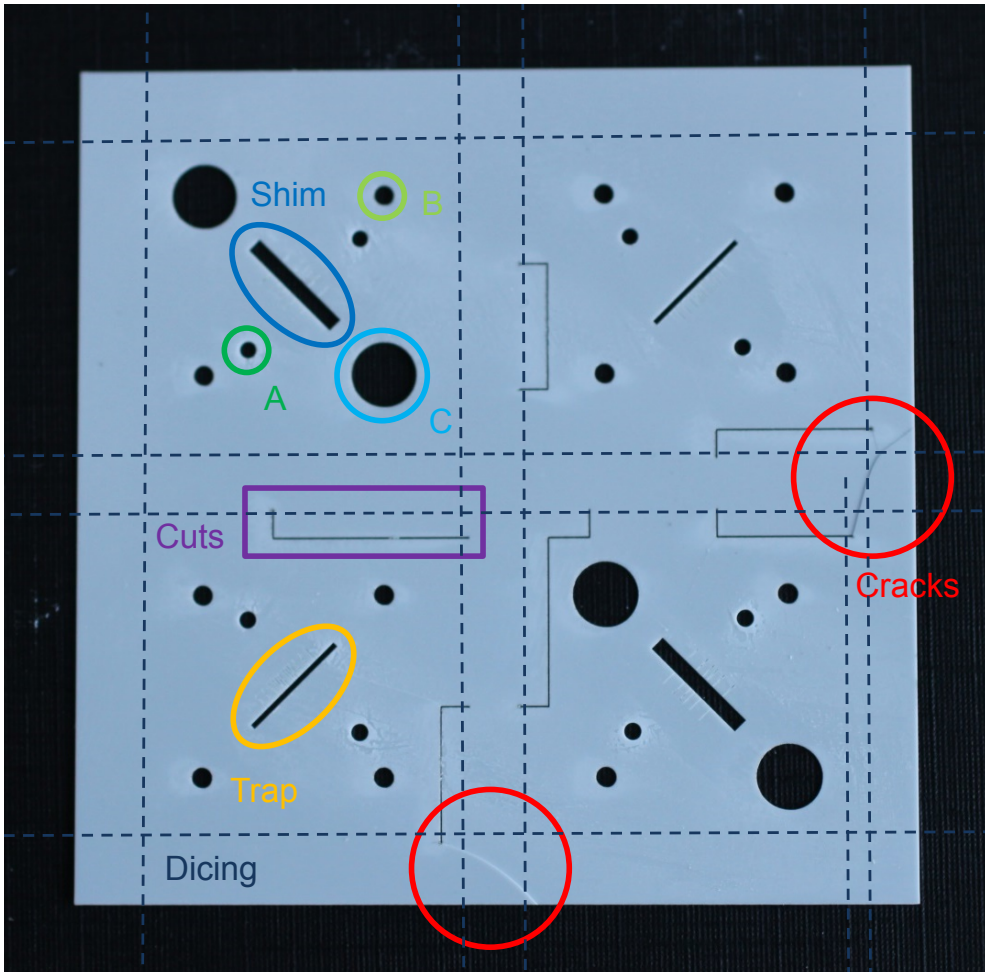

Figure 3.10: Full laser-machined wafer with patterns for the two shim (top left and bottom right) and the two trap wafers (top right and bottom left). The ellipse labeled 'shim' are the fine cuts for the shim electrodes of one wafer and the trapping channel. The ellipse labeled 'trap' marks the same for a trap wafer. Holes are marked with 'A' for an alignment hole, 'B' a screw hole for the full wafer stack, 'C' a clearance hole for the screws only fixing the trap wafers. The box labeled 'Cuts' marks a lasermachined cut used to define the final outer shape of a trap wafer after dicing (see text). The dashed dark blue lines labeled 'Dicing' mark the positions of the dicing cuts, separating the four trap-/shim-wafers. The 'Cracks' labeled circles are as mentioned in the text, from two incompatible laser-machining methods. For the final wafers only one laser-machining method was used. The full wafer is 2 by 2 inch.

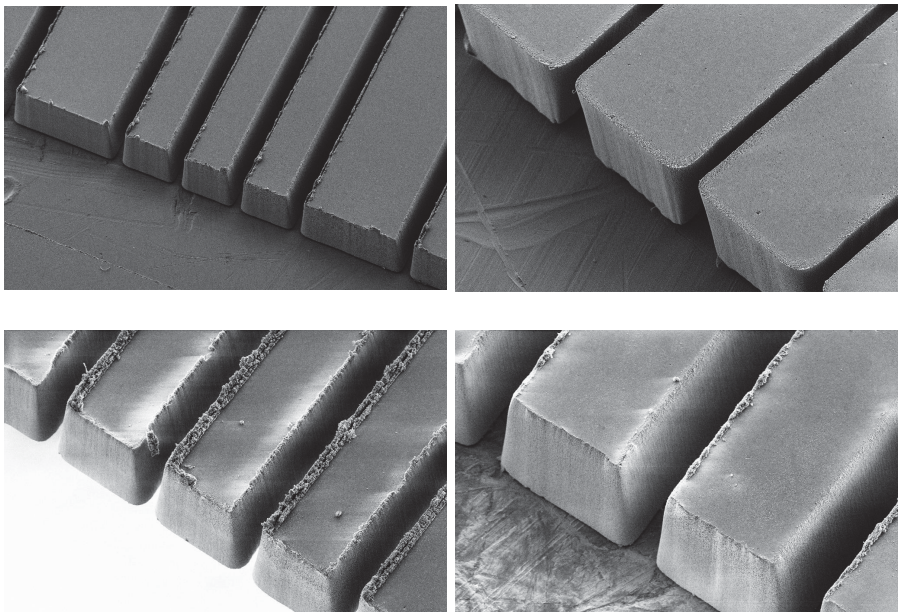

Figure 3.11: SEM pictures of laser machined trap structure from top (top left), bottom close-up (top right). A visible burr from laser machining (bottom left) was reduced by turning of the air sucker used to collect the fumes during the machining process (bottom right). In all pictures the (small) finger width is $\approx 155\,\mu m$.

in a PTFE frame leaving the front and back of the wafer exposed. Electrical contacting was done with one stainless steel wire both on the front and back of the wafer, pushing onto the wafer and a ledge of the frame below, preventing the wafer from breaking. To ensure a good connection the resistance from the outside contact to the wafer was measured before each evaporation to be $\approx 1\,\Omega$. Initial plating tests were performed with a solution from DOW[7]. As these proved not to produce the targeted surface roughness the solution was switched to METAKEM Gold SF, which was used successfully before by R. Blakestad [Bla10]. The plating process is very sensitive to the state of the plating solution. Care was taken not to contaminate the solution in any way. The solution was filtered before plating and its pH value was adjusted. The roughness of the plating was found to depend strongly on the pH value of the solution. The pH value changes with each use of the solution due to evaporation of ammonia and water during heating and plating and also through reduction of the sulfate-gold complex during plating. Both effects lower the pH value. Therefore the pH value was adjusted before every plating process, measuring the pH value and adding ammonia to reach the optimal level of 7.8 pH. When the pH value of the solution is very low gold grains start to precipitate

[7] AUROFAB^{TM} BP Plating Bath

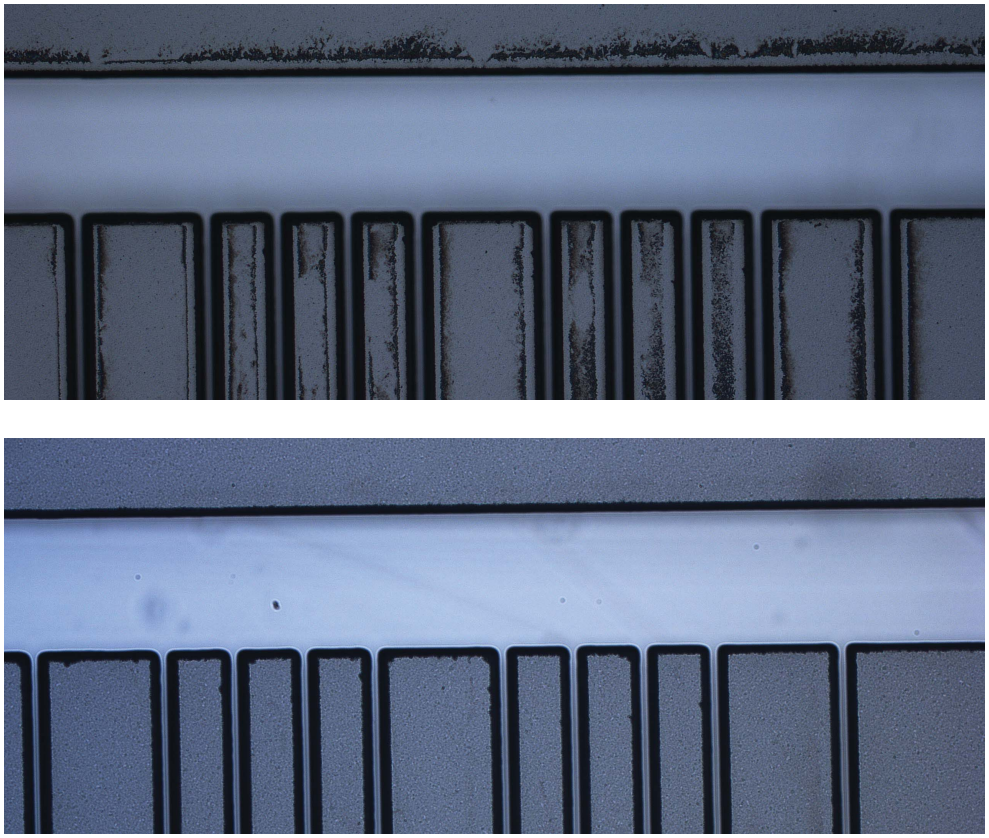

Figure 3.12: Laser-machined Alumina before (top) cleaning showing laser slag, cleaned with piranha etch (bottom).

and the solution needs to be filtered. Initially the solution was covered with aluminium foil during heating to prevent evaporation and changing of the pH value, but a blackening of the foil was observed, which is probably an effect of a redox reaction with the vapour of the solution. To prevent any adverse effect from this reaction a PVC cover was used during heating eventually. Also a final adjustment of the pH value immediately before plating was carried out. During plating the lower side of some dc electrodes did not build up gold or only a thin layer. This is most likely a problem of the evaporated gold not making a connection around the sharp wafer edges. Longer plating durations helped to start plating on all electrodes and faces, probably by gold growing over the edges and connecting the previously isolated patches. This led to a gold thickness varying between 6 µm to 10 µm on different surfaces of the trap.

Carrier/Filter Board The filter board has several purposes. It serves as mechanical carrier for the trap wafer and also bridges the electrical connections

to the vacuum feedthroughs. It also has RC low pass filters on every dc line to provide a ground for the trap drive rf and as a first stage of filtering noise to the dc electrodes. The substrate of the board is alumina, 0.635 mm thick, 101.6 mm squared. The gold tracks are printed with a thick film silk screen technique[8]. The resistors were also printed with resistance values of 240(40) Ω. The capacitors[9] have a value of 820 pF and where soldered on after fabrication with UHV solder[10]. This results in a corner frequency of 809 kHz for the RC filter and in a resistance to ground of 2 Ω for the dc trap and shim electrodes. With the calculated capacitances for dc trap electrodes between 1 fF and 20 fF (see section 3.2.1) and an applied rf voltage and frequency of 700 $V_{p\text{-}p}$ and $\Omega_{rf} = 2\pi \times 90$ MHz, this would result in 0.5 $mV_{p\text{-}p}$ and 10 $mV_{p\text{-}p}$ residual voltage on the dc electrodes respectively. These voltages do not create a significant residual micromotion. Also the wires connecting the filter board to the vacuum feedthrough with PEEK connectors were soldered to the pads on the filter board. As a last step the filter board was cleaned in a ultrasonic bath with acetone, isopropanol and DI pure water. On the lines to four outer shim electrodes (A1, D1, B7, C7) the filters were bypassed by bridging their resistors with wire bonds. As these electrodes are further from any trap zone where low noise is critical, these electrodes were thought as a crude possibility to drive magnetic dipole transitions of the ions at rf/microwave frequencies. Attempts in previous experiments at NIST to drive these transitions through filters failed. Bypassing the filter increases the rf amplitude on the electrodes and therefore at the ion. The bare filter board is shown in figure 3.13.

Assembly In a first step only the alignment-critical trap wafers with the main dc electrodes were aligned. This was done by fixing the trap wafers together with the center and the two middle spacer with screws through holes 'A' (see figure 3.14 onto a temporary mount machined from aluminum. With needles on translation stages and a microscope the trap wafers where aligned with respect to each other and finally fixed with screws through holes 'B'. By removing screws 'A' this assembled central trap wafer stack could be taken from the temporary mount. In a second step all other layers were combined, aligned with help of the alignment pins and fixed with screws through holes 'A'. Afterwards the trap and shim wafers where electrically connected to the filter board with wirebonds. For each dc electrode a minimum of five wirebonds was made. For the two trap rf electrode connections several tens of wirebonds where done.

[8] The gold tracks and resistive paste was printed by INTRATEC GmbH, www.intratec.de

[9] Special capacitors with a paladium-silver termination, Novacap, SMD ceramic cap. Size 0603, 100V, 820 pF, +/-5%, COG

[10] LewVac Components Ltd., www.lewvac.co.uk

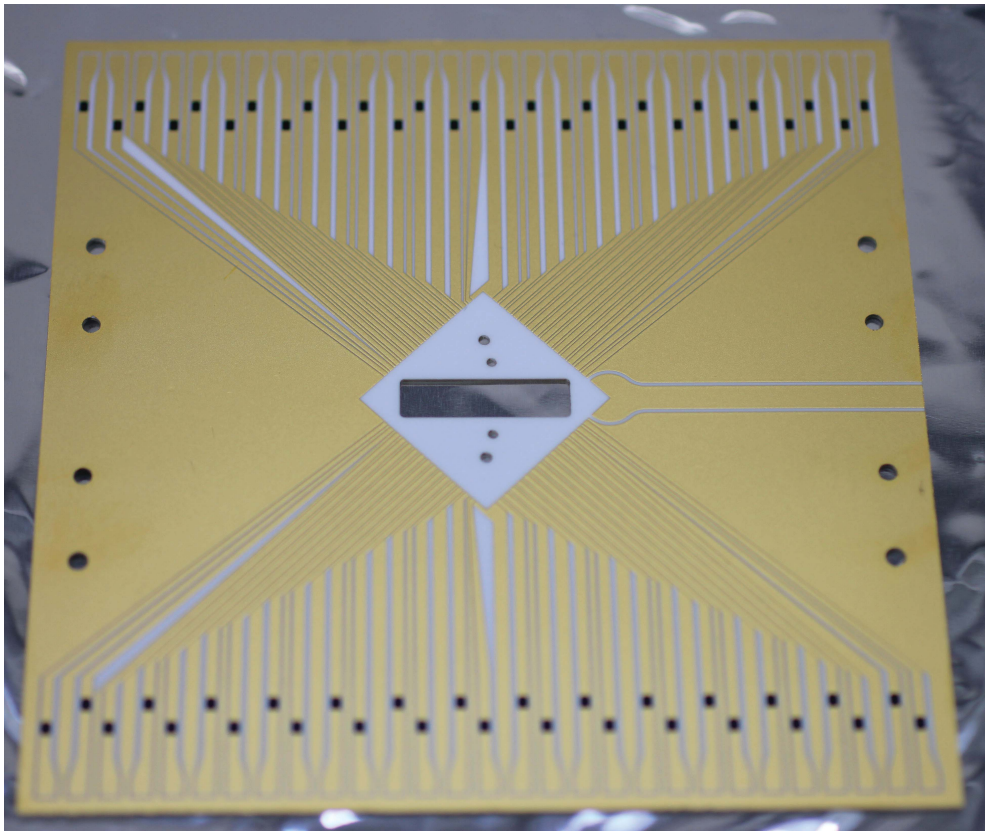

Figure 3.13: Picture of the filter board, without capacitors and wiring. The black rectangles on the tracks are the printed resistors. Lasermachined round holes on the side and in the center are for alignment and clearances for screws. The rectangular hole in the middle is the clearance for the trap channel.

3.3 UHV Chamber and Surroundings

The following describes the UHV vacuum chamber, the inside and surroundings. An overview drawing is shown in figures 3.15 and 3.16.

3.3.1 Trap mount and Atomic Source Ovens

The trap mount consists of a aluminium enclosure for the filterboard. This provides a precise mounting relative to the vacuum chamber and the atomic source ovens as well as electrical shielding against pickup and a possibility for a thermal connection of a cold finger to cool the trap. The figure 3.17 shows a picture of the trap mount during assembly.

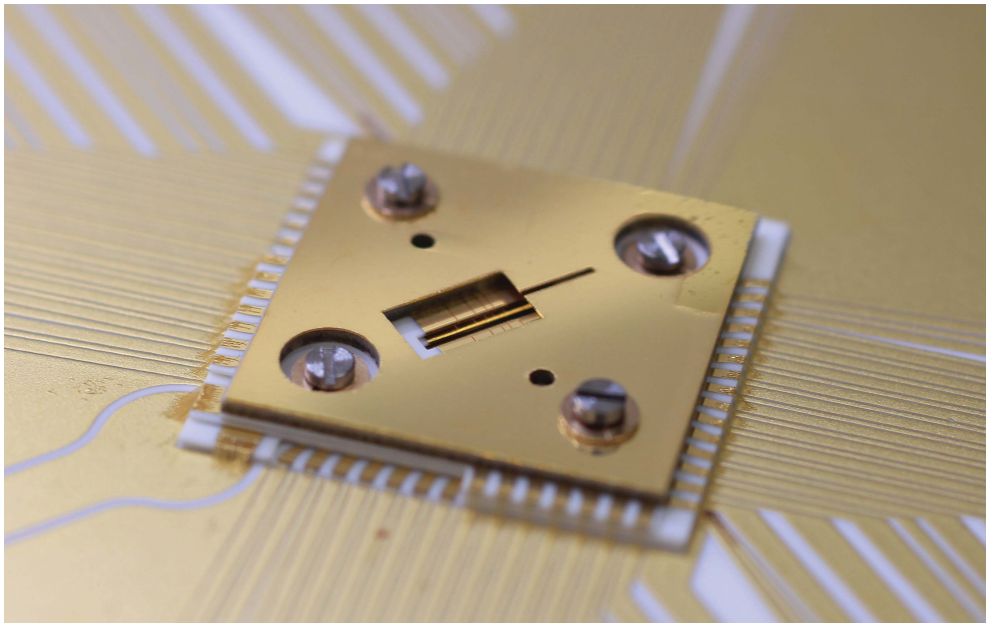

Figure 3.14: The picture shows the assembled trap stack on the filterboard. In the center the trap channel is visible, on top of the stack the mask wafer, on the edges of the stack the wirebonds to the filterboard.

Atomic Source Ovens

To provide the species loaded into the trap atomic source ovens were build, which heat calcium or beryllium by passing a current through a carrier material and evaporating a small amount. See [Hab12] for more on construction and tests of calcium and beryllium ovens. The oven assemblies are mounted on the outside of the trap mount. Two identical setups providing positioning and collimation of each a beryllium and a calcium oven. The ovens are mounted on a vacuum compatible PCB[11] with screws. The PCB then provides the electrical connections to the oven feedthrough to drive current through the ovens to heat them up. The ovens are shielded by a MACOR piece and an aluminium plate to prevent coating of other parts of the trap, potentially causing shorts on dc connections. The collimation piece, made from aluminium has two collimation slits and final aperture bores (2 mm diameter in the bottom of the piece to collimate the beam and direct it to a loading zone of the trap). Final collimation is provided by the mask wafer on top of the trap wafer stack (see section 3.2.2). Due to too tight tolerances for the collimation the final atomic beam is only 200 µm in diameter and not traveling through the trap in the center of the loading region but 80 µm displaced to the end of the trap. This made initial loading difficult as the atomic beam path had to be mapped

[11] Rogers Corporation, 4350B Laminate, www.rogerscorp.com

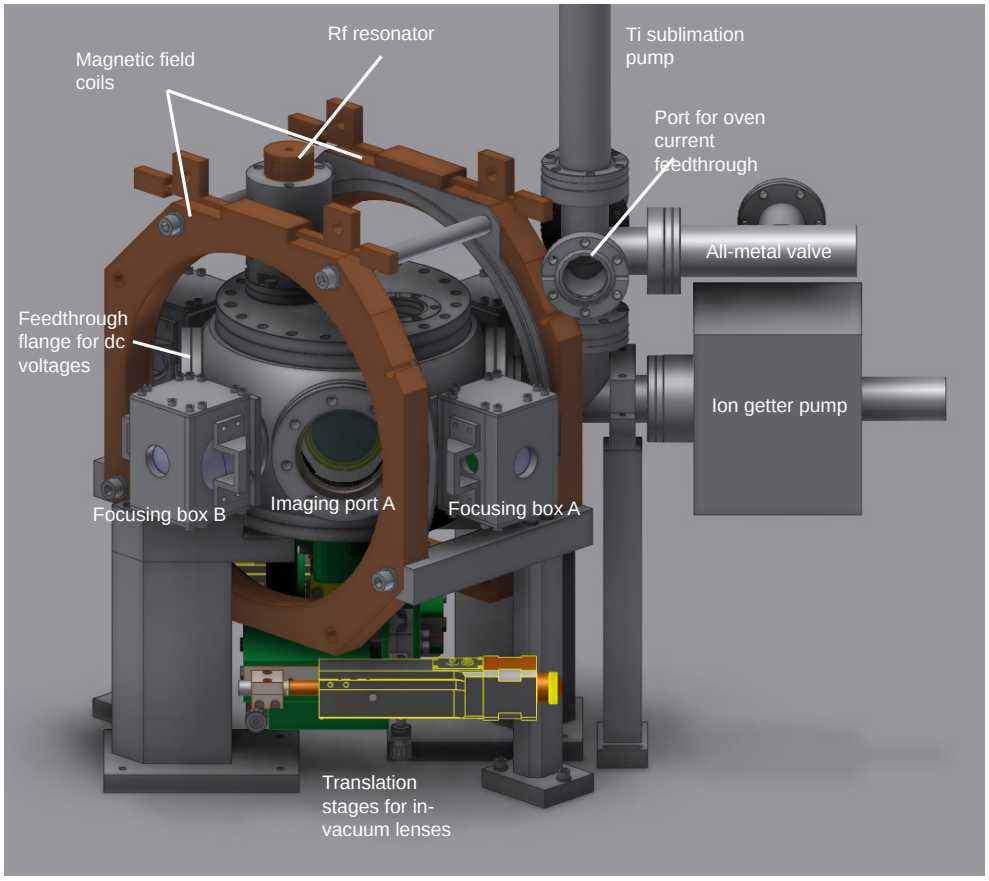

Figure 3.15: Overview of the main chamber.

out first, using the imaging system to observe the atom's neutral fluorescence signal from excitation with the 423 nm laser. On the other hand this has so far provided good shielding of the trap. No change in trap properties was noticed although all calcium from one oven was evaporated, which for other experiments lead to pollution of the trap, increasing the heating rates. So far the trap was only loaded from one side for both $^{9}Be^{+}$ and $^{40}Ca^{+}$. The second loading zone has a identical geometry and might have the same tight collimation and offset. Figure 3.18 shows drawings of the trap mount and the oven assemblies. See figure 3.19 for pictures of the oven mount and atomic source ovens.

3.3.2 UHV Chamber

Octagon As a main chamber a octagon[12], made from 316L stainless steel, was used, which features four CF40 and four CF63 ports alternated in the

[12]MCF800-SphSq-G2E4C4, Kimball Physics, www.kimballphysics.com

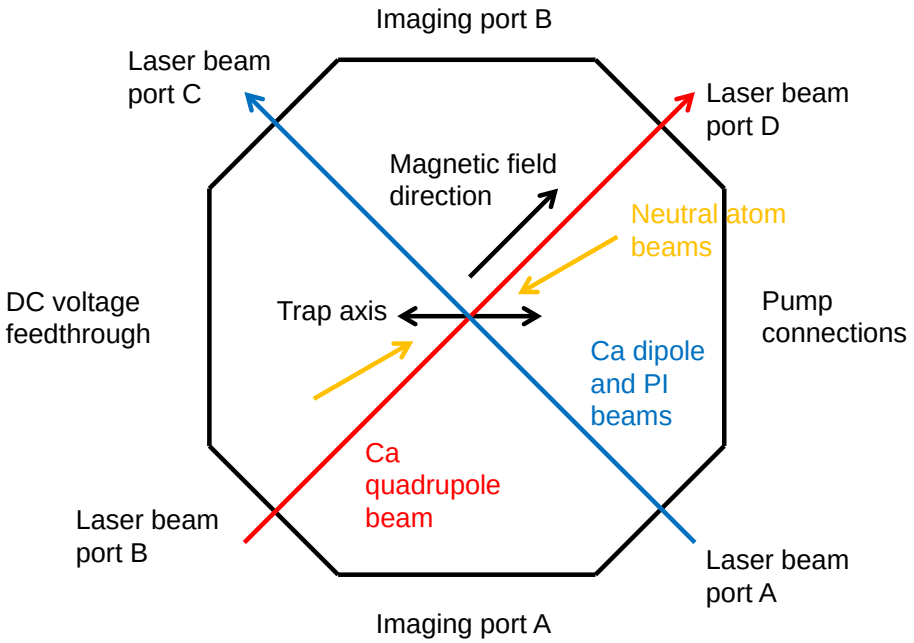

Figure 3.16: Schematic top view of the main chamber. Laser beams for beryllium were not drawn. They enter on all four ports and will be described in [Lo].

horizontal plane and CF150 ports on top and bottom. The CF40 ports are used for laser beam access, two CF63 port are used for imaging, one for the electrical feedthrough flange for the dc and shim connections to the trap, and the fourth for the connections to the pumps. The top port carries an adapter flange to two CF40 ports to connect the rf feedthrough and for a possible LN_2 cold finger[13] of the trap to achieve lower heating rates and better vacuum. This is not implemented in the current setup and the port was closed with a blind flange. On the bottom port an adapter flange to two CF16 ports is attached. This serves as a connection for the mechanical feedthroughs for the in-UHV lenses. The top and bottom adapter flanges where specially made by VACOM[14] from 316NL stainless steel.

Electrical Feedthroughs The chamber features three separate electrical feedthrough flanges. A dc and shim electrode connection flange with three high density D-sub connectors each containing 26 pins[15]. A rf feedthrough with

[13]Designed for the ST-400 Ultra High Vacuum (UHV) Cryostat from Janis Research (www.janis.com)

[14]VACOM Vakuum Komponenten & Messtechnik GmbH, www.vacom.de

[15]Allectra, 210-HD26-C63-3 3x High Density Sub-D F/T 26 pin on DN63CF, http://www.allectra.com

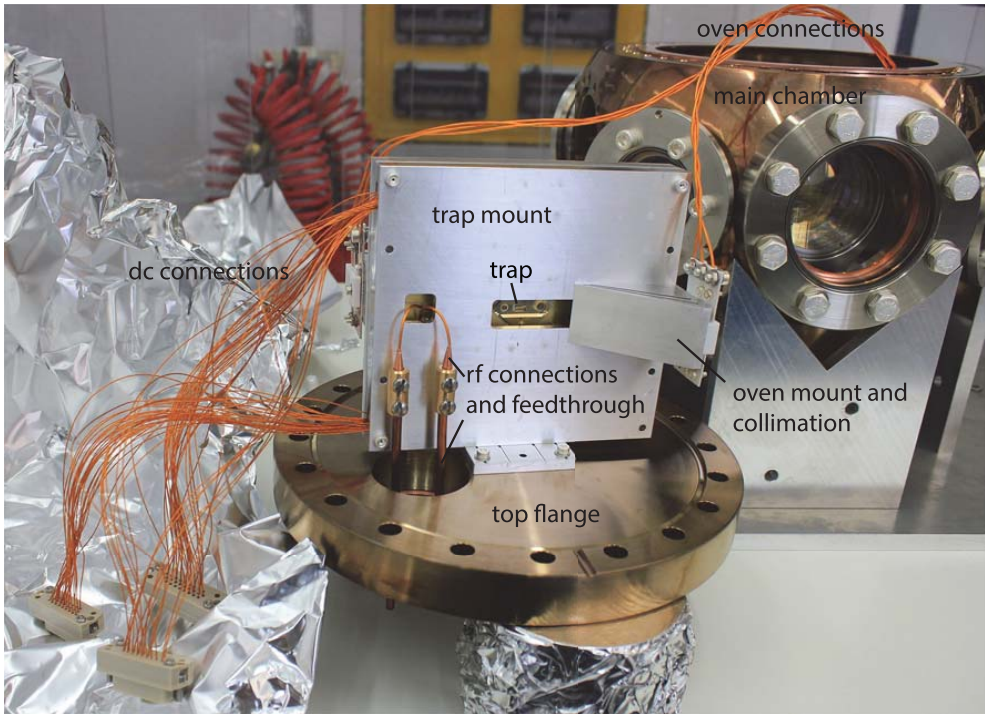

Figure 3.17: The trap mount on the top flange during final assembly. In the background a part of the main chamber can be seen.

two thick copper connections for the rf and rf ground[16]. A 6 pin mil connector feedthrough for the ovens which can carry up to 6 A per pin[17].

Viewports For optical access the chamber has six viewports. Four viewports for laser beam access are CF40 mounted fused silica[18]. Two imaging viewports with a larger diameter are necessary due to the large aperture lenses inside the UHV chamber. CF63 viewports[19] provide a sufficient clearance. The viewports installed have no anti-reflective coatings. All viewports are made from fused silica for minimal attenuation of the UV light for beryllium. These limit the maximum bakeout temperature of the chamber to 200 °C. In order to attach optics for focusing the laser beams onto the trap directly to the vacuum can mounting discs were made as an interface. They were sandwiched between the viewport and its mounting screws instead of washers. Each disk has three M4 threaded holes to which a focusing box (see section 3.4.2) was attached.

[16] Baruvac, CF40-HV10S-2-CE-CU39, www.baruvac.ch
[17] Allectra, 220-CM6-C40 Multipin f/t, 6 pins, for M16 plug on DN40CF, http://www.allectra.com
[18] MDC, VP-UV-C40, www.mdcvacuum.com
[19] MDC, VP-UV-C63, www.mdcvacuum.com

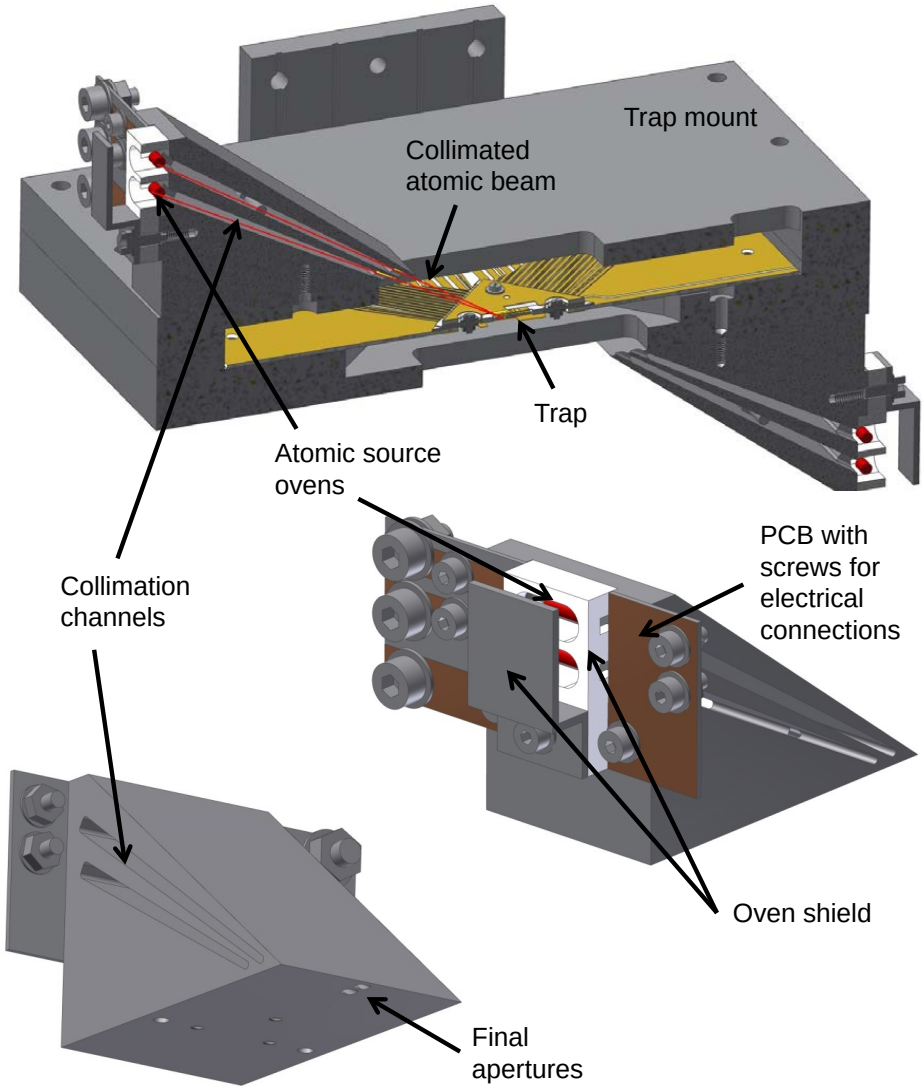

Figure 3.18: The drawing shows one cut view of the trap mount and two views of the oven assembly.

Figure 3.19: The left picture shows the mounting structure for the atomic source ovens. The ovens rest in a shield made from MACOR and are connected to a PCB which is connected to wires leading to the electrical feedthrough for the oven currents. In the top right picture a beryllium oven is shown, in the bottom right a calcium oven.

In-Vacuum Lenses and Mechanical Feedthroughs As part of the imaging system compound lenses were mounted inside the vacuum chamber. For these in-vacuum lenses to be movable from outside the vacuum chamber, a mechanical feedthrough was constructed from a steel rod mounting the lenses to the bottom of edge welded bellows[20], attached to the bottom flange of the chamber. The bellows have a CF16 flange on both ends. They are movable axial by ±1 mm and radial by ±2 mm. A restoring force to the center is given by: axial 41.9 N and radial 30.5 N at maximum displacement. The bellows were mounted outside of the vacuum system on translation stages[21] mounted to the bottom flange. The axis parallel to the trap axis is motorized with a stepper motor while the other axes are driven by manual micrometer screws. A cut through the mechanical design is shown in figure 3.20. See section 3.3.3 for a description of the imaging system and the optical properties of the in-vacuum lenses.

Pumps The UHV chamber is pumped by a standard combination of ion getter[22] and titanium sublimation[23] getter pumps. Additionally metal strips with a chemical getter material[24] were placed inside the main chamber in order to improve the local vacuum. The getter strips are activated by heat. The official activation needs 450 °C for 45 min, though according to SAES the getter strips get activated to 50% with a bakeout of 200 °C for 1 week.

Assembly All parts of the chamber and those inside (including all screws, washers etc. except the trap) were cleaned in acetone, isopropanol and ultra pure water (in this order) assisted by ultrasound for 5 min per bath. For initially dirty parts (e.g. machined by the department workshop) a prior ultrasonic cleaning with first an ammonia then a citric acid solution was performed[25].

Bakeout and Final Pressures Where possible the stainless steel parts of the chamber were first baked in air at 400 °C for approximately 12 h which reduces the amount hydrogen embedded in the stainless steel, improving final pressures. This step leads to a bronze colouring of the steel. In a second step the assembled chamber was baked without the trap to check for leaks and measure the final pressure.

In the following the full procedure is given with pressure levels and approximate times.

[20] COMVAT AG, www.comvat.com

[21] Thorlabs: manual axes: LNR25M/M, motorized axis: LNR50S/M

[22] VacIon Plus 20 StarCell, PN: 9191145 Agilent, www.chem.agilent.com

[23] Titanium Sublimation Pump Filament Cartridge Source, 2.75 in. ConFlat, PN: 9160050, Agilent, www.chem.agilent.com

[24] ST707/CTAM/30D STRIP, SAES, www.saesgetters.com

[25] Tikopur solutions RW 77 and TR 3

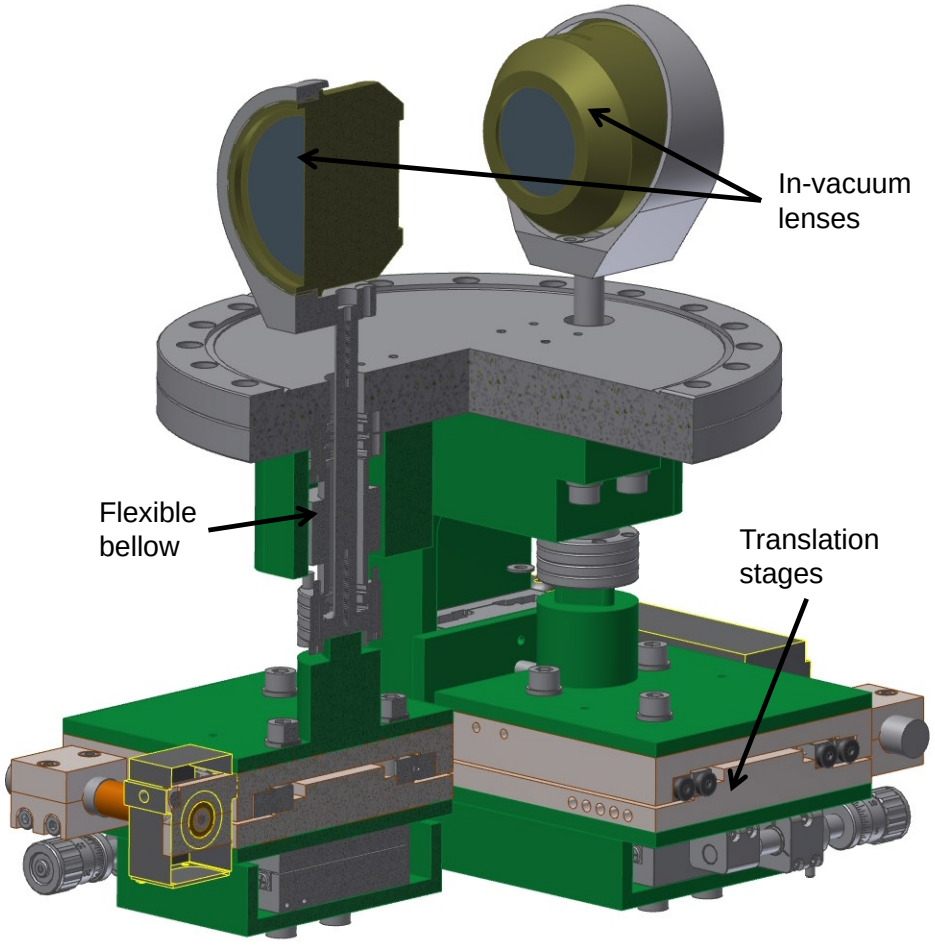

Figure 3.20: The drawing shows a cut view of the mechanical feedthroughs with translation stages attached outside of the vacuum chamber and the lenses for imaging inside. The ions/trap would be positioned in the center between the lenses. The translation stages and bellows are mounted on the bottom flange of the vacuum chamber.

1. Rough and turbo molecular pumping to $\sim 10^{-5}$ mbar (1 day).
2. First degassing of the titanium filaments wit a dc current of 32 A applied for 1 min, 3 times per filament.
3. Additional pumping with $40\,\mathrm{l\,s^{-1}}$ ion pump (1 h).
4. Ramping up the baking temperature to 190 °C, maximum rate ~ 1 K per 4 min (2 days).
5. Baking for 3 days.
6. Second degassing of titanium filaments, same procedure as above.
7. Baking for 4 days.
8. Starting chamber ion pump and pumping (1 day).
9. Closing off the outside valve to the pumping station and continuing pumping with only the chamber ion pump (7 days).
10. Ramping down the baking temperature, maximum rate ~ 1 K per 4 min (2 days).
11. Firing the titanium sublimation pump. Every filament for ~ 1 min at 37 A. After a settling time of 1 to 12 hours this was repeated until a pressure of 10^{-12} mbar was reached.

Finally the chamber was baked fully assembled with the trap inside following the same protocol as before.

No estimate of the pressure from a loss rate of ions from the trap was made. Lifetimes of a day for single ions are common with the cooling lasers on. Single $^{40}Ca^{+}$ ions stayed trapped over night with no cooling lasers running.

3.3.3 Imaging System

The experimental setup has two identical systems for imaging the trapped ions. This is used to image them at different zones of the trap without translating an imaging system. Currently a loading zone and the center experimental zone of the trap are imaged. One imaging system consists of a main lens inside the UHV chamber, which is adjusted in position for focus and trapping zone by mechanical feedthroughs outside the UHV chamber (see 3.3.2). The lens was designed to have the same working distance for the fluorescence from $^{40}Ca^{+}$ and $^{9}Be^{+}$ (313 nm and 397 nm). To image both species (outside of the vacuum system) the light is split by a dichroic beam splitter and compensation optics different for both wavelengths are used to create an image, which is recorded either with a PMT[26] or an electron multiplying CCD camera[27]. For

[26] Hamamatsu, H10682-210, www.hamamatsu.com
[27] Andor, DU-897D-CS0-UVB, www.andor.com

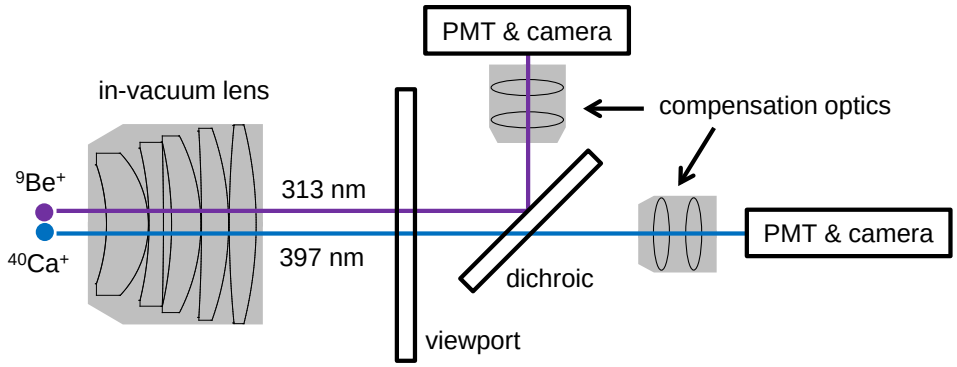

Figure 3.21: Schematic of a single imaging system, capable of imaging $^9Be^+$ and $^{40}Ca^+$ at the same time. The setup has two imaging systems of this kind.

imaging with the camera the ions are imaged directly on the CCD chip. For detection with the PMT the ions are imaged on the aperture of a pinhole with a PMT behind it. This allows spacial filtering, strongly reducing background light. Figure 3.21 shows a schematic drawing of the imaging system.
To estimate collection efficiency an experiment with $^{40}Ca^+$ was performed where with a first 397 nm pulse the ion gets shelved to the long-lived $D_{3/2}$ level and subsequently a single 397 nm photon gets released by a 866 nm pulse. As the PMT is not sensitive to the 866 nm photons only this single blue photon will be detected. Recording the number of photons collected and the number of experiments performed and the background counts from room lighting etc. the detection efficiency was calculated to be $\varepsilon = 0.006(2)$. The imaging system will be presented in more detail in [Lo].

3.3.4 Resonators

To reach the high rf voltage amplitudes required for the radial confinement of the ions a common approach is the amplification of a rf signal with a helical resonator. The design rules for these resonators are described in [MS59]. Following these it is possible to build a resonator with desired quality factor Q and resonance frequency ω_0 for the bare resonator. The main difficulty in the design of a resonator is to predict the change of the resonance frequency when the resonator is attached to the trap. The trap is ideally described as a capacitive load and the change in frequency can be described by using the telegraphers equations. For a transmission line of length l, with a characteristic impedance z_0 and a propagation constant γ, a load z_l, the input impedance z_{in} is calculated from

$$z_{in} = z_0 \frac{z_l + z_0 \tan(\gamma l)}{z_0 + z_l \tan(\gamma l)}. \tag{3.5}$$

Table 3.1: Design values for the two different resonators. D is the inside shield diameter and f_0 the resonance frequency of the unloaded resonator. These are the only 2 parameters needed to design a resonator as described in [MS59]. The capacitane and inductance are also derived from [MS59] for the given resonators.

	D (mm/in)	f_0 (MHz)	L(nH)	C(pF)
Low frequency resonator	60/2.4	145	464	5.6
High frequency resonator	33/1.3	350	145	3.1

For a perfectly coupled resonator on resonance $z_{\text{in}} = 0$ and with the resonator as transmission line assumed to be lossless $\gamma = i\beta$, where the wavenumber β is calculated as

$$\beta = \frac{2\pi}{\lambda} = \frac{2\pi f}{v}, \tag{3.6}$$

with the shifted resonance frequency f and the phase velocity v (given in equation 10 of [MS59]). The length of the transmission line is given by the effective length of the resonator b_{eff} (equation 11 in [MS59]). These assumptions result in

$$\frac{i\, z_{\text{l}}}{z_0} = \tan\left(\frac{2\pi f\, b_{\text{eff}}}{v}\right) \tag{3.7}$$

which is the result presented in [Roh09]. With this the shifted resonance frequency f for a purely capacitive load may be calculated. With a predicted capacitance of $\approx 5\,\text{pF}$ (2 pF for the trap from calculation and 3 pF estimated for the cabling) a first resonator was designed and constructed with a design value of 150 MHz for the resonance frequency to reach 90 MHz with the trap attached. Connecting this resonator to the trap a resonance frequency of 45 MHz was measured. The main reason for the mismatch was first assumed to be the underestimated capacitance of the vacuum feedthrough. A measurement of the feedthrough with the trap attached gave a capacitance of 27 pF. For this larger value a second resonator with a bare frequency of 350 MHz was constructed, which should according to calculation with a capacitive load of 27 pF result in a frequency of 80 MHz. Attaching this resonator to the trap a resonance of 62 MHz was measured, indicating that the full system is not well described by a purely capacitive load. This suspicion was hardened by a simple experiment where bulk capacitors with different values were attached to the two different resonators and the resonance frequency was measured, showing the behavior of the resonators for purely capacitive loads. The results are summarised in table 3.2 together with the previous measurements for the two resonators. The design values of the two resonators are given in table 3.1. Using numerical simulation[28] a new model of the trap, wiring and the resonator

[28] LTSpice, www.linear.com/designtools/software/

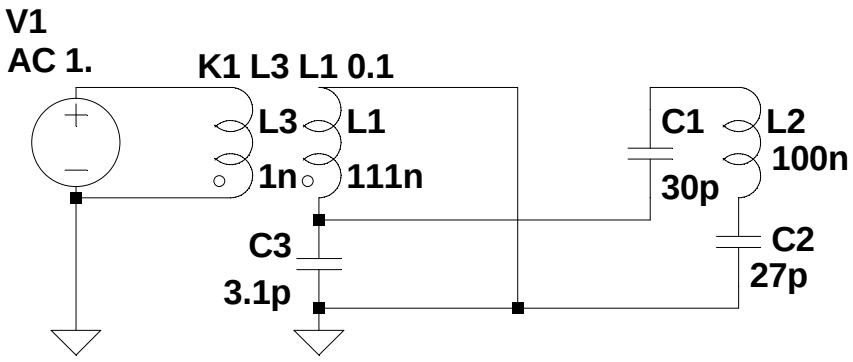

Figure 3.22: Equivalent circuit of the helical resonator and the attached trap used in simulations, where the trap was modeled as a capacitive and inductive load. C# labels capacitors, L# labels inductors. Their values given next to the labels in Farad or Henry respectively with the letter denoting the SI prefix nano (n) or pico (p). L1 (with a resistance of 0.1 Ω) and C3 form the resonator, with their values derived from [MS59]. C2 and L2 form the combined load of the resonator from the trap, the wiring and the feedthrough. C2 is measured. L2 is derived by matching the simulated frequency to the different resonator models. C1 is the capacitive divider (not used in all simulations).

could be established including a significant inductance. From the frequency measurements of the two resonators the value of this inductance could be deduced to be ≈ 100 nH. The simulated equivalent circuit is shown in figure 3.22. Further calculations showed that it is not possible to reach the desired 80 MHz to 100 MHz range with a helical resonator attached to this load. A solution was found by including additional capacitance between resonator and trap to decrease the total capacitance as seen from the resonator. This has the drawback of a reduced voltage amplitude. The added capacitance solved the issue and a final resonance frequency of 105 MHz was reached with the second resonator and an additional series capacitance of 30 pF, essentially halving the voltage delivered to the trap. As the capacitor breaks the dc ground connection a resistor with 1 MΩ was attached from the RF electrode connection to ground. Figure 3.23 shows a schematic of the final setup. The resonator is fed from an rf generator[29] which is amplified twice[30] to about 4 W and then coupled into the resonator inductively with a small loop of wire attached to a SMA connector in the cap of the resonator. The incoupling is optimised with a network analyser by minimising the reflected power. Incoupling with −40 dB

[29] Hewlett-Packard: 8640B signal generator

[30] First amplification: Mini circuits ZFL-1000VH2, 28 dB gain; second amplification: Mini circuits TIA-1000-4-2, 19 dB gain.

Table 3.2: Measured frequencies for the low and high frequency resonator (LFR, HFR respectively). Clearly visible is that for the low frequency resonator the inductance is not influencing the resonance frequency much as the values attained with bulk capacitors are similar. This is contrasted by the behavior of the high frequency resonator, where the frequency for the trap clearly deviates from values measured with the bulk capacitors. This is explained by the lower inductance of the high frequency resonator, resulting in a bigger influence of the trap inductance on the full system.

	$\omega/(2\pi)$ (MHz)
LFR, unloaded	140
LFR, loaded with trap	43
LFR, loaded with $C = 40\,\mathrm{pF}$	50.4
LFR, loaded with $C = 30\,\mathrm{pF}$	45.6
LFR, loaded with $C = 20\,\mathrm{pF}$	41.6
HFR, unloaded	334
HFR, loaded with trap	62
HFR, loaded with $C = 40\,\mathrm{pF}$	95.2
HFR, loaded with $C = 30\,\mathrm{pF}$	84.0
HFR, loaded with $C = 20\,\mathrm{pF}$	76.8

reflection is possible. The final resonator setup has a Q-value of $Q \approx 100$. With 26 dBm fed to the resonator the radial frequencies of the ion matched the simulation for $700\,\mathrm{V_{p\text{-}p}}$.

3.3.5 Magnetic Field Coils

To provide the 119.4 G offset field water cooled magnetic field coils were constructed[31] and set up in Helmholtz configuration. The coils have a diameter of 290 mm and a current supply[32] delivers 115.61 A to create the required field. The coils have 20 windings. Simulations of the field produced by the coils were performed taking the finite size of the conductor into account. Figure 3.24 shows the magnetic field along the trap axis (45° to the magnetic field direction) for various cases of alignment. For perfectly aligned coils the change of the magnetic field is described well in the region of interest by a parabola. The field changes from the center of the trap to the outer experimental regions (over a distance of 845 µm) by 0.19 mG. In a worst-case scenario of a misalignment of one coil from its optimal position by 10 mm in x, 5 mm in y and 10 mm in z direction the field changes by 3.9 mG over 845 µm. The change is well described by a linear function. Over a distance of 10 µm, which is in the

[31] Oswald Elektromotoren GmbH, www.oswald.de
[32] Agilent 6682A

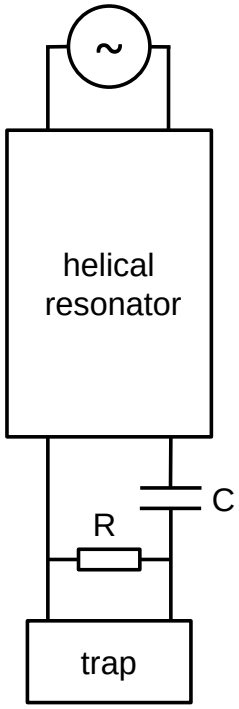

Figure 3.23: Schematic of the helical resonator. It is fed by a amplified rf source and its output is first connected to the capacitor C(30 pF) and resistor R(1 MΩ) and then with a vacuum feedthrough to the trap.

order of the ion-ion distance in a single trapping-well[33], the field changes by 0.025 µG in the optimal aligned case and by 63 µG for the worst-case scenario. Measurements of the magnetic field gradient were not performed yet.
In contrast, coils fitting better to the UHV-chamber with a radius of 7.5 cm and a distance of 30 cm would, in perfect alignment, produce a change of 0.17 µG over 10 µm (730 µG over 845 µm) and need 400 A of current (with 20 turns) to produce the required magnetic field.
The permanent magnet of the ion getter pump might also have an influence on the magnetic field gradient, which might require magnetic shielding to get to a low gradient.

[33] Two $^{40}Ca^{+}$ ions would be 10 µm apart for a trapping well with a motional frequency for a single ion of $\omega_m = 2\pi \times 2.5$ MHz.

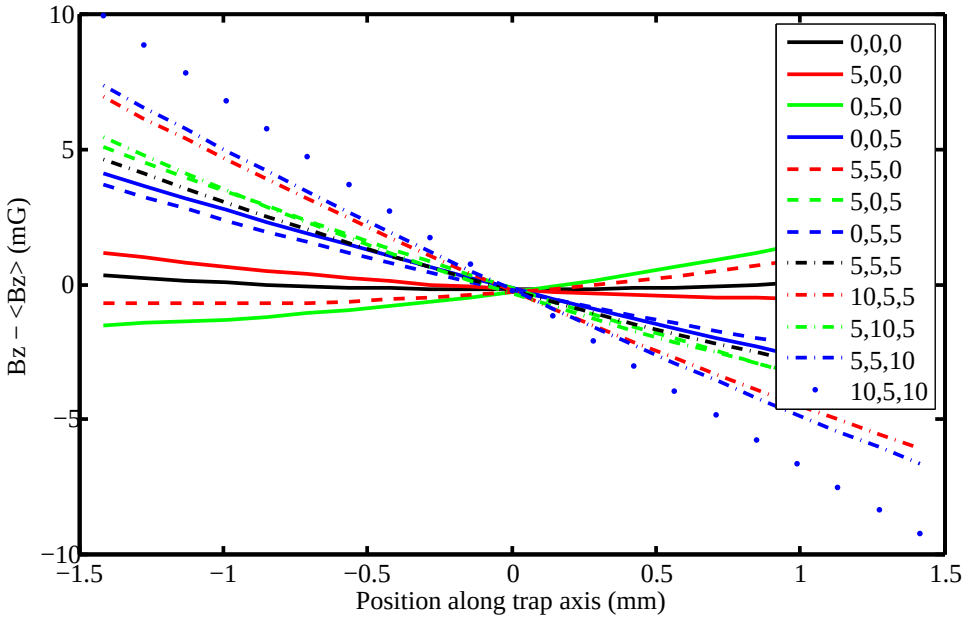

Figure 3.24: B field change along the trap axis for different displacements of one magnetic field coil from its optimal postilion. Displacement values given in the legend are in cm and ordered in x, y, z, with the optimal alignment labeled as '0,0,0' and the worst-case labeled '10,5,10'.

3.4 Laser Setup

3.4.1 Laser Light Sources

In the following the preparation of the needed laser light for $^{40}Ca^{+}$ and $^{9}Be^{+}$ is described.

397 nm Laser

The laser setup for addressing the $S_{1/2}$ to $P_{1/2}$ transition uses a commercial laser setup[34] starting with an Extended Cavity Diode Laser (ECDL) at 794 nm, amplified with a TA and doubled with a doubling cavity with a nonlinear BBO crystal to produce light at 397 nm. The main feature of the laser setup are two double passed Acousto-Optic Modulators (AOMs) diffracting in first positive and negative order, where the negative frequency beamline is sent to the ion π polarized, addressing the $S_{+1/2}$ to $P_{+1/2}$ transition. The positive frequency beamline sent to the ion sigma polarized, addressing the $S_{-1/2}$ to $P_{+1/2}$ transition. The electronic level scheme of the ion together with the lasers addressing the different transitions is shown in figure 3.26 for the 397 nm and

[34]Toptica photonics, 397 nm TA-SHG pro, www.toptica.com

866 nm laser beams used for detection and Doppler cooling. Both AOMs[35] have a wide tuning range (±20 MHz) without major change in diffraction efficiency. They are also used to switch the beam on and off. Both beams get coupled to the same polarization-maintaining fibre[36], but with perpendicular polarization, to deliver the light to the trap. A third AOM was recently set up by N. Oppong providing a second π beam set up counterpropagating to the other beams on the ion for future EIT cooling [SKEM$^+$01, LGT$^+$13] of $^{40}Ca^+$ ions. A schematic drawing of the beamline is shown in figure 3.25. Some light at 794 nm output on a monitoring port on the laser is used to stabilise the wavelength against slow drifts by referencing to a low finesse cavity (see [Lin11]) which is passively stabilized and, if left undisturbed, does not drift by more than 30 MHz in 24 h. The absolute wavelength is monitored with the wavemeter and optimized with the fluorescence signal of the ion.

Repumpers

For repumping the ion from the $D_{3/2}$ manifold while addressing the $S_{1/2}$ to $P_{1/2}$ transition with 397 nm we use light at 866 nm from an ECDL[37]. To address all Zeeman sub-levels in the $D_{3/2}$ manifold two frequency components are created with a continuously running AOM (0th and -1st order, 120 MHz). Both are superimposed and sent to a second AOM used for switching the beams on and off. For repumping the ion from the $D_{5/2}$ manifold to reset the qubit and for engineered dissipation of the pseudo-spin for the experiments described in chapter 5 a nearly identical setup as for the 866 nm is used. The only differences being the main wavelength (854 nm[38]) and the frequency of the splitting AOM (200 MHz). It was seen from experiment that the second frequency component from the splitting AOM did not significantly speed up the repumping and thus was not used in later experiments. Both lasers are stabilised against slow drifts by referencing to low finesse cavities (see [Lin11]) and their absolute wavelength is monitored with the wavemeter and optimized with the fluorescence signal of the ion for the 866 nm laser and with the $D_{5/2}$ repumping time for the 854 nm laser. A schematic drawing of the beamlines is shown in figure 3.27.

Photo-Ionization

For photo-ionisation of the neutral calcium atoms a two photon process is used as first demonstrated by [GRB$^+$01, LRH$^+$04]. For this a 846 nm ECDL[39] is doubled with a fibre coupled nonlinear waveguide[40] to 423 nm for the first excitation and a diode laser at 375 nm for excitation to a state close to the

[35] Intraaction ASD-802B8
[36] Schäfter+Kirchoff GmbH, PMC-400Si-2.3-NA012-3-APC
[37] Toptica photonics, 866 nm DL pro, www.toptica.com
[38] Toptica photonics, 854 nm DL pro, www.toptica.com
[39] Toptica 846 nm DL100
[40] ADVR PM FC/APC fiber in fiber out module including PPKTP SHG waveguide chip

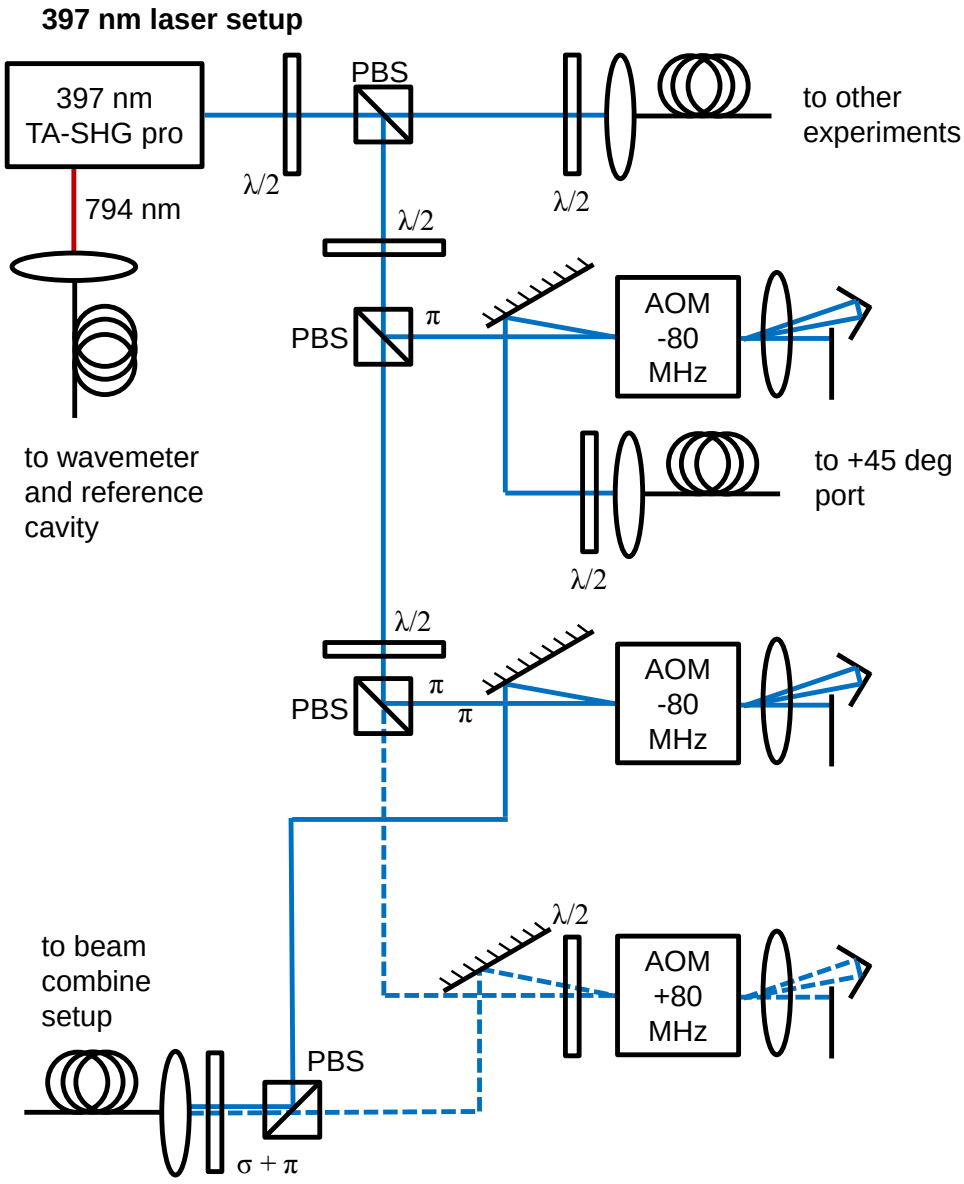

Figure 3.25: 397 nm beam line. The AOMs are used to produce the needed frequency shifts and to pulse the beam.

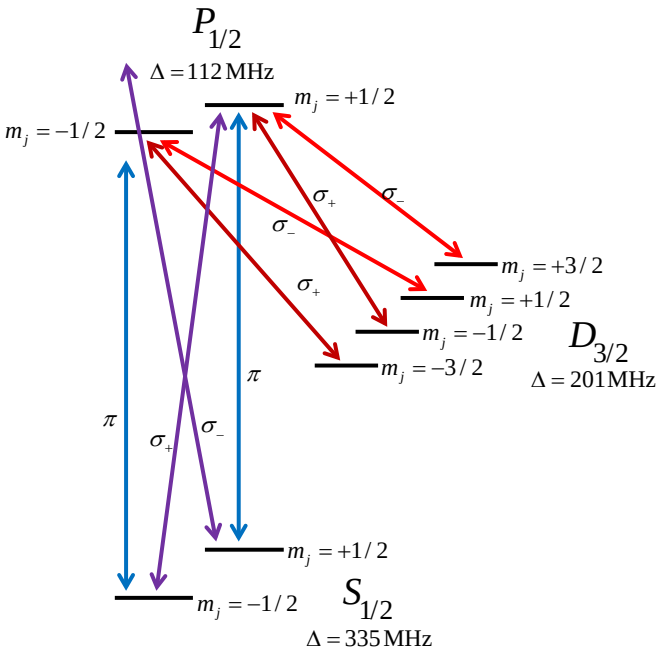

Figure 3.26: Level scheme and lasers used for Doppler cooling, detection and spin preparation of $^{40}Ca^+$. Different coloured arrows depict different frequencies. The two blue arrows are the 397 nm π-beam, the purple arrows are the 397 nm σ-beam. The bright red arrows are the higher frequency 866 nm beam and the darker red arrows are the lower frequency 866 nm beams.

ionization threshold. It was found that in this trap (possibly because of high rf drive frequency and voltage) it is possible to use the 397 nm laser for the second excitation step instead, but leading to a lower loading rate of $^{40}Ca^+$. The absolute wavelength of the 423 nm laser was found by observing fluorescence from the neutral calcium atoms. It is Doppler shifted blue by $\approx$ 200 MHz due to a $\approx 30°$ angle to the normal of the atomic beam. Its wavelength is monitored with the wavemeter. No further steps of stabilization are taken. A schematic drawing of the beamline is shown in figure 3.28.

729 nm Laser

To address the $S_{1/2}$ to $D_{5/2}$ quadrupole transition an ECDL with a wavelength of 729 nm is used. In general multiple transitions can be chosen for the pseudo-spin. The least magnetic field sensitive transition (0.56 MHz/G) is not accessible in this experimental setup because it needs the laser beam to hit the ion with a 45° angle to the magnetic field. As in this setup optical access is only possible with 0° or 90° to the magnetic field the second least

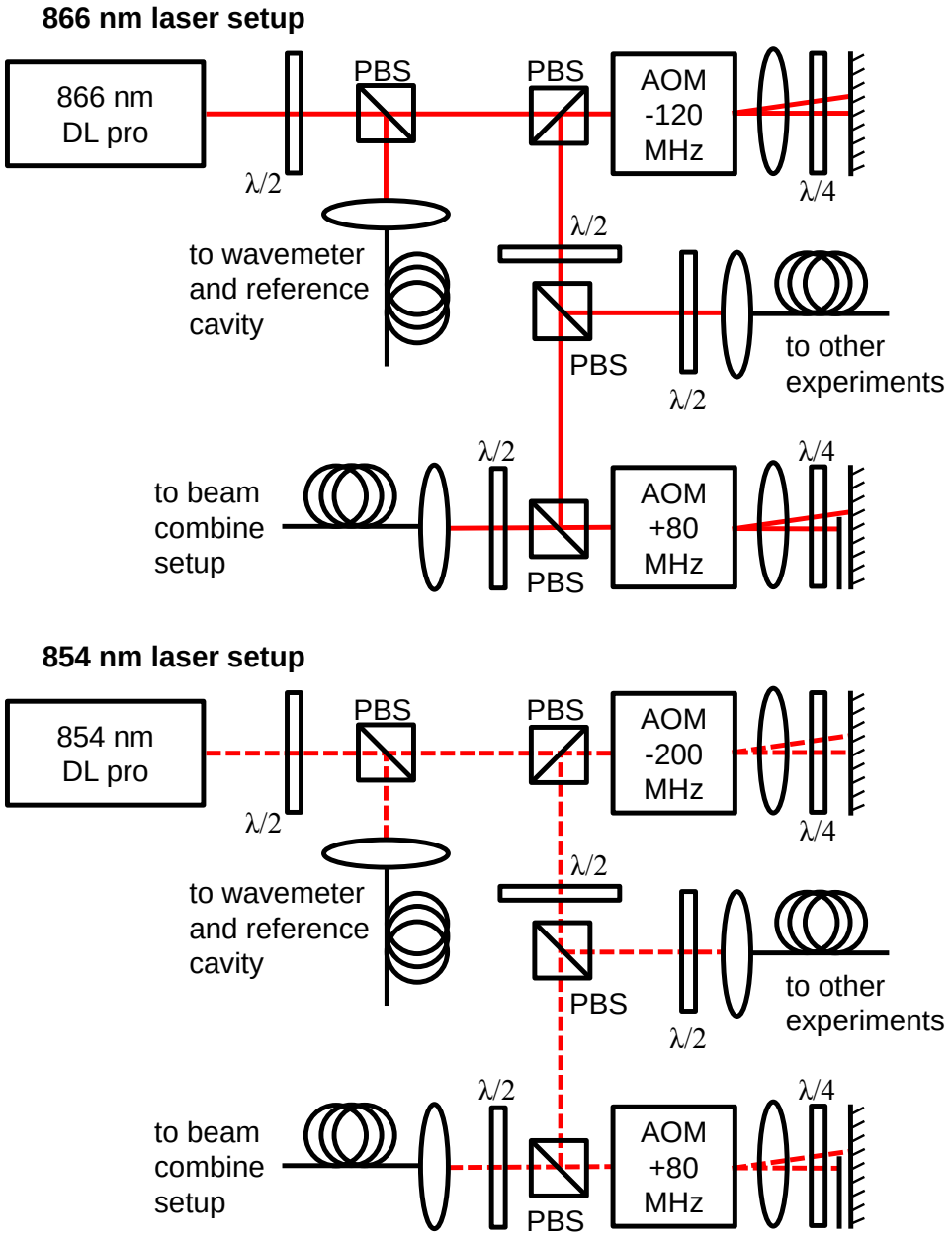

Figure 3.27: Beamlines for the 866 nm and 854 nm repumpers. The setup is similar with different values for the frequency splitting created by the AOMs. The splitting −200 MHz AOM in the 854 nm beamline was finally not used as repumping is working also without.

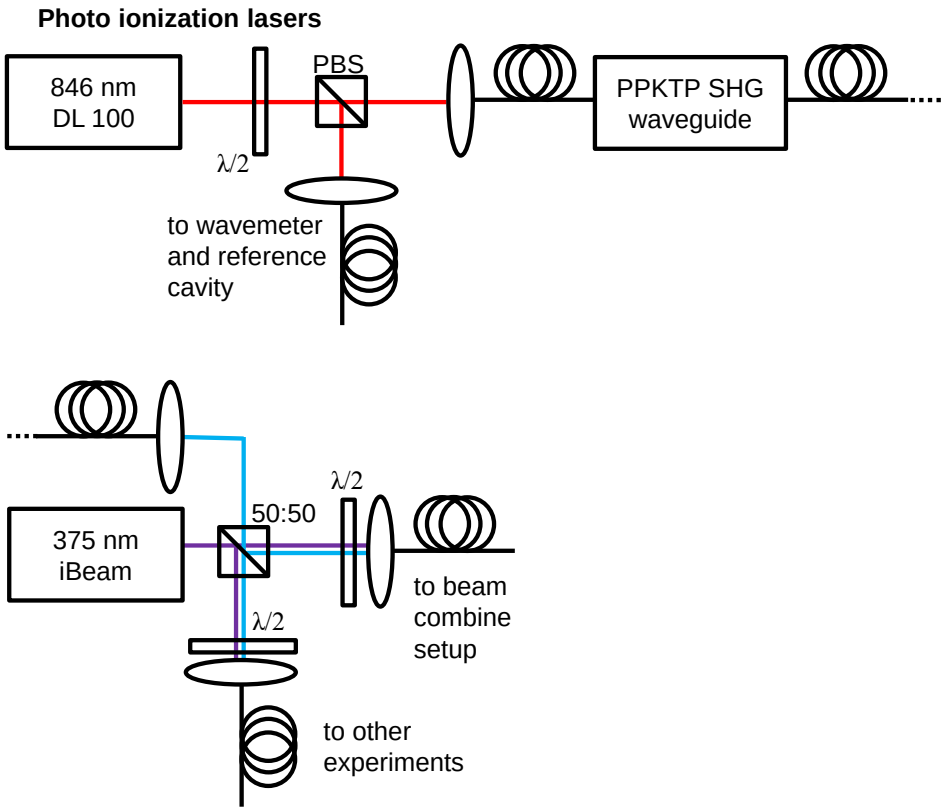

Figure 3.28: Beam line for the lasers used for photo-ionization beams for $^{40}Ca^{+}$.

magnetic field sensitive transition (1.12 MHz/G) $S_{+1/2}$[41] to $D_{+3/2}$ was chosen, addressed with a laser beam co-linear with the magnetic field. An in depth discussion of the 729 nm quadrupole transition of $^{40}Ca^{+}$ is given in [Roo00]. The level scheme for addressing of the quadrupole transition together with the 854 nm laser for repumping and the relaxation at 393 nm is shown in figure 3.29.

The 729 nm laser light is produced with a ECDL and amplified with a tapered amplifier[42]. A small amount from the diode output is used to narrow the line-width below 600 Hz using a Pound-Drever-Hall (PDH) lock to a high finesse cavity[43] [DHK+83]. It is frequency shifted 300 MHz by an AOM also used for fibre phase noise cancelation [MJYH94] and then coupled into a optical fibre and sent to a separate vibration and sound isolated box with the high finesse

[41] This nonstandard notation where S_{J,m_J} is simplified to S_{m_J} will be used throughout the thesis where no confusion with other J values is possible, still keeping the plus-sign for clarity.

[42] Toptica photonics: 729 nm TA pro, www.toptica.com

[43] Advanced Thin Films www.atf-ppc.com

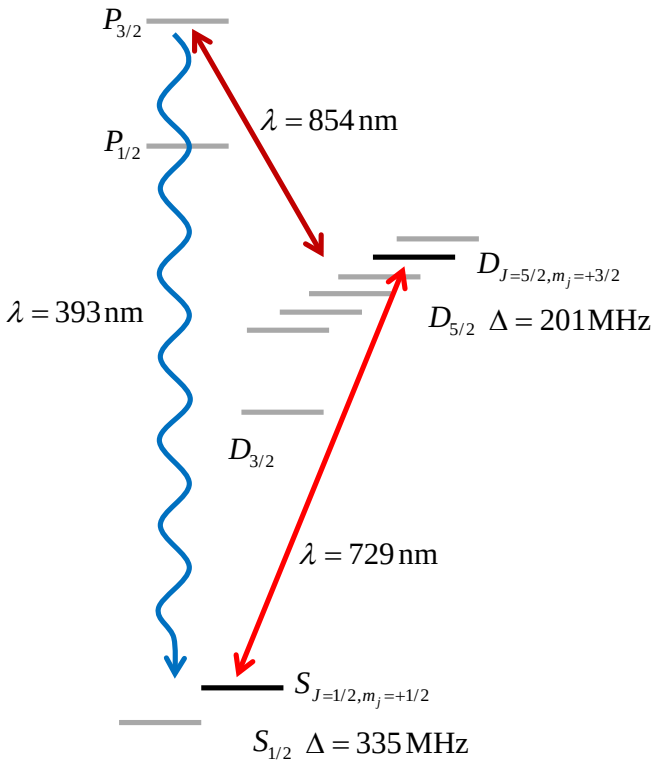

Figure 3.29: Level scheme and lasers used for coherent manipulation and repumping of $^{40}Ca^{+}$. The 729 nm laser addresses the sublevels $S_{J=1/2,m_J=+1/2}$ to $D_{J=5/2,m_j=+3/2}$ of the quadrupole transition, which are chosen as the qubit. The 854 nm laser repumps the spin with the emission of a 393 nm photon from the ion.

cavity setup. The lock and setup is further described in [Sep12], the fibre noise cancelation in [Mar13]. A main issue of the lock to the high finesse cavity is the limited servo bandwidth leading to amplified noise at up to 1.2 MHz from the carrier. This is an issue as this value is close to the ion's motional sidebands. With the center frequency of the laser resonant with a motional sideband this noise would address the carrier transition and lead to low fidelity of the pseudo-spin manipulations. For this reason all experiments were performed at trap frequencies for the axial mode of motion above 1.9 MHz. Techniques to improve the laser spectrum were investigated in [Flü14] and are planned to be implemented soon.
As the main portion of the light is used by other experiments a part of the TA output is frequency shifted −400 MHz by an AOM and then coupled into a fibre sending the light to a second TA[44] which amplifies the light to 600 mW.

[44]Toptica: 729 nm BoosTA

This output is coupled to a 30 cm fibre, kept short to minimize fibre phase noise. The fibre is mainly used to clean the spatial mode of the TA output and decouple pointing fluctuations from the AOM setup. After the fibre AOMs are used to produce frequencies to address the carrier transition and motional sidebands simultaneously and to pulse the laser beams.
In a first setup built by Karin Fisher [Fis13] three independent double-passed AOMs were used. To produce two frequency components addressing sidebands or the carrier two AOMs were used, the third planned for an off-resonant beam to cancel AC-Stark shifts as done in [Hem14]. This setup had several drawbacks. First the polarization of one beam is different than the other two, exhibiting different anti-correlated amplitude noise from polarization noise. Second the forming interferometer between the beams, inducing phase fluctuations which were measured to be up to 15° between to arms in 2 ms.
To tackle these shortcomings the setup was modified with a double passed AOM to pulse the beam and a second, single passed AOM driven with multiple frequencies to create the necessary multiple laser frequencies. Single passed AOMs typically experience duty cycle issues from thermal fluctuations leading to beam pointing fluctuations. To reduce this issue a frequency detuned from the ions resonance but still in the resonance range of the AOM is sent to the AOM whenever no pulse is on. This keeps the AOM at a more constant temperature than switching it on and off. As a second measure against duty cycle issues the center of the AOM was imaged with a lens onto the fibre tip of the fibre connecting the setup to the beam delivery for the trap, countering pointing fluctuations arising from duty cycle issues leading to fluctuating incoupling efficiency into the fibre and in turn to intensity fluctuations at the ion. The light from the AOMs is coupled into a short fibre (1 m), outcoupled close to the vacuum can and expanded in diameter before the final focusing lens in order to achieve a small focus diameter at the ion ($\approx 30\,\mu m$). Schematics for the full beamline are shown in figures 3.30 and 3.31.

Lasers for Beryllium

The laser setup for $^9Be^+$ will be covered in covered in the thesis of H.-Y. Lo. $^9Be^+$ has no repumpers and its pseudo-spin transition is driven with a set of Raman beams, which is why the only wavelength needed to manipulate and detect $^9Be^+$ is 313 nm. To photo-ionize neutral beryllium a two photon process at 235 nm is used. As both these wavelength are further in the UV than any of the $^{40}Ca^+$ wavelengths used, different optics are required and separate beamlines were set up. The beams were only combined directly in front of the vacuum chamber.

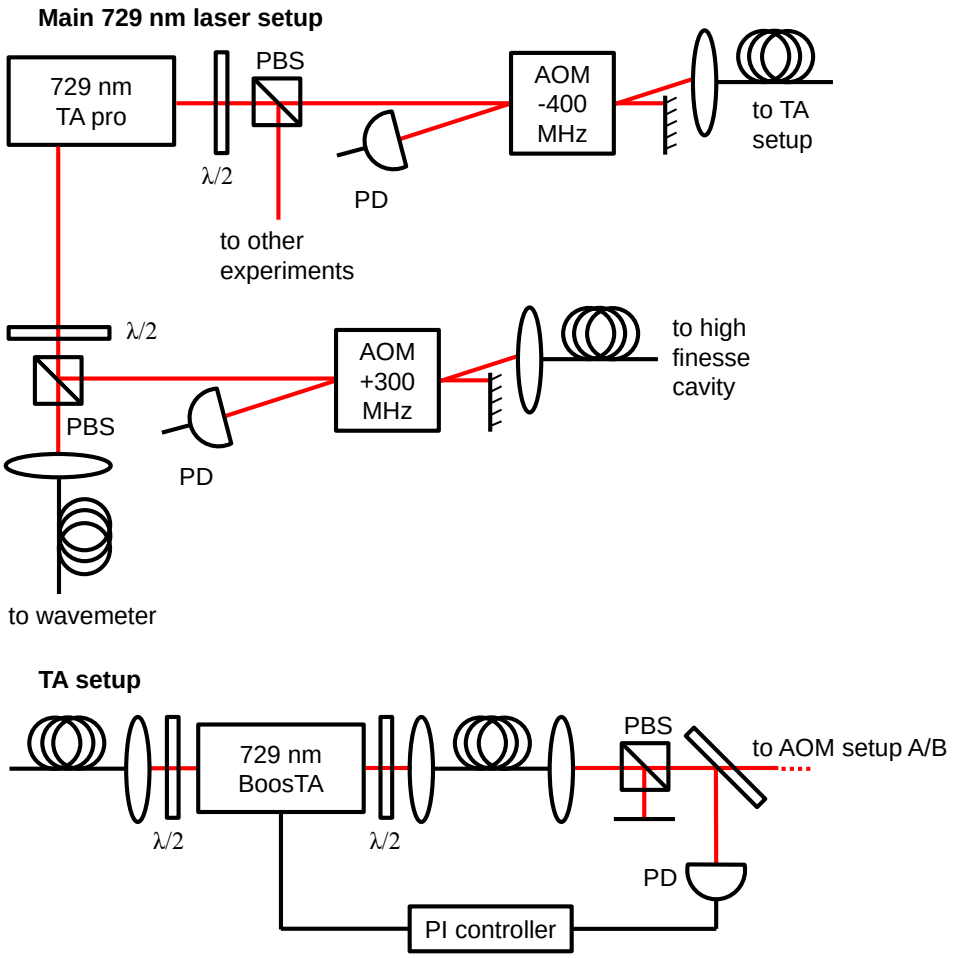

Figure 3.30: First part of the 729 nm laser beam line for locking the laser to the high finesse cavity, distributing and amplifying the light.

3.4.2 Beam Delivery

To combine the laser beams addressing $^{9}Be^{+}$ and $^{40}Ca^{+}$ a special optics mount was built. This 'focussing box' (shown in figure 3.33) is using the same dichroic beam splitter as the imaging system (see section 3.3.3), but now used as a beam combiner. It has two lenses, one achromatic lens[45] for the $^{40}Ca^{+}$ beams and a fused silica lens for the $^{9}Be^{+}$ beams. The box is mounted directly to the viewports of the vacuum can. All four viewports for laser beam access are equipped with such a box. The $^{40}Ca^{+}$ wavelength 854 nm, 866 nm, 397 nm, 423 nm and 375 nm get combined on 50:50 non-polarizing beam splitters and on dichroic beam combiners prior to the focussing box. Using the 50:50 beam

[45] Thorlabs AC254-200-A

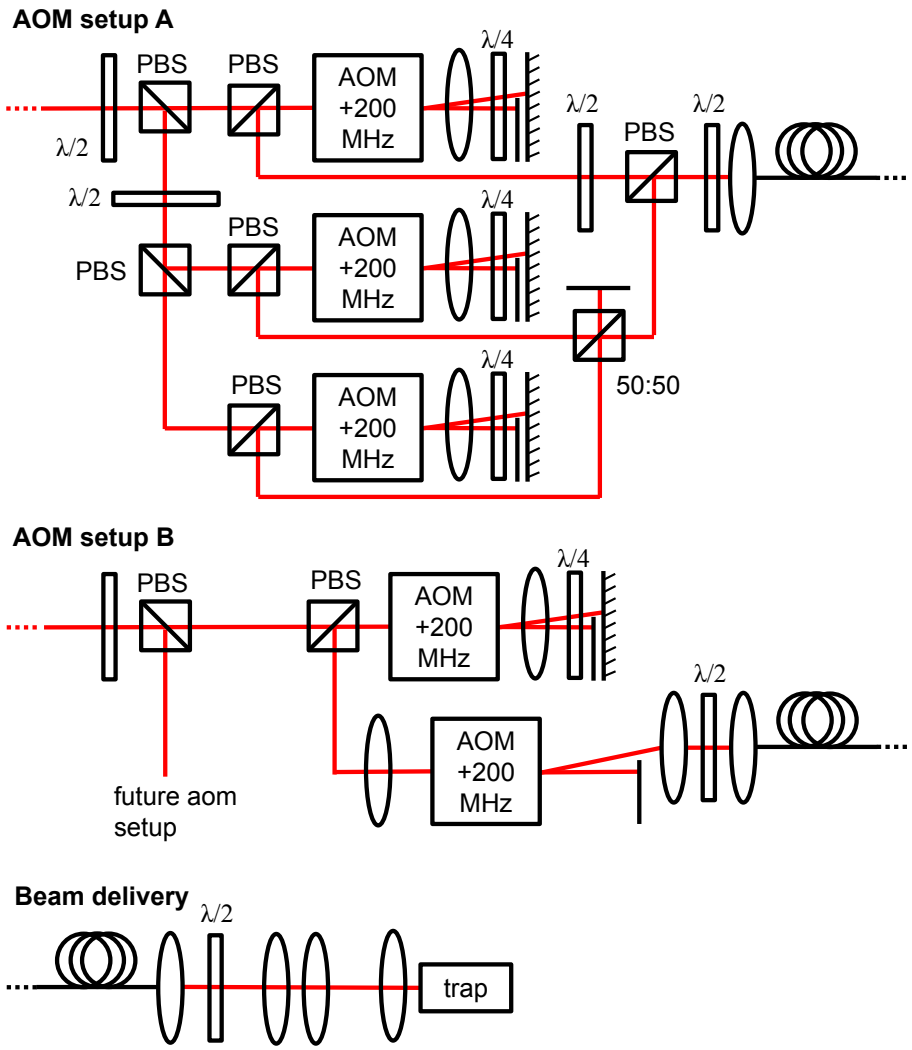

Figure 3.31: Second part of the 729 nm laser beam line, which creates the necessary frequencies to address carrier and motional sidebands and to pulse the beam. AOM setup 'A' and 'B' are alternatives used in different experiments. See text.

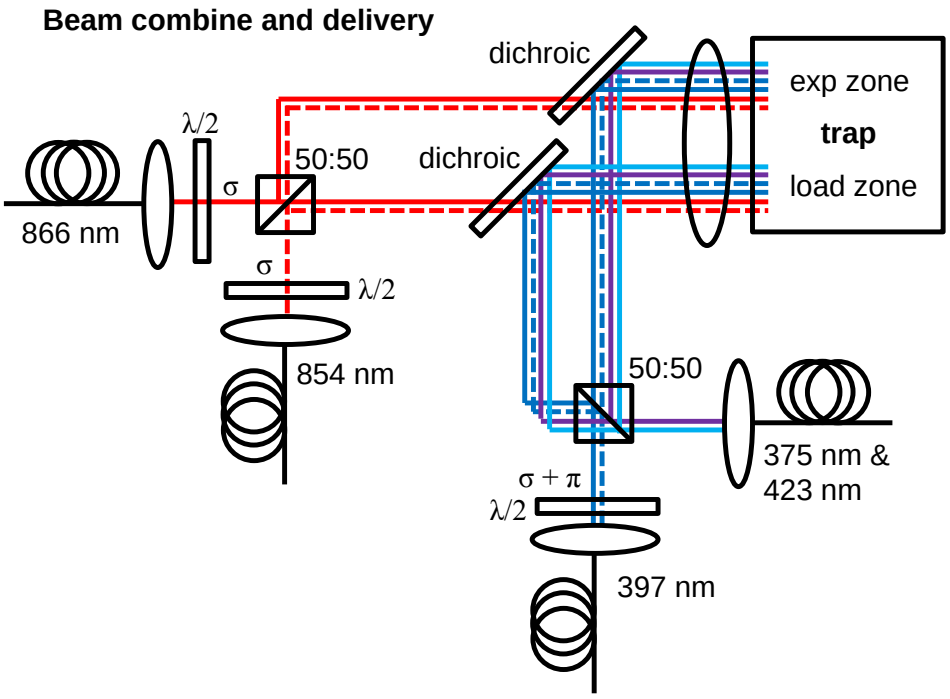

Figure 3.32: Overlap and delivery of the different laser beams needed to address the dipole transitions of $^{40}Ca^{+}$ and to photo-ionize the neutral calcium atoms.

splitters naturally gives two beams, one used for the experimental zone, one for the loading zone. The combined beams enter the vacuum can on laser beam port A (see figure 3.16) perpendicular to the magnetic field and make a 45° angle to the trap axis. The 729 nm beam enters the vacuum chamber through laser beam port B (see figure 3.16), co-linear with the magnetic field and also makes a 45° angle to the trap axis.

3.5 Computer Control

The computer control system consist of a ML507 evaluation board[46], which features a Virtex-5 chip (Virtex-5 XC5VFX70T). This consists of a field programming gate array (FPGA) and a Power PC 440. The FPGA allows to produce a timing-critical pulse sequence, where the Power PC feeds the FPGA the single pulses into a FIFO (first-in-first-out) and pre-computes the sequence. A main advantage of this system is the ease of programming, as the common user may write a pulse sequence in C/C++, which is much easier to learn than any VHDL (Very High Speed Integrated Circuit Hardware Description

[46]Xilinx, www.xilinx.com

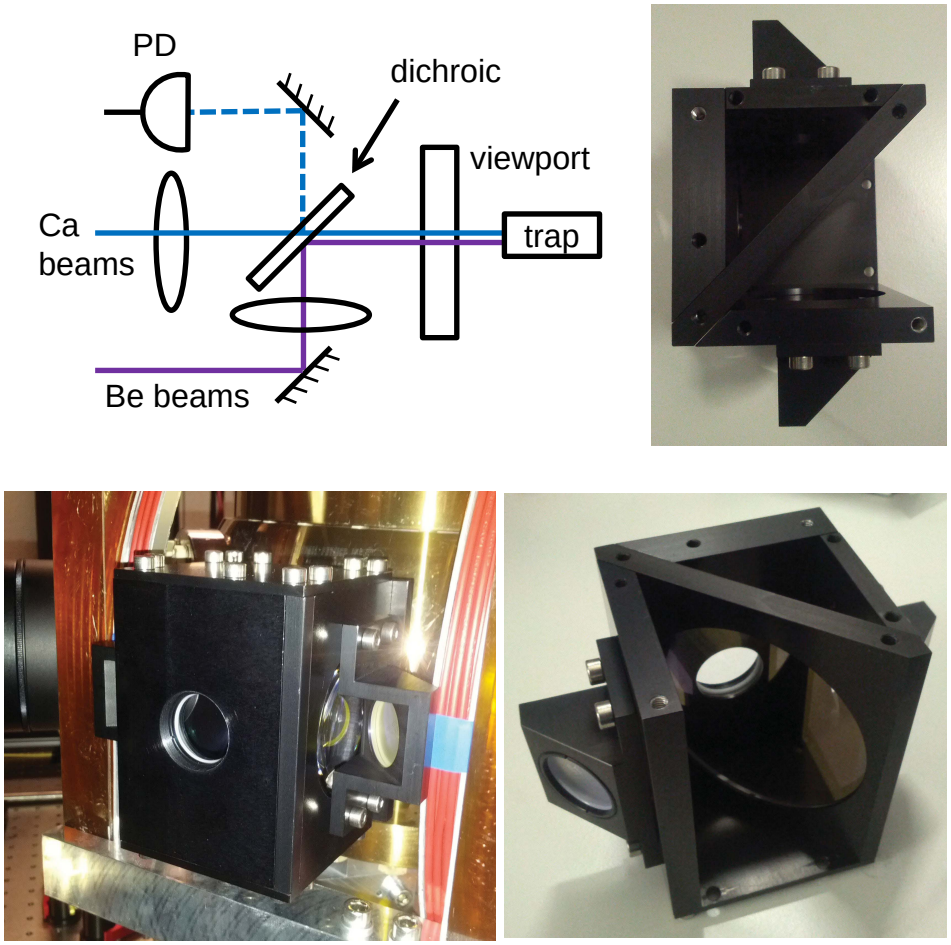

Figure 3.33: Focusing box: In the top left a schematic of the box is shown. The box has two entry ports, a central port for the $^{40}Ca^{+}$ beams and a side port for the $^{9}Be^{+}$ beams. It also has a port for monitoring powers using small reflections/transmission from the dichroic measured with a photo diode. The top right picture shows the box in the same orientation as the schematic. The bottom pictures show the box installed (left picture) and from the back (right picture).

Language) and less error prone than any C-to-VHDL compiler. The code running the ML507 board and the GUI code where inherited from the NIST ion storage group and further developed, mostly by B. Keitch and V. Negnevitsky. The ML507 board is controlled via ethernet through a graphical user interface (GUI) on a normal PC, where the user decides which pulse sequence to run with which parameter values. The ML507 board has 32 output lines (TTL, transistor–transistor logic), which can produce TTL pulses. These are used to define the laser pulses, mostly by controlling rf-switches, which route rf signals to the AOMs of the laser setup. As an interim solution newly designed direct digital synthesizer (DDS) boards[47] are preloaded with frequency, phase and amplitude settings via the PC. They allow a TTL signal to switch a channel to a second setting, which is phase-referenced to the first. These rf signals are routed to the AOMs allowing to change the frequency, phase and amplitude within an experimental sequence. In this interim DDS setup, the starting phase of the first pulse of any channel is random, with only the second pulse having a absolute phase reference to the first. No absolute phase reference exists between any two channels. This was a limiting factor for some experiments described in chapter 5. The system was now updated allowing for full phase control across all channels and several pulses on one channel within a sequence. This will facilitate more complex experiments in the future.

[47] Enterpoint, Milldown DDS1 ChannelCard, www.enterpoint.co.uk

Chapter 4

Experimental Techniques and Characterization Measurements

4.1 $^{40}Ca^{+}$ Dipole Transitions at 119 Gauss

Experiments with $^{40}Ca^{+}$ ions operate typically in low magnetic field, lifting the degeneracy of the Zeeman-states, but not increasing their splitting beyond their linewidth to ease Doppler cooling and fluorescence detection. The untypically high magnetic field chosen in this experimental setup necessitated simulations of the system and a more complex laser setup. As already discussed in section 3.4, the $S_{1/2}$ to $P_{1/2}$ transition must be addressed by a pair of 397 nm laser beams, one π-, the other σ-polarised. These beams mainly address the $S_{+1/2}$ to $P_{+1/2}$ and the $S_{-1/2}$ to $P_{+1/2}$ transitions with only off-resonant driving of the other transitions. The beams are co-propagating. Also the $D_{3/2}$ to $P_{1/2}$ transition needs several 866 nm laser beam components of different frequency and polarisation. With these two sets it is possible to drive the atomic levels to cool the ion by Doppler cooling and produce enough scattered photons at 397 nm to detect the ion. The simulation of this sub-system was performed by H.-Y. Lo, using full optical Bloch equations. Figure 4.1 shows a frequency scan of both 397 nm beams together for two typical power settings. Figure 4.2 shows a frequency scan of the 866 nm laser beam components. Clearly visible in both scans are the dark resonances formed between the 866 nm and 397 nm laser beam components. As the position of these dark resonances in frequency space depends on the detuning of both lasers, and since the 866 nm transition is highly saturated, we typically work with the 866 nm laser set far enough blue of resonance to also push the dark resonances away from the main resonance. The frequency difference between the two 397 nm components was also investigated. Figure 4.3 shows simulation and experimental data for a frequency scan of the sigma-polarised component. Here a dark resonance with the pi-polarised component can be seen as well as the dark resonances with the 866 nm laser. For an optimal working point the 397 nm sigma component has to be detuned

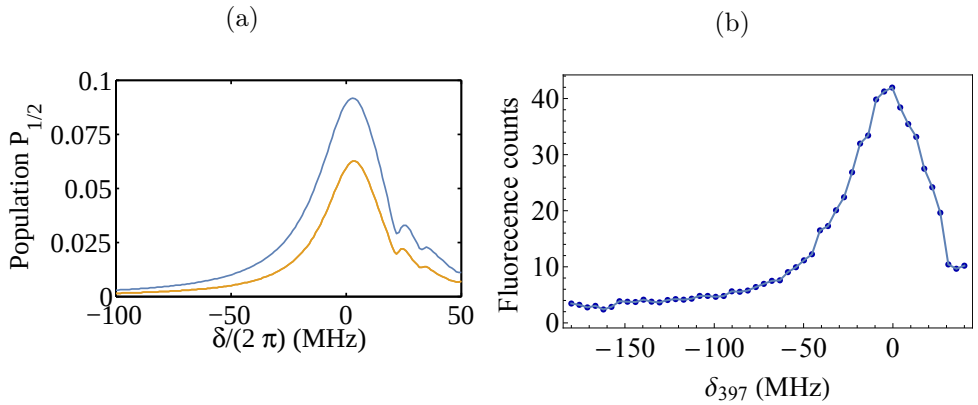

Figure 4.1: 397 nm fluorescence spectrum of $^{40}Ca^{+}$, scanning the detuning of the 397 nm laser frequency. (a) Results of the simulation. The blue trace shows the spectrum with the 397 nm powers used for detection, 7 µW for both 397 nm frequency component (0.9 saturation intensities). The yellow curve shows the scan with powers used for Doppler cooling, 3.5 µW for each 397 nm frequency component (0.46 saturation intensities). In both curves dark resonances with the 866 nm frequency components can be seen blue of the main resonance. Calculating the expected number of photons per unit time from the simulation with the detection efficiency as measured in section 3.3.3 gives $\dot{N} = P\,\Gamma\,\eta = 0.09{*}2\pi{\times}21.6\,\mu s^{-1}{*}0.006(2) \simeq 73(24)\,ms^{-1}$. (b) Experimental data of two ions with optical powers set for detection and a detection time of 200 µs, resulting in $\dot{N} \simeq 105\,ms^{-1}$ for one ion on resonance. This deviation might be explained by different optical powers (simulations show a maximum population of the $P_{1/2}$ level of 0.15) and the large error of the measurement of the detection efficiency. Also the signal is not background-free.

by ~ 11 MHz blue from the dark resonance.

4.2 Ion Loading

Loading ions is achieved by heating an atomic oven by passing an electrical current through it. This evaporates neutral atoms which are then photo-ionised in the trapping region with laser light of 375 nm and 423 nm wavelength for $^{40}Ca^{+}$ or 235 nm for $^{9}Be^{+}$. Loading one $^{40}Ca^{+}$ ion takes 1 min if the full setup is optimized using a current of 4.2 A (0.7 V). $^{9}Be^{+}$ has a similar loading time with 0.63 A (2 V). The time is mainly limited by an initial warm-up of the ovens, not by a steady-state loading rate. The electrical currents are chosen such that single ions can be loaded. At higher currents ions load too fast after the initial warm-up to reliably trap only one ion. Higher currents are possible and currents up to 6 A (for a short time) were used for detection of neutral atoms. During loading one imaging system was usually used to either detect

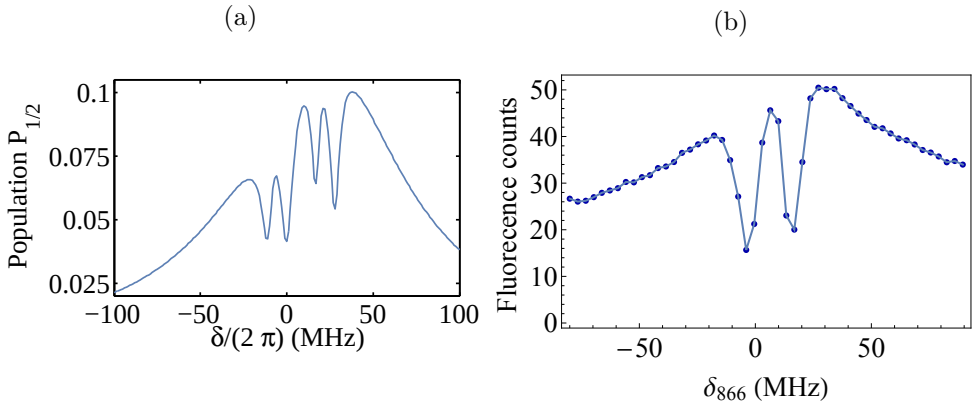

Figure 4.2: 397 nm fluorescence spectrum of $^{40}Ca^{+}$, scanning the detuning of the 866 nm laser frequency. (a) showing simulations with multiple dark resonances with the 397 nm frequency components visible. (b) Experimental data showing the same basic structure, but not resolving the fine details of the dark resonances. A typical working point for the 866 nm laser would be blue detuned at 50 MHz.

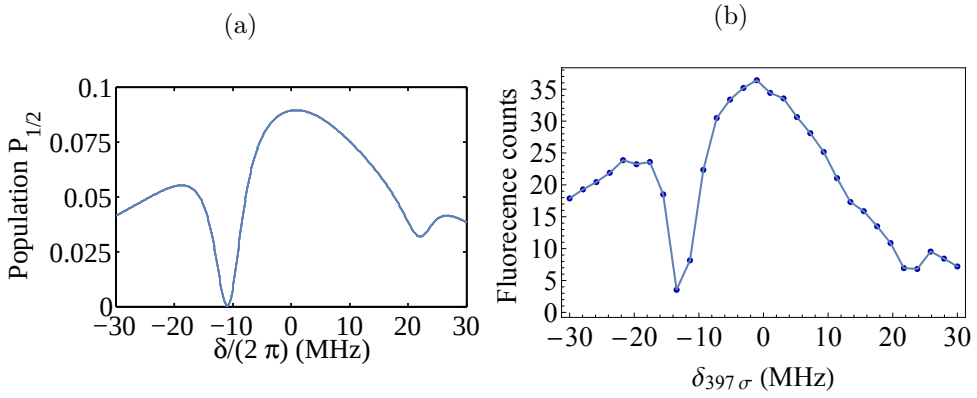

Figure 4.3: 397 nm fluorescence spectrum of $^{40}Ca^{+}$, scanning the detuning of the σ^{+} polarised frequency component of the 397 nm laser. A dark resonance with the π polarised component is visible at $\simeq -11$ MHz and another with the 866 nm laser at $\simeq 22$ MHz. (a) shows the result of the simulation, (b) experimental data.

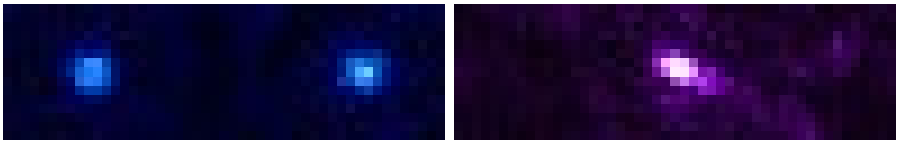

Figure 4.4: Pictures of two $^{40}Ca^{+}$ ions and one $^{9}Be^{+}$ ion trapped simultaneously in the same potential well. The left picture shows the fluorescence of the two $^{40}Ca^{+}$ ions with a dark $^{9}Be^{+}$ ion in the middle, the right picture shows the fluorescence of the single $^{9}Be^{+}$ ion surrounded by the two dark $^{40}Ca^{+}$ ions.

the ions fluorescence with the PMT or image it with the camera. After loading an adiabatic waveform is applied to the dc trap electrodes to shuttle the ion to the experimental zone were it was imaged with the second imaging system. It was also possible to load without detection/imaging in the loading zone.
Loading the trap for the first time it was essential to use the PMT with background-subtracted detection (see section 4.3.4) to detect the ions signal prior to optimization.
The trap proved to be able to trap $^{9}Be^{+}$ and $^{40}Ca^{+}$ ions simultaneously as shown in figure 4.4.

4.3 Experimental Sequence

All experiments use the same basic structure. First the ion is pre-cooled by the 397 nm π polarized beam, which is red detuned from the $\left|S_{1/2}, M_J = +1/2\right\rangle \leftrightarrow \left|P_{1/2}, M_J = +1/2\right\rangle$ transition by ≈ 40 MHz with ≈ 100 saturation intensities, and repumped by the 866 and 854 nm beams. This pulse helps to recrystallize the ion in case a background collision heated it up and also gives the FPGA time to fill the FIFO with the subsequent pulse sequence. This pulse usually lasts 3 ms. Next near resonant Doppler cooling (section 4.3.1) is performed for $\simeq 500\,\mu$s, followed by optical pumping of the ion into the $\left|S_{1/2}, M_J = +1/2\right\rangle$ state (section 4.3.2). The ion is cooled close to its motional ground state by sideband cooling (section 4.3.3). Finally the main experiment is performed followed by measuring the spin state using fluorescence detection (section 4.3.4).

4.3.1 Doppler Cooling

Doppler cooling [WD75, HS75] relies on the momentum transfer between an atom and photons it absorbs from the laser beam used for cooling. If this laser beam is red detuned from the resonance of the atom the probability of the atom absorbing a photon is highest when it is moving against the beam direction, as the Doppler shift then compensates the detuning. With the momentum of the photon $\hbar\mathbf{k}$ ($\mathbf{k}$ being the laser beams k-vector) and the atoms momentum $\mathbf{p}$ being anti-parallel, the momentum of the atom after absorbtion $\mathbf{p}'$ of the

photon will be lower than before

$$|\mathbf{p}| > |\mathbf{p} + \hbar\mathbf{k}|. \tag{4.1}$$

When the atom re-emits the photon this will happen in a random direction. Using a short-lived transition for this process, scattering many photons, the net-effect will be a reduction of the atoms momentum, as the absorbtion process lowers it, and the temporary rise by emission averages out over many cycles. The value of the detuning and the power of the laser beam determine the speed and final temperature of the atom, where the lowest possible temperature is given by the linewidth of the atomic transition Γ used for cooling. This *Doppler limit* is given by

$$T_{\mathrm{D}} \simeq \frac{\hbar\Gamma}{2k_{\mathrm{B}}} \tag{4.2}$$

with k_{B} the Boltzmann constant and T_{D} the final Doppler-temperature[1]. The exact value of the Doppler limit temperature depends on the emission pattern and the geometry of the laser beam(s). Values for ions are derived in [IW82, WDW78]. The maximum cooling rate is achieved if the laser detuning from the atoms transition is $\delta \simeq -\Gamma/2$.
As $^{40}Ca^{+}$ needs an 866 nm laser beam for repumping, which is (as discussed in section 4.1) typically blue detuned, this will add a heating process. As the branching ratio favours the cooling transition by 20:1, this is under normal conditions not an issue. In contrast to cold atoms experiments (where the laser beams during Doppler cooling also form the magneto-optical trap) only one laser beam direction is needed for Doppler cooling as long as its k-vector has a sufficient projection on all three motional axes of the ion(s).
In our setup Doppler cooling is performed with the same set of lasers as fluorescence detection, but with beam powers reduced to approx. half a saturation intensity and with both 397 nm frequency components red detuned by roughly 10 MHz compared to their setting for fluorescence detection. In experiments Doppler cooling was optimized together with sideband cooling by trying to achieve the strongest red sideband extinction and the highest contrast for blue sideband Rabi oscillations. As the main task of Doppler cooling in these experiments is to reduce the ions motional population to be well in the Lamb-Dicke regime and not to be as cold as possible, no optimization of the final Doppler temperature was performed. The axial mode was measured to have a mean occupation of $\bar{n} \approx 10$ quanta after Doppler cooling, estimated from blue sideband flopping (see section 5.2.2 for the method).

[1] Here is assumed that the Doppler limit is much higher than the average recoil from photon emission.

4.3.2 Internal State preparation

The internal state preparation is performed by 'frequency-selective optical pumping' with linearly polarized light from a laser beam which enters the trap perpendicular to the applied magnetic field. The σ^+ polarization component of the 397 nm light is resonant with the $\left|S_{1/2}, M_J = -1/2\right\rangle \leftrightarrow \left|P_{1/2}, M_J = +1/2\right\rangle$ transition. Since the $S_{1/2}$ states are split by 334 MHz and the $P_{1/2}$ states are split by 110 MHz in the field of 119 G, the σ^- polarization component is 444 MHz from resonance. As coherence is negligible in this process a calculation with rate equations was performed to estimate the limit on the fidelity arising from the off-resonant pumping. At one saturation intensity, the $S_{+1/2}$ state preparation fidelity can be calculated to be 0.9973. At 1/40 of a saturation intensity, rate equation simulations indicate that fidelities of 0.9991 are achievable. For an unknown reason the time required for pumping is 100 times faster in the simulations than in the experiment. Detuning the 397 nm light by an unrealistic 85 MHz from resonance would result in the desired pumping time with a population of the $S_{+1/2}$ level of 0.97 after 20 µs optical pumping. Introducing a polarisation impurity by adding a fraction of pi polarized 397 nm light does not slow the pumping down significantly but affects the final populations. Including the $D_{3/2}$ levels together with the 866 nm laser did not slow down the pumping process in the simulations significantly. Plots of the $S_{1/2}$ population in the experiment and from simulation are shown in figure 4.5.

4.3.3 Resolved Motional Sideband Cooling

To cool the ions motion to the ground state sideband cooling is performed after Doppler cooling. In our experiments this is typically done with a pulsed method, where first a red sideband pulse is applied, followed by a combined $D_{3/2}$ repump (854 nm) and spin preparation (397 nm σ polarized and 866 nm) pulse. This *cycle* cools the ion by combining the coherent operation of the red sideband pulse, which takes out a quantum of motion and rotates the spin from down to up, with the spin dissipation, resetting the spin with only marginal effect on the ions motion. To cool the ion to its motional ground state a sequence of 60 to 100 cooling pulses is applied. The duration of the red sideband pulse is ramped linearly in duration from the beginning to the end of the sideband cooling sequence, to provide efficient cooling of the different Fock states $|n\rangle$, as their red sideband Rabi frequencies scale with $\sqrt{n}$. The start time is estimated from red sideband flopping after Doppler cooling which gives an indication of the highest N states populated by estimating the highest Rabi frequency. The end pulse time can be estimated from the carrier π-time and the Lamb-Dicke parameter. All parameters were optimized to yield best contrast on blue sideband flopping after sideband cooling. After sideband cooling, the spin is optically pumped, and a blue sideband π pulse is applied. Under perfect conditions the sideband cooling with the subsequent

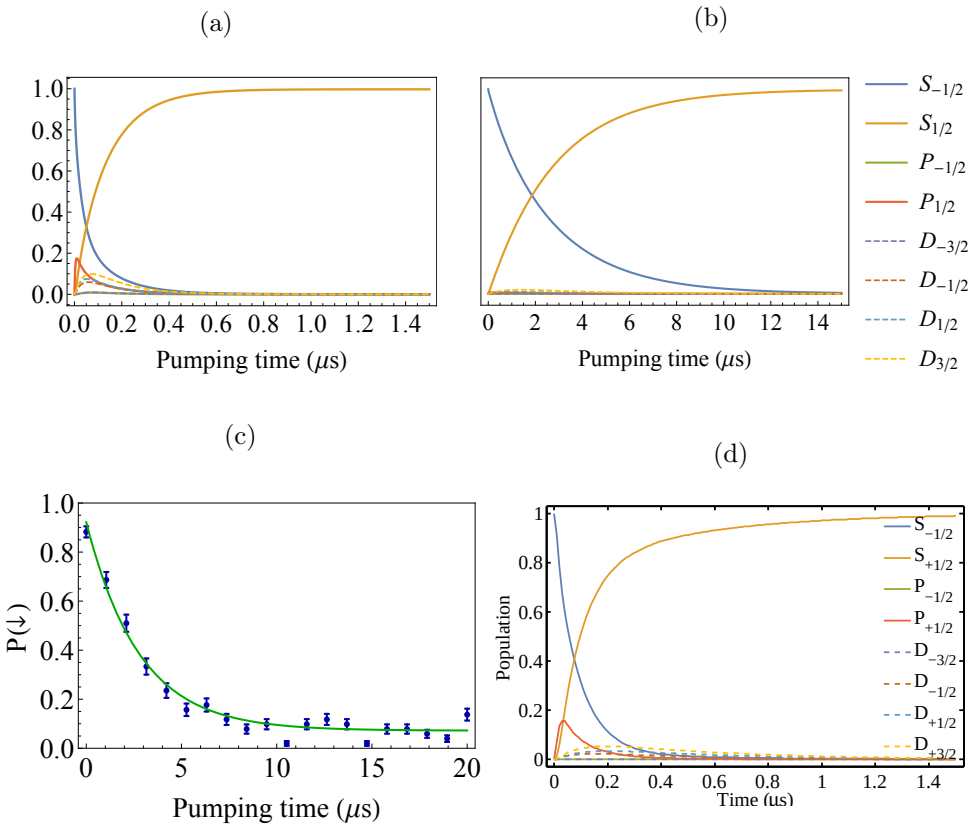

Figure 4.5: (a) Results from the rate equations with 1.4 saturation intensities in the 397 nm beam yielding a $1/e$ pumping time of 0.13 µs and a occupation of the $S_{J=1/2,m_J=+1/2}$ level of 0.997 after 20 µs. (b) Results from the rate equations with $1/40$ saturation intensities in the 397 nm beam, chosen for a higher fidelity of the final state, yielding in a $1/e$ pumping time of 2.5 µs and a occupation of the $S_{J=1/2,m_J=+1/2}$ level of 0.999 after 20 µs (c) Pumping signature in the experiment: Observed is the population of the $S_{1/2}$ levels when the duration of the internal state preparation pulse is scanned, followed by a fixed length pulse with the 729 nm laser shelving the population of the $S_{J=1/2,m_J=+1/2}$ level to the $D_{J=5/2,m_J=+3/2}$ level, thus only leaving population in the $S_{J=1/2,m_J=-1/2}$ level for the final detection pulse. The $1/e$ pumping time estimated from the data by fitting an exponential decay is 2.8(2) µs. This is roughly 20 times longer than the theoretical predictions. The 397 nm power incident on the ion was estimated from measurements of the laser beam's power before and after the vacuum chamber to 1.4 saturation intensities. (d) Results from the optical Bloch equations of the optical pumping to the $S_{J=1/2,m_J=+1/2}$ level to check for the influence of possible coherences. This contains no 397 nm σ_- beam component. The intensities are chosen to be the same as in the calculation from rate equations (1.4 saturation intensities in the 397 nm beam). As expected no major difference to the calculation form rate equations in the pumping time is found.

optical pumping results in the state $|\downarrow, 0\rangle$, which turns into $|\uparrow, 1\rangle$ through the blue sideband π-pulse. In a non-perfect situation the spin population will not be completely transferred to $|\uparrow\rangle$. Reading out the spin state by fluorescence detection provides a signature for the sideband cooling. While scanning the value of a parameter to be optimized, the spin population is observed, choosing the new value for the parameter where the population of $|\uparrow\rangle$ is highest. As correlation between several variables exist, this is typically an iterative process, looping over the different parameters.
It is also possible to replace the blue sideband pulse by a carrier π-pulse followed by a red sideband π-pulse. This operation also adds a quantum of motion but ends up in the spin-down state, contrary to the blue sideband π-pulse. As the carrier is almost motion-insensitive, this provides a possibility to calibrate the red sideband frequency and π-pulse duration.
Non-optimal pumping was observed when the axial mode was to close to a radial mode or the servo bumps (see section 3.4.1). In that case the dc trapping voltages had to be changed to shift the frequency of the axial mode to a better value.
Continuous sideband cooling was also tested, where the red sideband, the repumping and spin preparation lasers are turned on simultaneously for a single long pulse. It performs faster ($\sim 2\,\mathrm{ms}$) than the pulsed method ($\sim 20\,\mathrm{ms}$) with the drawback of AC-Stark shifts caused by the 854 nm laser, which makes the 729 nm transition frequency dependent on the 854 nm laser power. It was harder to maintain over long time periods, as the amplitude of the 854 nm laser was drifting. This was also the case for the environment engineering experiments described in chapter 5. Except where noted all experiments use the pulsed method for sideband cooling. To measure the mean Fock state occupation after sideband cooling two standard techniques were used. The first is using the ratio of the red and blue sideband excitation to determine $\bar{n}$ [LBMW03]. As the blue sideband Rabi frequencies are given by $\Omega_{n,n+1} = \Omega\eta\sqrt{n+1}$ but the red sideband Rabi frequencies by $\Omega_{n,n-1} = \Omega\eta\sqrt{n}$ the difference can be used by comparing the excitation from both on the thermal state after sideband cooling. The mean vibrational quantum number is given by

$$\bar{n} = \frac{P_{\mathrm{e,rsb}}/P_{\mathrm{e,bsb}}}{1 - P_{\mathrm{e,rsb}}/P_{\mathrm{e,bsb}}} \tag{4.3}$$

with $P_{\mathrm{e,rsb}}$ ($P_{\mathrm{e,bsb}}$) the population of the $|\uparrow\rangle$ after a red (blue) sideband pulse. This method is independent of the pulse time, Rabi frequency and Lamb-Dicke parameter, as long as the values are the same for both the red and blue sideband pulse. Therefore this method delivers an easy to calculate, robust measure of $\bar{n}$. It is not well suited to estimate $\bar{n}$ close to 0 as $P_{\mathrm{e,rsb}} \to 0$, where off-resonant carrier excitation are starting to be a noticeable effect. The second method is better suited for precise measurements. It extracts the Fock state populations from blue sideband Rabi oscillations and is described in section 5.2.2. After sideband cooling the mean Fock state occupation was

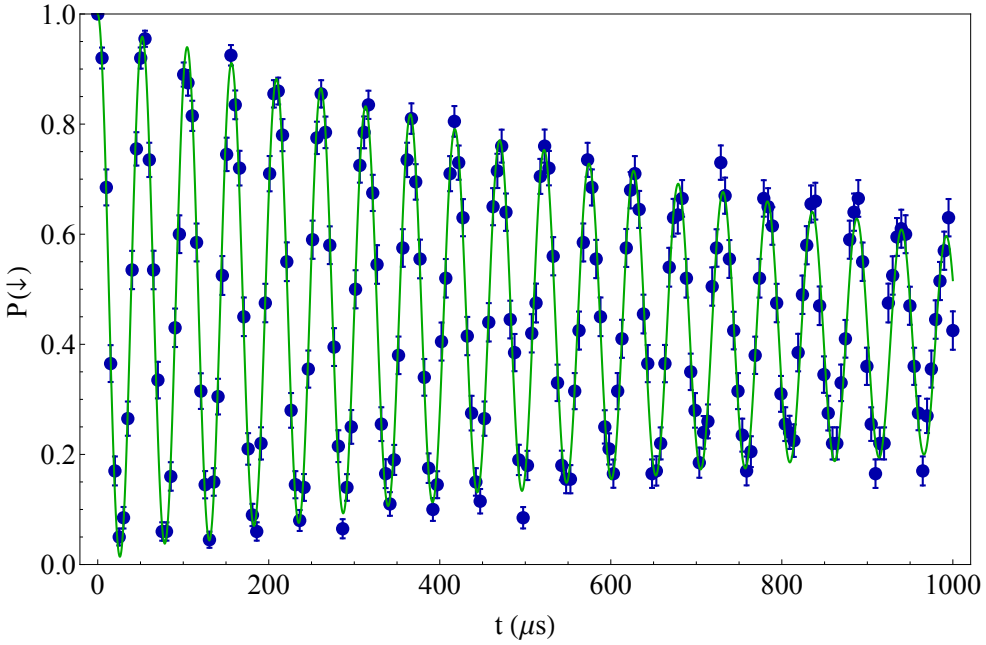

Figure 4.6: Data for blue sideband Rabi oscillations of a ground-state cooled ion. Fitting the Rabi oscillations as described in section 5.2.4 assuming a thermal distribution for the n-states yields a mean energy eigenstate occupation of $\bar{n} = 0.014(8)$.

determined with the second method to be $\bar{n} = 0.014(8)$ quanta. The data of this measurement is shown in figure 4.6.

4.3.4 Fluorescence Detection

Detection and measurement of the $^{40}Ca^{+}$ atoms is done via the $S_{1/2}$ to $P_{1/2}$ transition by collecting photons at 397 nm scattered by the ion from the incident laser beam. This allows the imaging of ions on a camera as well as photon counting with a PMT. The camera is generally used for counting the number of ions if the photon counts per ion are not calibrated and to check the spatial configuration for multiple ions. Cameras have the drawback of slow readout times (∼ms). In contrast, PMTs are fast in readout but feature no spacial resolution, which makes them the optimal choice for experiments with single ions. Thus a PMT is used to measure fluorescence levels for optimizing fluorescence and for internal state detection. For a detection pulse the 397 nm σ and π-beams are tuned to resonance with 1-2 saturation intensities and turned on together with the 866 nm laser for $\approx 300\,\mu s$.
The fluorescence of the ion is detected with the imaging system resulting in a number of photon counts for a given detection time. This is used to determine the spin state, i.e. whether the ion was in the $D_{3/2}$ or the $S_{1/2}$ state). A normal

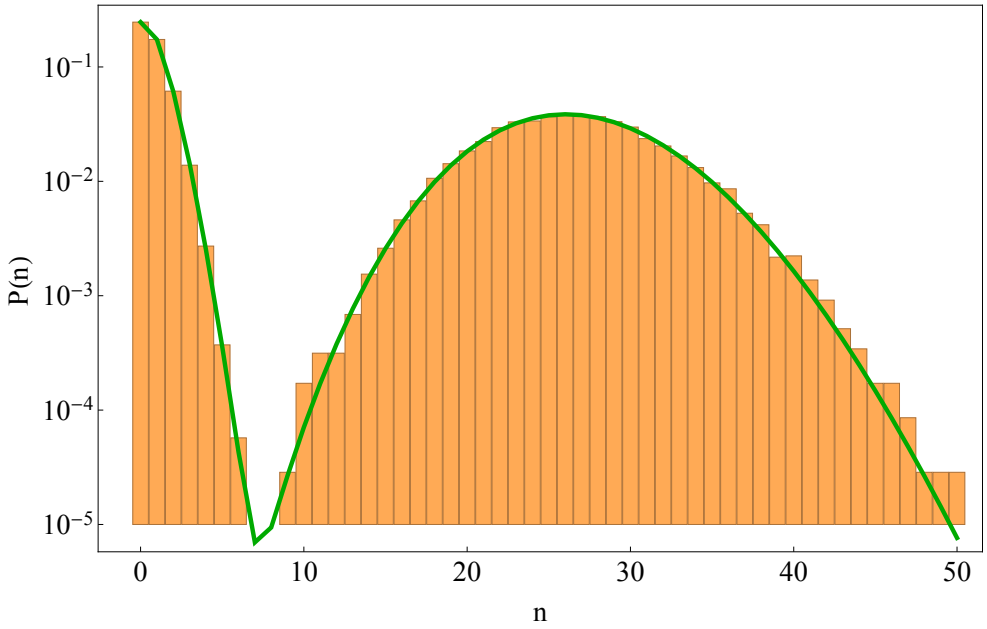

Figure 4.7: Histogram of 35000 single detections with the number photon counts per shot for a detection time of 300 µs. Bins close from 0 to 7 correspond to the ion being dark, i.e. the electron being shelved to the D level. The higher counts correspond to the ion being bright, i.e. the electron in the S state. The green trace shows a fit to the data with two Poisson distributions, yielding the mean values 0.705(2) and 26.54(4) counts. With a threshold at 7 counts the states $|\downarrow\rangle$ and $|\uparrow\rangle$ can be discriminated better than $1 : 10^5$.

fluorescence level (25 counts) indicates the $S_{1/2}$ state and photons detected on the background level (0.5 counts) indicate the ions being in the $D_{3/2}$ state, not scattering any photons. Background-subtracted detection [Luc12] can be performed by applying a second pulse with only the 397 nm beams on, shelving the ion to the $D_{3/2}$ state and recording the background level of 397 nm light incident on the PMT. Subtracting these counts from the results of the first detection pulse gives the background subtracted counts. This technique was mainly used during loading, when fluorescence counts are low.

Error Estimation

For all data and the fits to it the statistical uncertainty of a binomial distribution was used, i.e. for N single measurements with the same experimental parameters $\mathbf{x}$ and the measured mean probability $p(\mathbf{x})$ the uncertainty is given by

$$u_p(\mathbf{x}) = \sqrt{\frac{p(\mathbf{x})(1-p(\mathbf{x}))}{N}}. \tag{4.4}$$

This most likely underestimates the error as systematic effects are neglected. As parameters of the experimental setup are fluctuating (laser frequencies and powers) there will be a systematic fluctuation in the data, currently not accounted for. This assumption is strengthened as all fits to the data have χ^2 values higher than 1, indicating that the probability distribution of the data is not sufficiently well described by equation 4.4.

4.4 Micromotion Compensation

To detect micromotion several techniques were applied. For the simplest method the micromotion sideband in the 397 nm fluorescence was compared to the carrier signal and minimized. This utilizes the fact that the optical transition has a linewidth of 20 MHz but the rf drive frequency is around 100 MHz and thus the sidebands may be well resolved. With this measurement of the micromotion amplitude the voltages of the shim voltages were adjusted to minimize the size of the micromotion sideband and maximize the carrier. Example fluorescence scans are shown in figure 4.8.
For the single ion experiments performed in this thesis this has proven to be sufficient. The technique has several shortcomings though. Most fundamental it is only measuring the micromotion amplitude along the direction of the laser beam. Micromotion in the transversal plane is not detected. This is no severe issue in our experimental setup as all but the 729 nm laser beams are at the same angle as the 397 nm probe beam. For the 729 nm beam this leads to reduced Rabi frequencies. As the trapping potential is highly harmonic no heating effects are expected for a single ion. The identification of the sidebands has proven to be difficult with this method, as it is easily possible to mistake the second micromotion sideband for the first and the first for the carrier. Using the 729 nm beam to probe for micromotion is not possible in our setup as the modulation frequency is to high to probe the sidebands by shifting the 729 nm with the AOMs.
As derived in section 2.3.2 ions of different mass are not displaced by the same distance in the presence of a stray field in radial direction. Thus a two-ion mixed species crystal would not align along the axial direction but tilt. This leads to a coupling of the axial and radial modes of motion. If not all motional modes are cooled to the ground state this can cause heating of a cold mode by a hotter mode. It is therefore necessary to compensate the stray field completely when working with mixed species ion crystals. To detect micromotion along both principal axes in the radial plane it is possible to use a second laser beam to obtain a second spectroscopic signal along a direction complementing the first measurement. Ideally this beam would have a projection onto the radial plane perpendicular to the first beam. In our setup this axis is not accessible. A second option is the use of amplitude modulation of the rf trap drive at the radial trap frequencies [BMB$^+$98]. If the ion is sitting in the rf null, the

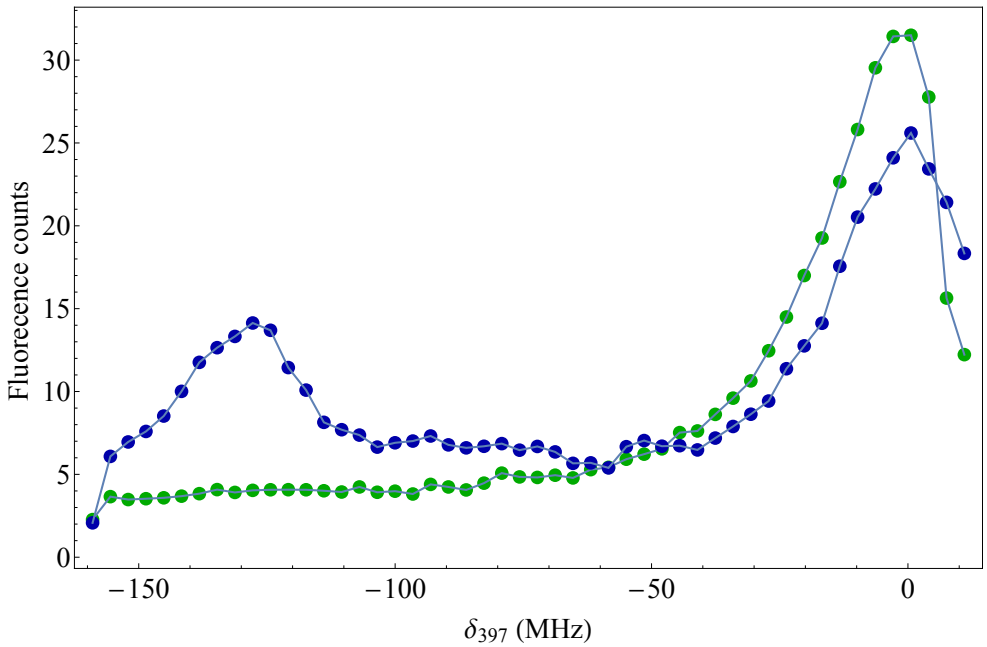

Figure 4.8: Fluorescence spectrum of the $S_{1/2}$ to $P_{1/2}$ transition. The blue data points are for an ion with micromotion in direction of the probing 397 nm laser beam. The resonance (at 0 MHz) and the first micromotion sideband (at −130 MHz) are clearly visible. Their frequency difference correspond to the trap drive frequency of 105 MHz. The difference of 25 MHz is due to a calibration error of the cavity used for scanning the 397 nm laser. The green data points show the same scan with the micromotion being compensated with the shim electrodes. Clearly the magnitude of the micromotion sideband is minimized and the carrier increased.

slope of the pseudopotential is zero. Changing the rf drive amplitude will not change the ions position. If the ion is not in the rf null, the slope of the pseudopotential is non-zero, thus a modulation of the rf drive power will lead to an oscillating motion of the ion with the modulation frequency. If this frequency is chosen to be equal to one of the radial modes frequencies, the ion will heat up, which can be detected either by loss of fluorescence for strong excitations or by red sideband spectroscopy, analysing the motional heating[2]. This method was briefly tested using strong modulation and fluorescence detection, but is not yet implemented as the standard method for micromotion compensation in our setup.

[2]For this the ion would need to be cooled close to the ground state of the observed radial mode prior to the amplitude modulation.

4.5 Spin Coherence

To determine the spin coherence of the system, i.e. the combined stability of the laser and the ion qubit transition Ramsey interferometry experiments were performed[Ram98]. For this the ion is prepared in the spin-superposition state

$$|\psi\rangle = \frac{1}{\sqrt{2}}\left(|\downarrow\rangle - e^{-i\,\Phi_1}\,|\uparrow\rangle\right) \tag{4.5}$$

by first preparing the $|\downarrow\rangle$ state as described in section 4.3.2 followed by a $\pi/2$ carrier-pulse to rotate the spin, which carries the phase Φ_1 of the laser, now imprinted onto the ion's state. After this the spin is left to evolve freely for a time period τ to the state

$$|\psi\rangle = \frac{1}{\sqrt{2}}\left(|\downarrow\rangle - e^{-i(\Phi_{\mathrm{ion},\tau}+\Phi_1)}\,|\uparrow\rangle\right), \tag{4.6}$$

where $\Phi_{\mathrm{ion},\tau}$ is the collected phase of the ion during the wait time τ. In general this is calculated from $\Phi_{\mathrm{ion},\tau} \equiv \Phi_{\mathrm{ion}}(t_1,t_2) = \int_{t_1}^{t_2}\omega_{\mathrm{ion}}(t)\,\mathrm{d}t$. In the ideal case that the ions frequency is constant this would simply result in $\Phi_{\mathrm{ion},\tau} = \omega_{\mathrm{ion}}\tau = \omega_{\mathrm{ion}}(t_2 - t_1)$. In the same way the phase of the laser $\Phi_{\mathrm{laser},\tau}$ is accumulated during the wait time τ. Applying a second $\pi/2$ pulse with phase[3] Φ_2 the following state is formed

$$|\psi\rangle = \frac{1}{2}\left[\left(|\downarrow\rangle - e^{-i(\Phi_{\mathrm{laser},\tau}+\Phi_2)}\,|\uparrow\rangle\right) - e^{-i(\Phi_{\mathrm{ion},\tau}+\Phi_1)}\left(e^{i(\Phi_{\mathrm{laser},\tau}+\Phi_2)}\,|\downarrow\rangle + |\uparrow\rangle\right)\right]. \tag{4.7}$$

Introducing the relative laser phase $\Delta\Phi = \Phi_2 - \Phi_1$ and the relative accumulated ion-laser phase $\delta\Phi_\tau = \Phi_{\mathrm{laser},\tau} - \Phi_{\mathrm{ion},\tau}$ and reordering the components the state may be written as

$$|\psi\rangle = \frac{1}{2}\left[\left(1 - e^{i(\delta\Phi_\tau+\Delta\Phi)}\right)|\downarrow\rangle - e^{-i(\Phi_{\mathrm{laser},\tau}+\Phi_2)}\left(1 + e^{i(\delta\Phi_\tau+\Delta\Phi)}\right)|\uparrow\rangle\right]. \tag{4.8}$$

Finally performing a measurement of the spin's state the probability

$$P_\downarrow(\delta\Phi_\tau,\Delta\Phi) = \frac{1}{2}\left(1 - \cos\left(\delta\Phi_\tau + \Delta\Phi\right)\right) \tag{4.9}$$

can be retrieved. In the ideal case that the laser is on resonance and no fluctuations of the ion or the laser frequencies are present $\delta\Phi_\tau = 0$ and the final state is only determined by the relative phase $\Delta\Phi$ chosen by the experimenter. Repeating the experiment to build up statistics and using different settings of $\Delta\Phi$ the cosine curve will be retrieved. In case of a fluctuating phase $\delta\Phi_\tau$ the probability for the experiments outcome will be different for each shot

[3] This phase is an offset referenced to the phase of the first $\pi/2$ pulse Φ_1. With our DDS setup the values of both pulses can be set independently.

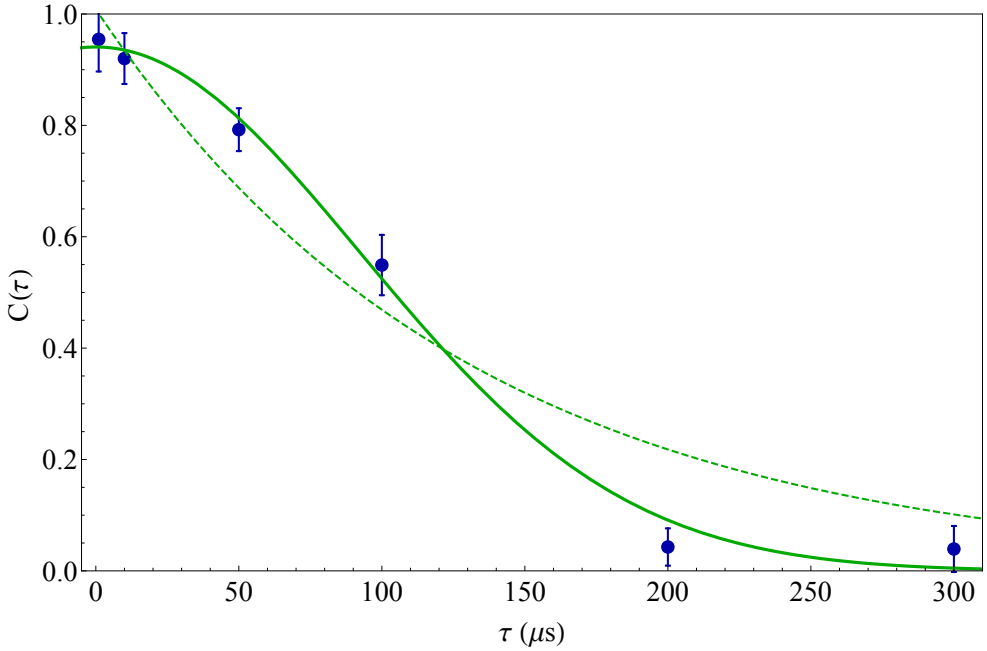

Figure 4.9: Ramsey experiment data with wait time τ between $\pi/2$ pulses for the qubit transition ($S^{+1/2} - D^{+3/2}$) with a Gaussian fit (green solid line)) $C(\tau) = A\, e^{-\tau^2/(2\tau_{\mathrm{Spin}}^2)}$, which yields $A = 0.94(2)$, $\tau_{\mathrm{Spin}} = 93(4)\,\mu\mathrm{s}$ and $\chi^2 = 1.7$, and an exponential fit (green dashed line), which yields $A = 1.01(7)$, $\tau_{\mathrm{Spin}} = 130(30)\,\mu\mathrm{s}$ and $\chi^2 = 20.0$.

and the retrieved cosine curve will have reduced contrast parameterised by $C(\tau) \in \{0, 1\}$ and possibly an offset $\langle \delta\Phi_\tau \rangle$:

$$\langle P_\downarrow(\tau, \Delta\Phi) \rangle = \frac{1}{2} \left(1 - C(\tau) \cos\left(\langle \delta\Phi_\tau \rangle + \Delta\Phi\right)\right) \tag{4.10}$$

The form of $C(\tau)$ depends on the spectral properties of the noise. Thus the the spin decoherence may take different forms. For a noise spectrum dominated by frequency components smaller than the inverse of the wait time τ the spin decoherence may be modelled by a Gaussian or an exponential decay. If the noise spectrum is dominated by components larger than the inverse of the wait time τ it is often better described by an exponential decay [Hom06].
The Ramsey experiments are performed with Doppler cooled ions only, as the experiment does not make use of the ions motion and the carrier is sufficiently insensitive to the ions temperature.

A Ramsey experiment on the qubit transition was performed by choosing different wait times τ and scanning the relative phase of the $\pi/2$ pulses $\Delta\varphi$ for each wait time. The resulting sine curves were fitted with $P_\downarrow(\varphi) = 1/2 + C \sin(\varphi + \delta)$ to extract the contrast C. The full C vs τ data was then fitted

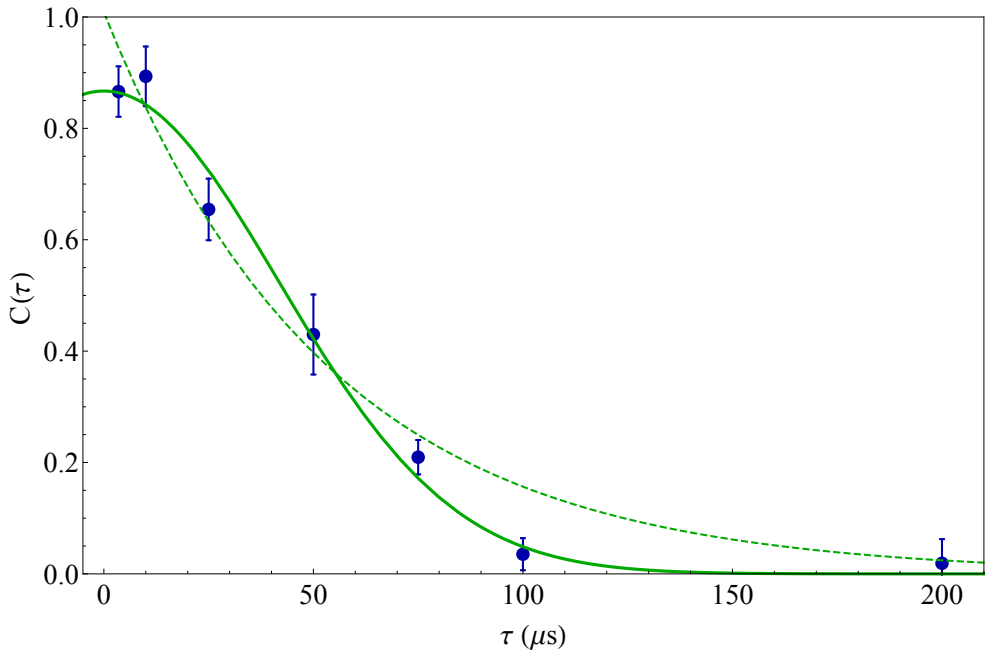

Figure 4.10: Ramsey experiment data with wait time τ between $\pi/2$ pulses for the $S^{+1/2} - D^{-1/2}$ transition with a Gaussian fit (green solid line)) $P(\downarrow) = A\, e^{-\tau^2/(2\tau_{\mathrm{Spin}}^2)}$, which yields $A = 0.87(3)$, $\tau_{\mathrm{Spin}} = 42(2)\,\mu\mathrm{s}$ and $\chi^2 = 2.2$, and an exponential fit (green dashed line), which yields $A = 1.01(6)$, $\tau_{\mathrm{Spin}} = 53(7)\,\mu\mathrm{s}$ and $\chi^2 = 11.9$. As the coherence times are half the values of the qubit transition, this suggests the magnetic field noise is the dominant effect in the spin decoherence.

with a Gaussian decay function $C(\tau) = A\, e^{-\tau^2/(2\tau_{\mathrm{Spin}}^2)}$ and with an exponential decay function $P(\downarrow) = A\, e^{-\tau/\tau_{\mathrm{Spin}}}$. The reduced χ^2-values favour the Gaussian fit, which yields $A = 0.94(2)$, $\tau = 93(4)\,\mathrm{ms}$ and $\chi^2 = 1.7$. The results for the exponential fit are $A = 1.01(7)$, $\tau = 130(30)\,\mathrm{ms}$ and $\chi^2 = 20.0$. This suggests that the noise spectrum is dominated by slow fluctuations compared to the wait time τ. The C vs τ data and the Gaussian and exponential fits are shown in figure 4.9.

To separate the contributions from magnetic field noise and laser frequency fluctuations a second Ramsey experiment on the $S_{+1/2} - D_{-1/2}$ transition was performed. This transition is twice as sensitive to magnetic fields compared to the qubit transition $S^{+1/2} - D^{+3/2}$. The transition is 402 MHz lower in frequency than the qubit transition. This could be conveniently reached by not using the switching AOMs (depicted in figure 3.31), but instead using the zeroth order beam of that setup and using the AOM in front of the optical fibre (depicted in figure 3.30) to pulse the beam. This also did not require any change in the laser lock, making sure the lock performance is the same

as in the experiment on the qubit transition, and thus resulting in the same contribution to the decoherence. The data was again fitted with Gaussian and exponential functions yielding $A = 0.87(3)$, $\tau = 42(2)\,\mathrm{ms}$ and $\chi^2 = 2.2$ for the Gaussian fit and $A = 1.01(6)$, $\tau = 53(7)\,\mathrm{ms}$ and $\chi^2 = 11.9$ for the exponential fit, again suggesting low frequencies dominating the noise spectrum. The C vs τ data and fits are shown in figure 4.10. Within error bounds this coherence time is half as long as the previous result, which indicates that the coherence time is limited by magnetic field noise. This result is expected as the experimental setup has no compensation, stabilization or shielding for magnetic field noise. As typically for a locked laser the higher frequencies are limiting and magnetic field noise is dominated by slow frequencies from the fields created by electrical currents from mains supply at 50 Hz and multiples also the Gaussian fit suggests a magnetic field limited coherence time. In later experiments the laser linewidth was measured by beating the laser used in the experiments with a second narrow-linewidth laser. This measurement gives a lower bound on the linewidth of the laser of $\sim 10\,\mathrm{Hz}$, which would result in a coherence time $\simeq 100\,\mathrm{ms}$ (without magnetic field noise present). The measurement was performed by C. Flühmann.

4.6 Heating Rate

The ions motional state is coupled to an amplitude reservoir, which originates typically from fluctuating electric fields. For the motional ground state $|0\rangle$ this results in a 'heating' to a thermal state with a mean Fock state $\bar{n}$. The increase of $\bar{n}$ is linear for short times compared to the time for the ion to be fully thermalized with its environment (which is at 300 K) [TMK+00]. The heating rate $\dot{\bar{n}}$ was measured with the standard technique of comparing the level of excitation for the red and blue sidebands of motion (see for instance [LBMW03] after preparing the ion in the motional ground state and waiting for a time τ. The ratio of the excitation of the two sidebands is given by $R = P_{\uparrow,\mathrm{rsb}}/P_{\uparrow,\mathrm{bsb}}$ and the mean motional excitation may be calculated as

$$\bar{n} = \frac{R}{1-R}. \tag{4.11}$$

Repeating the experiments with different wait times τ gives the data presented in figure 4.11, which is fitted with a linear function $\bar{n}(t) = \dot{\bar{n}}t$. This results in a heating rate of

$$\dot{\bar{n}} = 10.7(8)\,\mathrm{quanta/s} \tag{4.12}$$

for a $^{40}Ca^{+}$ with a trap frequency $\omega = 2\pi \times 1.95\,\mathrm{MHz}$. From this the electric field noise spectral density can be inferred, which is independent of the trap frequency and the ions mass and thus useful to compare the performance of

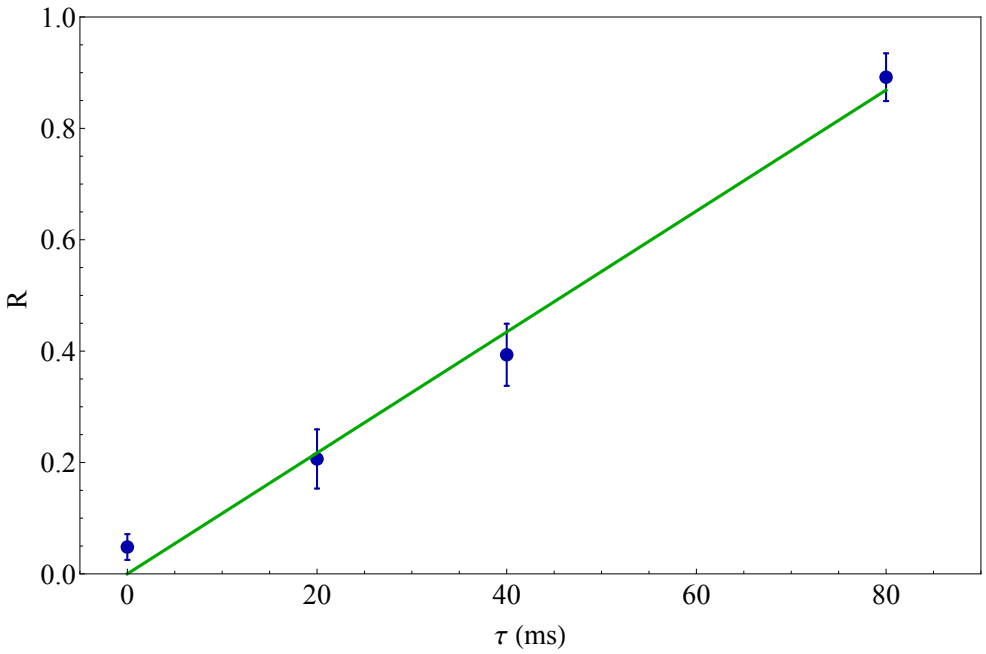

Figure 4.11: Data for ratio of sidebands R for different wait times τ fitted with a linear function $R(\tau) = c - \dot{\bar{n}}\tau$, yielding a heating rate of $\dot{\bar{n}} = 10\,\text{quanta/s}$.

different traps. It is given by

$$S_E(\omega) = \dot{\bar{n}} \frac{4m\hbar\omega}{e^2}, \tag{4.13}$$

where m is the ion's mass, $\hbar$ Plank's constant and e the electric charge. As discussed in [TKK+00] a scaling of $\omega S_E(\omega) \sim d^{-4}$ is theoretically predicted from microscopic fluctuating patch potentials, with d the distance of the ion to the closest electrode surface. For this trap it is

$$\omega S_E(\omega) = 1.8(1) \times 10^{-6}\,\text{V}^2\,\text{m}^{-2}, \tag{4.14}$$

with $d \approx 184\,\mu\text{m}$. This is in comparison a relatively low value, which might be explained by the comparably thick gold layer of the trap and the final cleaning step with Piranha etch described in 3.2.3. It should be mentioned though that the value for the trap described in [Bla10] has only a marginally worse value of $\omega S_E(\omega) = 5 \times 10^{-6}\,\text{V}^2\,\text{m}^{-2}$. This suggests that the general fabrication recipe is suited for producing traps with low heating rates. The design goal for the heating rate set in section 3.2 was exceeded by a factor of 3.

4.7 Motional Coherence

The fluctuating electric fields causing the heating rate measured in section 4.6 will also cause a decoherence of Fock state superpositions. Turchette *et*

al. [TMK+00] derived the decoherence of several quantum states coupling to different reservoirs. The result of interest here is the decoherence of Fock state superpositions in amplitude reservoirs. The decay of the density matrix element $\hat{\rho}_{0,m}$, expressing the coherence between the Fock state $n = 0$ and $n = m$, is given by

$$\hat{\rho}_{0,m}(t) = \frac{1}{2(1+\dot{\bar{n}}t)^{1+m}}. \tag{4.15}$$

Another source of motional dephasing is a drifting trap frequency, which would not contribute to the heating rate. This can be modeled by a phase reservoir. The motional coherence is also of major importance for the squeezed states produced in chapter 5, as they dephase much faster.
The dephasing was measured for a superposition of the ground and first excited state. This superposition state is prepared by initialising the ion in the motional ground state and applying first a $\pi/2$ carrier pulse followed by a π red sideband pulse.

$$|\Psi_{\text{start}}\rangle = \frac{1}{\sqrt{2}}\left[|\downarrow,0\rangle + |\downarrow,1\rangle\right]. \tag{4.16}$$

The ion is left for a wait time τ in which a fluctuation of the trap frequency leads to a relative phase shift between the 0 and 1 Fock states:

$$|\Psi_{\text{shift}}\rangle = \frac{1}{\sqrt{2}}\left[|\downarrow,0\rangle + e^{\varphi(\tau)}\,|\downarrow,1\rangle\right]. \tag{4.17}$$

Then the population is transferred back to the ground state $|\downarrow,0\rangle$. Any motional dephasing will now inscribed in the spin state as

$$|\Psi_{\text{final}}\rangle = \frac{1}{2}\left[(1+e^{i\varphi(\tau)})\,|\downarrow,0\rangle + (1-e^{i\varphi(\tau)})\,|\uparrow,0\rangle\right]. \tag{4.18}$$

Finally the spin state is measured. Averaging over many experiments gives a reading of the phase shift experienced by the ion. If this shift is random, repeating the experiment will give an average loss in contrast of the resulting sine curve, where the loss in contrast is depending on the wait time τ. Assuming only decoherence due to heating of the ion (an amplitude reservoir), it should be described by 4.15. The decoherence of the superposition state Ψ_{01} is then given by

$$P(\downarrow) = \hat{\rho}_{01}(t) + \hat{\rho}_{10}(t) = \frac{1}{(1+\dot{\bar{n}}t)^2}, \tag{4.19}$$

with the final motional state described by the density matrix $\hat{\rho}$, with the sum of the two off-diagonal elements $\hat{\rho}_{01}$ and $\hat{\rho}_{10}$ expressing the coherence of the superposition state (yielding 1 at $t = 0$). The heating rate derived from the dephasing is found from a fit with $P(\downarrow) = A/(1+\dot{\bar{n}}_{\text{dephase}}t)^2$ to the experimental data (see figure 4.12) as

$$\dot{\bar{n}}_{\text{dephase}} = 21(3)\,\text{s}^{-1}. \tag{4.20}$$

This is twice the expected value from the heating rate measurement given in section 4.6. This means that a not identified source of motional dephasing must exist in the setup. The data was fitted again with an exponential decay $P(\downarrow) = A/\exp(-t/\tau_{\text{dephase}})$ yielding a decoherence time of

$$\tau_{\text{dephase}} = 32(3)\,\text{ms}. \tag{4.21}$$

The value of the decoherence time was not constant for measurements taken on different dates. In total four measurements were taken. For all data sets the same fits were performed as described above, yielding a decoherence time for the exponential decay and a rate for fitting with equation 4.19. The results are: on 12.05.2014 $\tau_{\text{dephase}} = 16(1)\,\text{ms}$ decoherence time and rate $\dot{\bar{n}}_{\text{dephase}} = 40(5)\,\text{s}^{-1}$, on 26.05.2014 with $\tau_{\text{dephase}} = 32(3)\,\text{ms}$ and $\dot{\bar{n}}_{\text{dephase}} = 21(3)\,\text{s}^{-1}$), on 10.06.2014 $\tau_{\text{dephase}} = 22(4)\,\text{ms}$ and $\dot{\bar{n}}_{\text{dephase}} = 31(5)\,\text{s}^{-1}$ and on 10.06.2014 $\tau_{\text{dephase}} = 41(10)\,\text{ms}$ and $\dot{\bar{n}}_{\text{dephase}} = 15(5)\,\text{s}^{-1}$. These values do not agree within 3σ with each other, which suggests that the noise is changing over time.

4.8 Trapping Potentials

Good agreement was found for the axial trapping potential and simulated values from the boundary element method simulation. The radial potentials did not match the values of the simulation and neither did the angle of the radial modes with respect to the laser beams, which was inferred from a measurement of the radial modes Lamb Dicke parameters for the 729 nm laser. This difference could be explained by adding an offset voltage to all dc voltages. With this single parameter the simulation could be matched well with the measurements. The origin of a possible offset voltage is not clear. Its value is around 1 V but changes over weeks. It does seem to be related to the rf drive, as switching the rf drive off for several days got rid of the offset, slowly building up over time again. The ion shuttling and ion chain splitting features of the trap are under current investigation and will be discussed in the future thesis of L. de Clercq. Ions were transported through the whole trap and first successful experiments with splitting and adiabatic transport were performed.

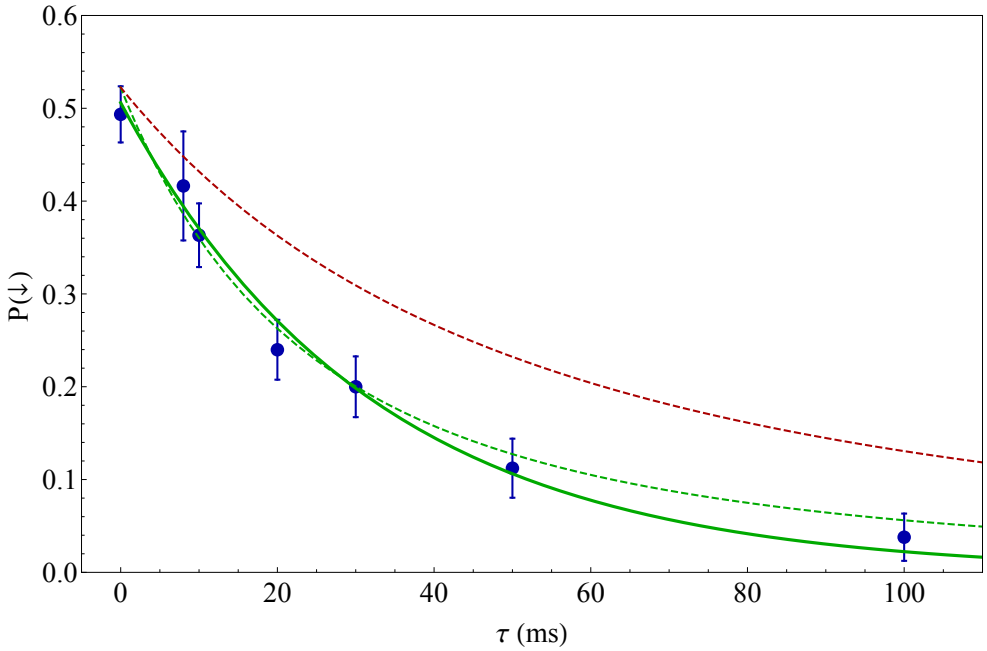

Figure 4.12: Motional coherence data with wait time τ. The green solid curve is a fit to the data using a general exponential decay with $P(\downarrow) = A\, e^{-\tau/\tau_{\mathrm{dephase}}}$ yielding a motional dephasing time $\tau_{\mathrm{dephase}} = 32(3)\,\mathrm{ms}$. The green dashed curve is a fit using the expected form of the dephasing for an amplitude reservoir as dominating source of decoherence $P(\downarrow) = 1/(1 + \dot{\bar{n}}_{\mathrm{dephase}}\, t)^2$, yielding a rate of $\dot{\bar{n}}_{\mathrm{dephase}} = 21\,\mathrm{s}^{-1}$. The red dashed curve shows the expected dephasing using the heating rate as measured in section 4.6 and the amplitude value from the previous fit. This shows that the dephasing is twice as large as expected with an amplitude reservoir predicted by our measured heating being the primary source of decoherence.

Chapter 5

Environment Engineering

In this chapter the experiments performed on dissipative state preparation (DSP) are presented. The general technique described in section 2.5 is used to prepare and stabilize coherent, squeezed and displaced squeezed states of motion, using the axial mode of motion of a single $^{40}Ca^{+}$ ion.
The experimental implementation is described in section 5.1, followed by the analysis of the created states, their fidelities and limits to the technique in section 5.2. The results of this chapter are also covered in two recent publications [KLK+15, LKdC+15].

5.1 Implementation of the Pumping Technique

For the experiments on environment engineering the Hamiltonian $\hat{H}_{\mathrm{ee}}$ given in equation 2.89 is implemented with up to three frequency components of the 729 nm laser. The dissipation is implemented by optical pumping using the 854 nm, 866 nm and 397 nm lasers, where the 854 nm pump can be seen as the dissipative part interrupting the coherent drive and the 866 nm and 397 nm lasers are used to re-prepare the spin in the spin-down state $|\downarrow\rangle$. Similar to sideband cooling described in section 4.3.3, for these experiments two different methods were used. For the *pulsed method* the coherent manipulation and the optical pumping were performed in separate pulses forming a cycle, which is applied repeatedly with up to 300 cycles applied in total. Pulse times depend on the type of state produced but range for the coherent manipulation from 30 µs to 60 µs and are usually set to 20 µs for the optical pumping. This means in some cases a state preparation time of up to 20 ms. For the *continuous method* a single long pulse combining both operations was used with durations up to 6 ms. Details regarding the setup and calibration for both the coherent manipulation and the optical pumping are given in the following sections.

5.1.1 Coherent Manipulations

The 729 nm laser light is prepared as described in section 3.4.1. The Hamiltonians used for the creation, analysis and manipulation of the motional states $\hat{H}_{\mathrm{ee}}$, $\hat{H}_{-}$ and $\hat{H}_{+}$ given in equations 2.89, 2.90 and 2.91 are implemented using three laser fields: one which resonantly drives the carrier transition $|\downarrow\rangle|n\rangle \leftrightarrow |\uparrow\rangle|n\rangle$, a second which resonantly drives the red motional sideband transition $|\downarrow\rangle|n\rangle \leftrightarrow |\uparrow\rangle|n-1\rangle$ and a third which resonantly drives the blue motional sideband transition $|\downarrow\rangle|n\rangle \leftrightarrow |\uparrow\rangle|n+1\rangle$. These laser fields are described by their Rabi frequencies Ω_{car}, Ω_{rsb} and Ω_{bsb}, their phases φ_{car}, φ_{rsb} and φ_{bsb} and their optical frequencies ω_{car}, ω_{rsb} and ω_{bsb}. The conceptual setup in the control software uses a center frequency ω_{center} and the motional frequency ω_{m} of the ion. The frequencies for the single terms are calculated by $\omega_{\mathrm{car}} = \omega_{\mathrm{center}}$, $\omega_{\mathrm{rsb}} = \omega_{\mathrm{center}} - \omega_{\mathrm{m}}$ and $\omega_{\mathrm{bsb}} = \omega_{\mathrm{center}} + \omega_{\mathrm{m}}$.
It is important that ω_{m} matches the motional frequency of the ion well, independent of any Stark shifts on the ion's internal transitions, as otherwise the rotating frame defined by the beatnote of the lasers and the motion of the ion would not match and the target state would constantly precess in phase (and thus never reach a steady state). It should be calibrated with an uncertainty not larger than the inverse of the duration of a single experiment. As the experiments take up to 20 ms a 50 Hz resolution is necessary.
The motional frequency ω_{m} was carefully calibrated using a *tickle* experiment: first the ion was cooled to the ground state of the axial mode followed by optically pumping the spin to $|down\rangle$. Subsequently a rf 'tickle' pulse fed to a non-filtered shim electrode (see section 3.2.3, Carrier/Filter Board) was used to excite the ions motional mode. After this the ion was probed using a red sideband π-pulse, leading to a spin excitation if the ion was successfully excited by the rf tickle pulse and to no excitation if the ion is still in the motional ground state. Repeating this experimental sequence with different values for the frequency of the tickle pulse this experiment can be used to determine the motional frequency.
With this experiment the motional frequency is calibrated with a precision of ~ 20 Hz. A change of the rf trap drive power led to a drift of the frequency. The thermalization process could take up to several days. After the thermalization the motional frequency would not drift over hours within the measured 20 Hz resolution. A typical data set of the calibration is shown in figure 5.1. This experiment has the advantage that no laser is used for excitation, thus avoiding Stark shifts present in a simple red sideband spectroscopy. The drawback of this method is the extremely low rf power needed which drifted, probably due to temperature changes of the fixed-value attenuators used to attenuate the tickle signal produced by DDS channels.
A second method with a detuned laser pulse consisting of the two frequency components $\omega_{\mathrm{car}} + \omega_{\mathrm{m}} - \delta$ and $\omega_{\mathrm{car}} - \omega_{\mathrm{m}} - \delta$ with a detuning $\delta \simeq 200$ kHz was tested later and worked equally well, possibly with the advantage of being

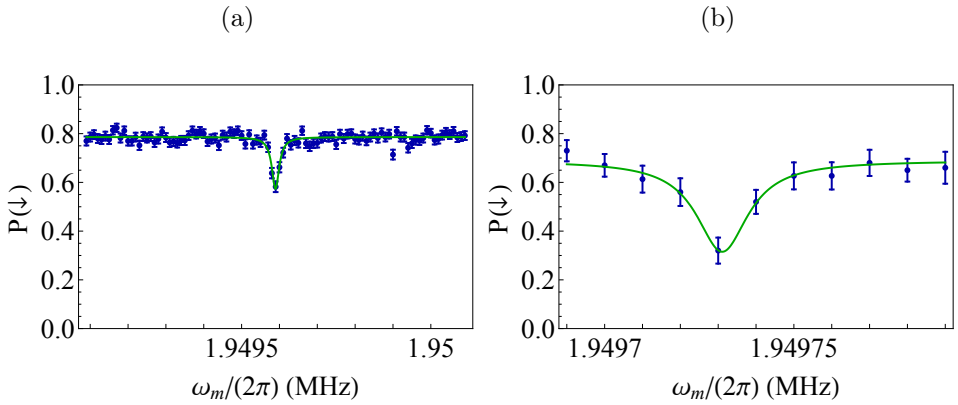

Figure 5.1: Two typical calibration scans of the motional frequency ω_{m}. The data is fitted with a Lorentzian function yielding a linewidth at Full Width Half Maximum (FWHM) of (a) 23(3) Hz, (b) 16(3) Hz.

less affected by drifts (this was not confirmed).
Powers for the frequency components were calibrated either from a photo diode measuring the beam intensities using only one frequency component at a time or by measuring the beat note signal between the laser beam addressing the ion and a reference beam (directly taken from the master output of the 729 nm laser) 200 MHz shifted relative to the experimental beam. The beatnote then contains a carrier component at 200 MHz and the motional sidebands at plus and minus a motional frequency. Both methods were equally reliable. With these values calibrated the other parameters were optimized using directly the dissipative pumping and characterizing the result using a certain 729 nm analysis pulse followed by reading out the spin state. Several different analysis pulses were used, all described in the following sections. For the final experiments the measurement in the engineered basis with the $\hat{H}_+$ was used with a pulse duration close to the $\pi/2$ time, giving the most sensitive signal (see section 5.2.3 for this measurement technique). First ω_{car} was calibrated to account for Stark shifts, which change for different states produced, as the 729 nm laser powers used need to be adapted to account for the different parameters of the state. A scan of ω_{car} can be seen in figure 5.2 with a clear dip marking the resonance. Similar the single pulse durations and the number of pulses for the pulsed method and the length of the pulse for the continuous method were optimized.

Coherent State

For the coherent state preparation, the $\hat{H}_{\mathrm{ee}}$ Hamiltonian (equation 2.89) takes the form

$$\hat{H}_{\mathrm{ee,CS}} = \hbar\Omega\,(\hat{a}\, - \alpha\,\mathbb{1}_m\,)\,\hat{\sigma}_+ \,+ \mathrm{h.c.}. \tag{5.1}$$

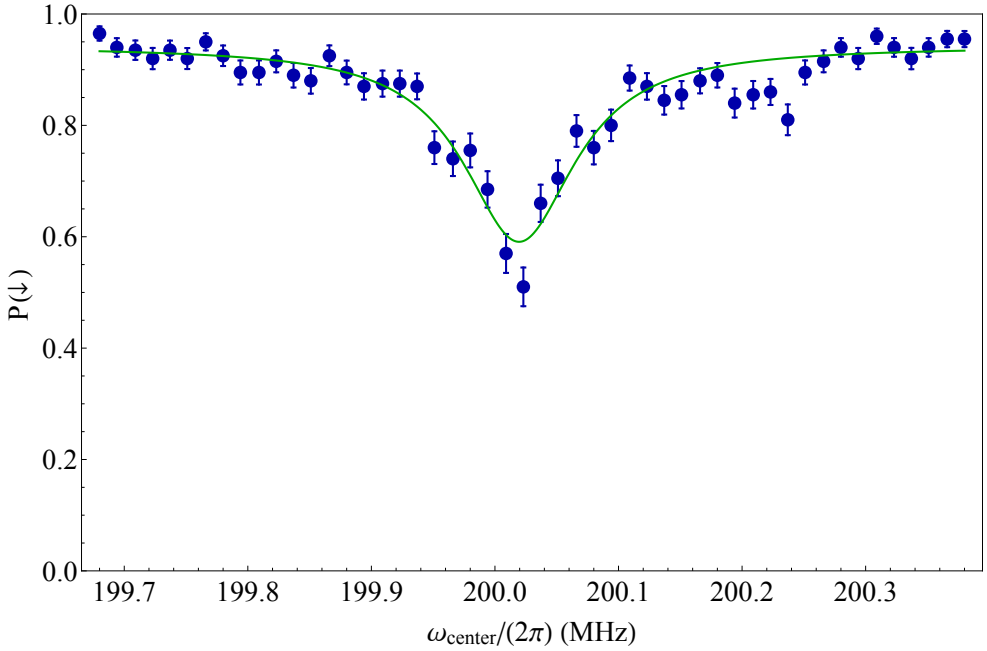

Figure 5.2: Calibration scan of the center frequency ω_{center} for pumping into a displaced squeezed state. A clear resonance is visible for the correct frequency value. The fit with a Lorentzian function yields a linewidth (FWHM) of 110(10) kHz.

This involves simultaneously applying two laser fields, one which resonantly drives the carrier transition $|\downarrow\rangle|n\rangle \leftrightarrow |\uparrow\rangle|n\rangle$ and another which resonantly drives the red motional sideband transition $|\downarrow\rangle|n\rangle \leftrightarrow |\uparrow\rangle|n-1\rangle$. The Rabi frequencies for these transitions are connected to the coherent state as $|\alpha| = \Omega_{\text{car}}/\Omega_{\text{rsb}}$ and $\arg(\alpha) = \varphi_{\text{car}} - \varphi_{\text{rsb}} + \pi$.
For all experiments involving the coherent state preparation, the multiple frequency components were generated by splitting the light into two paths and sending it through two double-passed AOMs. These two paths were then combined on a polarizing beamsplitter before coupling into a single mode fibre which delivers the light to the trap. This setup is also described in section and 3.4.1 and depicted in figure 3.31, labeled as '729 nm AOM setup 1'.

Squeezed State

For the squeezed state preparation, the $\hat{H}_{\text{ee}}$ Hamiltonian (equation 2.89) takes the form

$$\hat{H}_{\text{ee,SS}} = \hbar\,\Omega\left(\cosh(r)\;\hat{a} + e^{i\Theta}\sinh(r)\;\hat{a}^{\dagger}\right)\hat{\sigma}_{+} + \text{h.c.}, \tag{5.2}$$

This involves simultaneously applying two laser fields, one which resonantly drives the red motional sideband transition $|\downarrow\rangle|n\rangle \leftrightarrow |\uparrow\rangle|n-1\rangle$ and a second

driving the blue motional sideband $|\downarrow\rangle |n\rangle \leftrightarrow |\uparrow\rangle |n+1\rangle$. The Rabi frequencies for these transitions are connected to the desired squeezed state as $\Omega \cosh(r) = \Omega_{\mathrm{rsb}}$, $\Omega \sinh(r) = \Omega_{\mathrm{bsb}}$ and $\Theta = \varphi_{\mathrm{bsb}} - \varphi_{\mathrm{rsb}}$. For all experiments involving squeezed states the AOM setup needed to be changed from '729 nm AOM setup 1' used for the coherent state. As discussed in section 3.4.1, in this setup an interferometer exists between the AOMs producing the frequency components of the red and blue sidebands. Fluctuating path length of the interferometer leads to a fluctuation of the relative phase of the two frequency components. As this phase defines the phase of the squeezed state, a fluctuation of the phase, leads to a badly defined phase of the squeezed state, influencing the squeezed state fidelity. This is a consequence of the increased sensitivity of a squeezed state to phase fluctuations. Thus the '729 nm AOM setup 2' was used (see section 3.4.1 and figure 3.31) for the preparation of squeezed states. This setup uses a single-pass AOM with multiple rf frequencies send to it to produce the multiple laser frequencies needed.

Displaced-Squeezed State

For the displaced-squeezed state preparation, the $\hat{H}_{\mathrm{ee}}$ Hamiltonian (equation 2.89) gives already the final form

$$\hat{H}_{\mathrm{ee,DSS}} = \hbar\,\Omega \left(\cosh(r)\ \hat{a} + e^{i\Theta} \sinh(r)\ \hat{a}^{\dagger} - \alpha \right) \hat{\sigma}_{+} + \mathrm{h.c.}. \tag{5.3}$$

It combines the two Hamiltonians for the coherent and the squeezed state with the definitions $\Omega \cosh(r) = \Omega_{\mathrm{rsb}}$, $\Omega \sinh(r) = \Omega_{\mathrm{bsb}}$, $\Theta = \varphi_{\mathrm{bsb}} - \varphi_{\mathrm{rsb}}$, $\arg(\alpha) = \varphi_{\mathrm{car}} - \varphi_{\mathrm{rsb}} + \pi$, and $|\alpha| = \cosh(r)\Omega_{\mathrm{car}}/\Omega_{\mathrm{rsb}}$. As for the squeezed state, for the displaced-squeezed state the '729 nm AOM setup 2' was used as the fluctuating phase would harm the squeezing part of this state in the same way as for the squeezed vacuum state and additionally lead to a fluctuation phase between the squeezing and the displacement, which would result in fluctuations of the energy eigenstate populations (see section and 3.4.1 figure 3.31).

5.1.2 Optical Pumping

The optical pumping is done with a combined pulse of the 854 nm, 866 nm and 397 nm lasers. The 854 nm laser repumps the population from the $D_{5/2}$ level and the 866 nm combined with the sigma polarised component of the 397 nm laser repump the ion into the spin-down state as described in section 4.3.2. With the continuous pumping technique the power of the 854 nm laser had to be optimized and subsequently actively stabilized. The power optimization was done by monitoring the speed of the pumping into the desired state and its final fidelity, where both too high and too low powers had deteriorative effect on both monitored values. As a strong Stark shift is introduced by the 854 nm laser onto the $D_{5/2}$ level, the 729 nm frequency ω_{car} had to be recalibrated for

(a) Coherent state, pulsed method. (b) Squeezed state, continuous method.

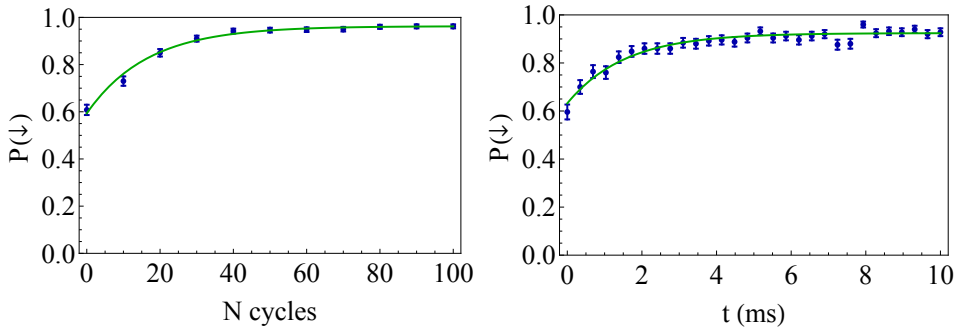

Figure 5.3: Pumping into the dark state probed with the $\hat{H}_-$ Hamiltonian.

each 854 nm laser power setting. In order to counter long term drifts of the 854 nm laser power and the connected change of the shift of ω_{car} the power was actively stabilized with the signal from a photo diode motoring a picked-off beam close to the trap.

5.2 Analysis of Prepared States

5.2.1 Steady/Dark state

In this first diagnosis of the created states we test if a steady state is reached after the dissipative state preparation and if it approximates a dark state. For this we follow the usual sequence of first pre-cooling then Doppler-cooling the ion. Then the dissipative state preparation is performed for a given duration. Subsequently the spin is repumped to $|\downarrow\rangle$ followed by the application of the $\hat{H}_-$ Hamiltonian[1] for a fixed time. Finally the spin state is read out. In the ideal case the $\hat{H}_-$ Hamiltonian would not excite the spin at all after the steady state is reached. Data for a coherent and a squeezed state is shown in figure 5.3. The state approaches a steady state which approximates a dark state of the pumping Hamiltonian. This shows that a state close to $|0\rangle_{\hat{U}}$ was created but does not characterize the state in an independent way.

5.2.2 Energy Eigenstate Analysis

In this separate analysis the populations of the energy eigenstates [MMK+96] of motion are determined. The state is again prepared by the sequential application of pre-cooling, Doppler-cooling, dissipative state preparation, spin

[1] This is the same Hamiltonian as the $\hat{H}_{\text{ee}}$ Hamiltonian used for the preparation of the state. But when the continuous method is used their center frequency is different, due to the Stark shift of the 854 nm laser on the $D_{5/2}$ levels.

repumping. This is followed by the application of a blue sideband Hamiltonian

$$\hat{H}_{\mathrm{bsb}} = \hbar\,\Omega_{\mathrm{bsb}}\hat{a}^{\dagger}\,\hat{\sigma}_{+} + \mathrm{h.c.} \tag{5.4}$$

for a certain time. As introduced in section 2.4, in the Lamb-Dicke regime the $\hat{a}^{\dagger}$ operator scales with the motional state $|n\rangle$ as $\langle n-1|\,\hat{a}\,|n\rangle = \sqrt{n}$. This allows to extract the populations $p(n)$ from the spin evolution under $\hat{H}_{\mathrm{bsb}}$. The population of the spin down state $|\downarrow\rangle$ as a function of the blue sideband pulse duration t is given by

$$P(\downarrow) = \frac{1}{2}\sum_{n} p(n)(1 + e^{-\gamma_n t}\cos(\Omega_{n,n+1}t)), \tag{5.5}$$

where $p(n)$ is the probability for finding the oscillator in the nth energy eigenstate and $\Omega_{n,n+1}$ is the Rabi frequency for the transition between the $|\downarrow\rangle\,|n\rangle$ and $|\uparrow\rangle\,|n+1\rangle$ states. The phenomenological decay parameter γ_n accounts for decoherence and fluctuations in the applied laser intensities [MMK+96]. By fitting a form similar to equation 5.5 to each set of data the probability distribution $p(n)$ is obtained. Then $p(n)$ is fitted using the theoretical form of the probability distributions for coherent, squeezed and displaced-squeezed states [Yue76]. The data and fits are shown in figures 5.4 (coherent state), 5.5 (squeezed state) and 5.6 (displaced squeezed state). The deduced populations with fits to the distributions are shown in figure 5.7. The fit for the coherent state yields a coherent state parameter $|\alpha| = 2.00(1)$. For the squeezed state we obtain a squeezing amplitude $r = 1.45(3)$, which for a pure state would correspond to a 12.6(3) dB reduction in the squeezed quadrature variance. For the displaced-squeezed state fitted parameters of $r = 0.63(6)$, $|\alpha| = 2.2(2)$ and $\arg(\alpha) - \varphi_s/2 = 0.42(6)$ rad are obtained. The details of the fitting are described in section 5.2.4. The blue sideband method verifies the size of the state most accurately but does not allow to measure the fidelity of the states, since it does not verify the phase coherence of the superposition states. It is also difficult to obtain good population estimates for states with a large spread in their Fock state occupancies. These shortcomings are addressed with a new type of measurement described in the section 5.2.3.

5.2.3 Analysis in the Engineered Basis

A new type of measurement, inspired by the technique of the reservoir engineering, was developed. It is based on the generalization of Fock state ladders, described in section 2.5.3. The Hamiltonian

$$\hat{H}_{+} = \hbar\Omega\left(\hat{K}^{\dagger}\,\hat{\sigma}_{+} + Kh\hat{\sigma}_{-}\right) \tag{5.6}$$

may be used to produce a fidelity measure for the desired motional state $|0\rangle_{\hat{U}}$ which obeys $\hat{K}\,|0\rangle_{\hat{U}} = 0$. Applying the Hamiltonian to $|0\rangle_{\hat{U}}\,|\downarrow\rangle$ results ideally

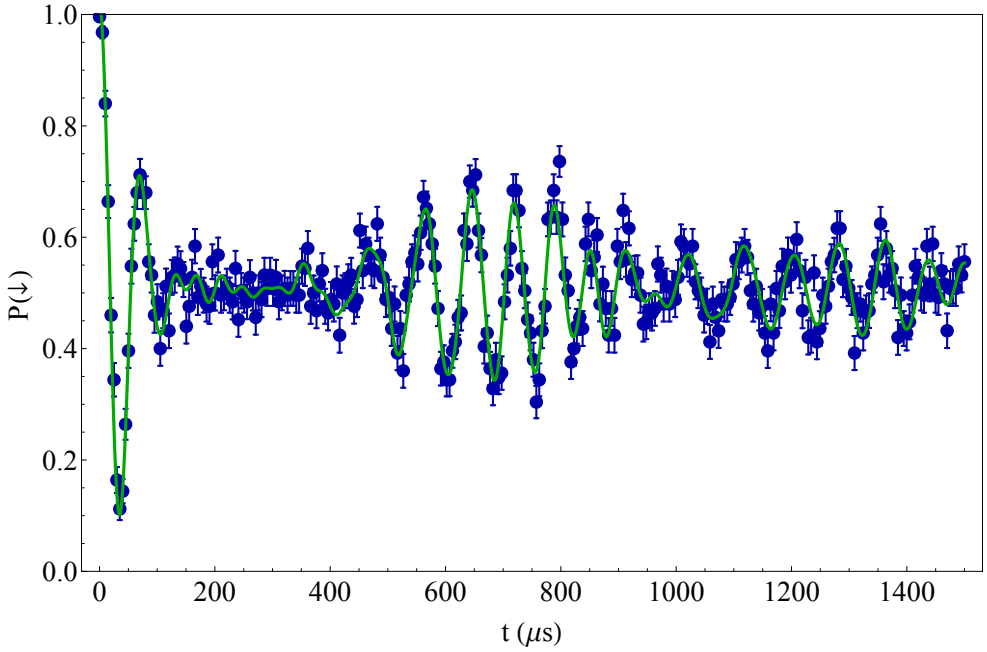

Figure 5.4: Blue sideband flopping data for a coherent state, fitted with an equation similar to 5.5.

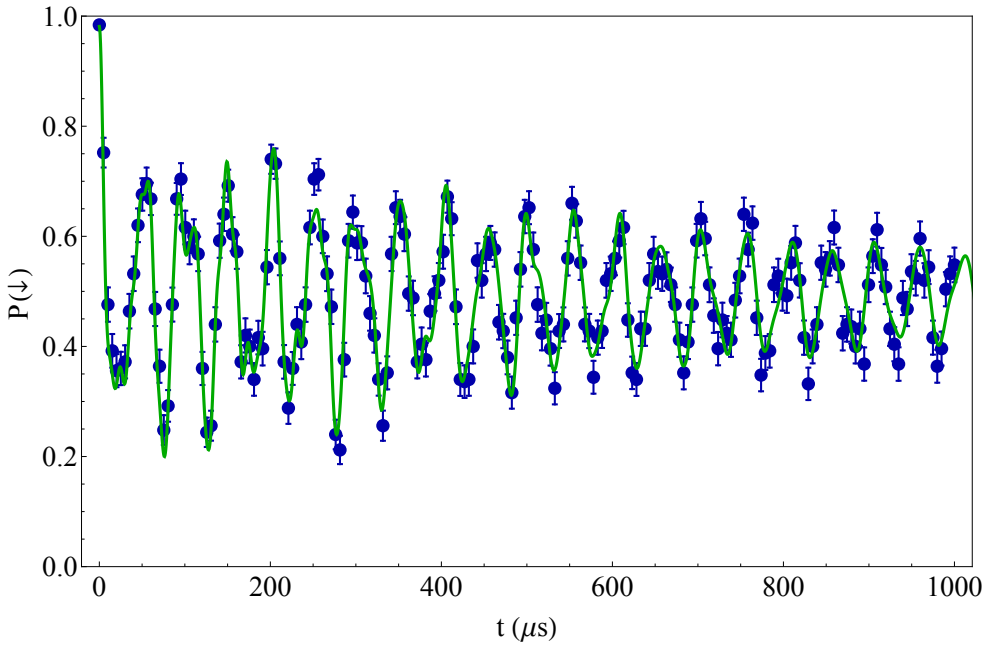

Figure 5.5: Blue sideband flopping data for a squeezed state, fitted with an equation similar to 5.5.

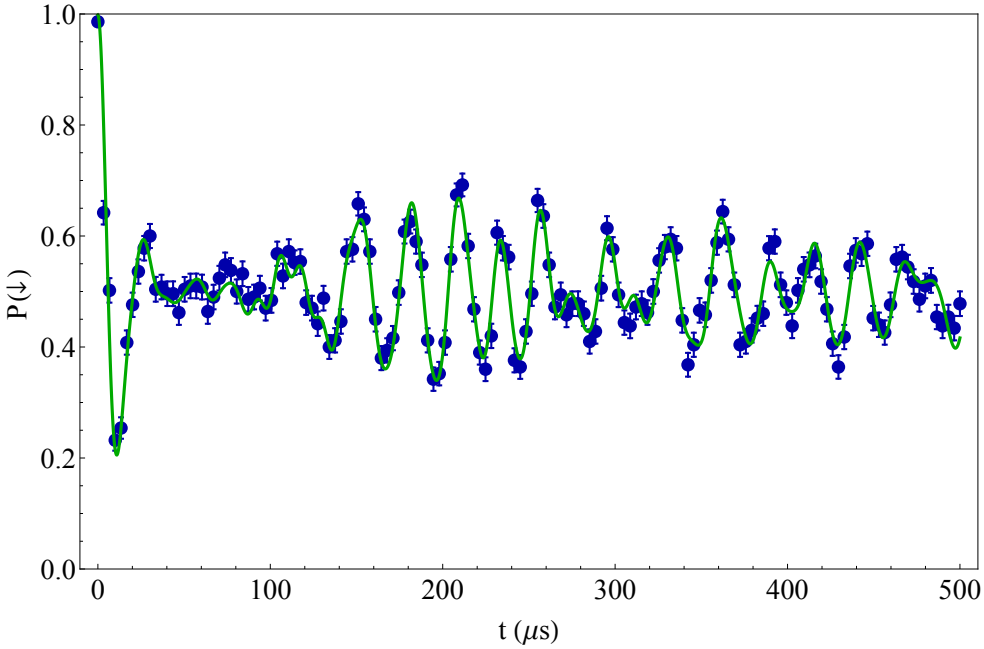

Figure 5.6: Blue sideband flopping data for a displaced-squeezed state, fitted with an equation similar to 5.5.

in single frequency Rabi oscillations, which is analogous to applying the anti-Jaynes-Cummings Hamiltonian to the motional ground state $|0\rangle|\downarrow\rangle$. For the non-ideal case the contrast and frequency decomposition of these oscillations can then be used to give a lower bound on the fidelity. As $\hat{K}$ is also used in the dissipative state preparation it obvious that it contains the phase information of the state and may now be used to verify that the probed superposition of energy eigenstates has the desired phase relationship.
A motional state tomography is more general, as any state may be analysed and the full state is characterised. With this projection onto the ground state of the engineered basis only that component is analysed. The clear advantage of our new method is a high signal to noise level achieved in the comparably short measurement time. The experiment is carried out by first preparing the desired state with the sequential application of pre-cooling, Doppler-cooling, dissipative state preparation, spin repumping. Following this the $\hat{H}_+$ Hamiltonian is applied for a given time, after which the spin state is read out. The new method was used to analyse the prepared coherent and squeezed states. The Rabi flop data was fitted in the same way as the blue sideband data, resulting in a population distribution in the engineered basis $p_{\hat{U}}(n)$ From this the fidelity is inferred, which corresponds to $p_{\hat{U}}(0)$. The data and fits are shown in figures 5.8 and 5.9. The extracted populations and fits are shown in figure 5.10 resulting in fidelities of 0.90(2) and 0.88(2) for the coherent and squeezed states respectively. These are lower bounds on the fidelity as these numbers in-

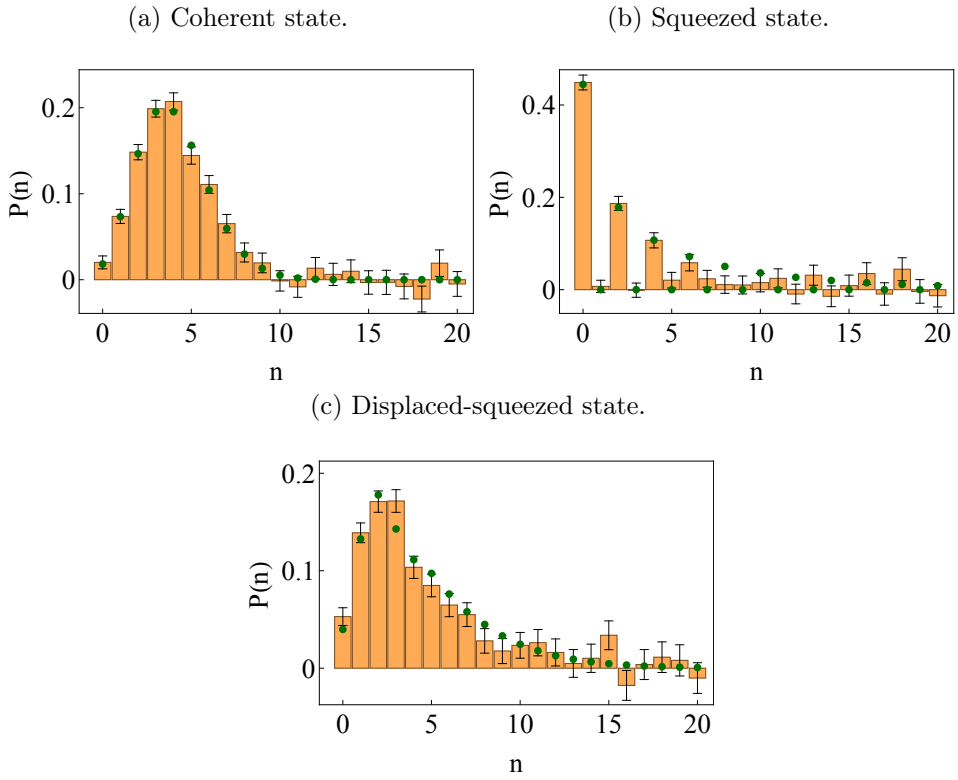

Figure 5.7: Populations deduced from the blue sideband flopping shown in figures 5.4, 5.5 and 5.6 for the (a) coherent, (b) squeezed and (c) displaced-squeezed state. The green dots show the populations for the fitted states.

clude errors in the analysis pulse in addition to state-preparation errors. This is the first fidelity measure for squeezed motional states of trapped ions.
The Rabi frequencies for implementation of the used Hamiltonian are given by $\Omega_{\mathrm{c}}/\Omega_{\mathrm{bs}b} = -\alpha^*/\cosh(r)$ and $\Omega_{\mathrm{r}sb}/\Omega_{\mathrm{bs}b} = e^{-i\varphi_{\mathrm{s}}}\tanh(r)$.
Similar to a traditional blue sideband/red-sideband measurements also the $\hat{H}_-$ Hamiltonian was applied over time (replacing the $\hat{H}_+$ Hamiltonian in the above sequence). This is in principle the same measurement as described in section 5.2.1, only here the duration of the analysis pulse applied is scanned instead of the state preparation duration. The results given in figure 5.11 show a dark state, slowly decaying, with no clear oscillatory pattern.

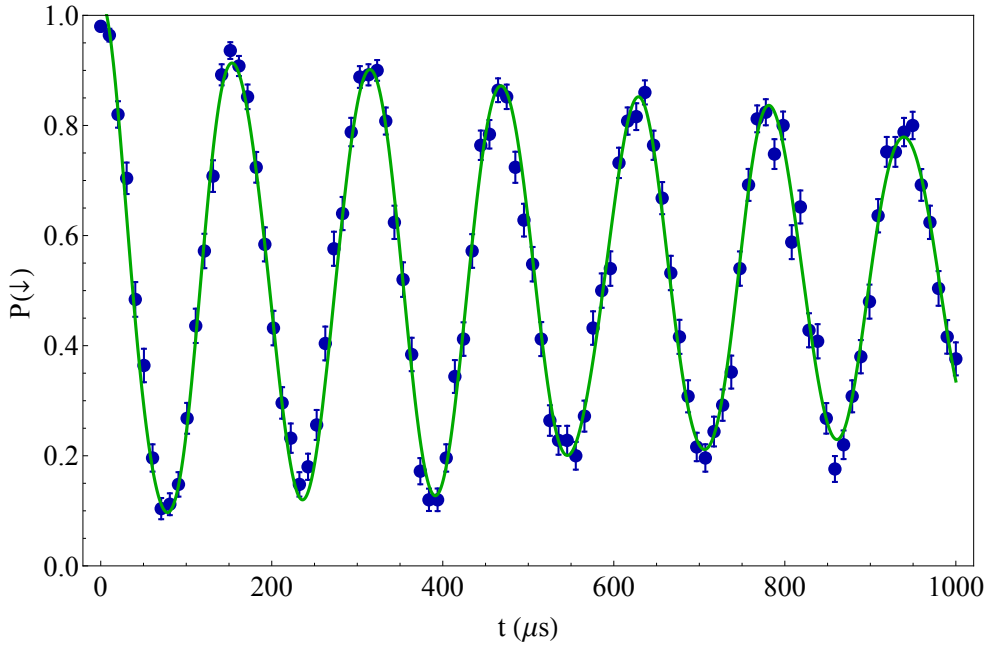

Figure 5.8: Application of the $\hat{H}_+$ Hamiltonian to the coherent state. Clear single frequency Rabi oscillations are visible.

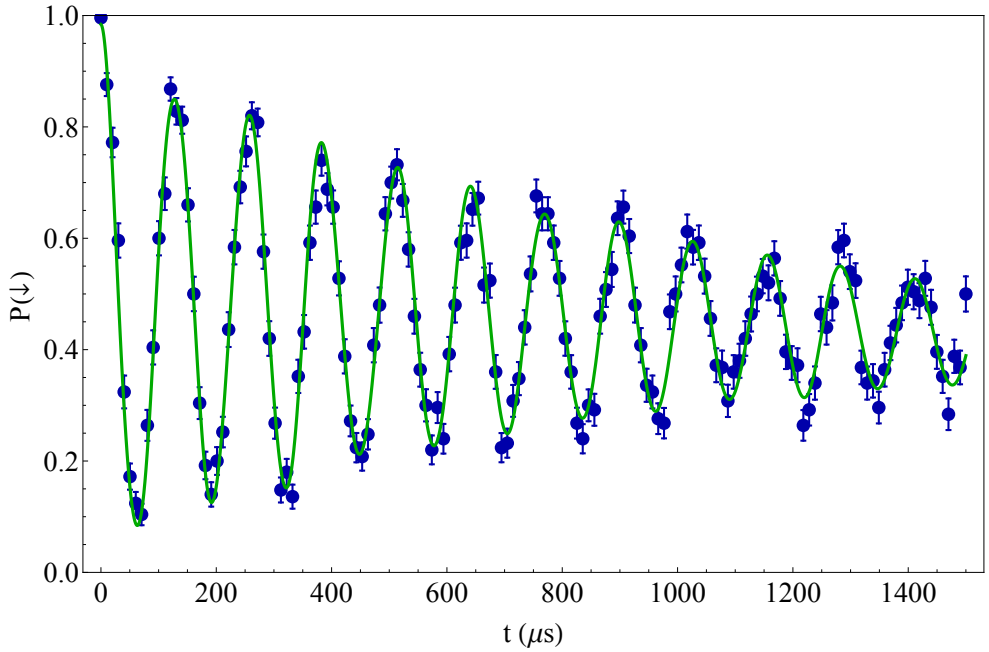

Figure 5.9: Application of the $\hat{H}_+$ Hamiltonian to the squeezed state. Clear single frequency Rabi oscillations are visible.

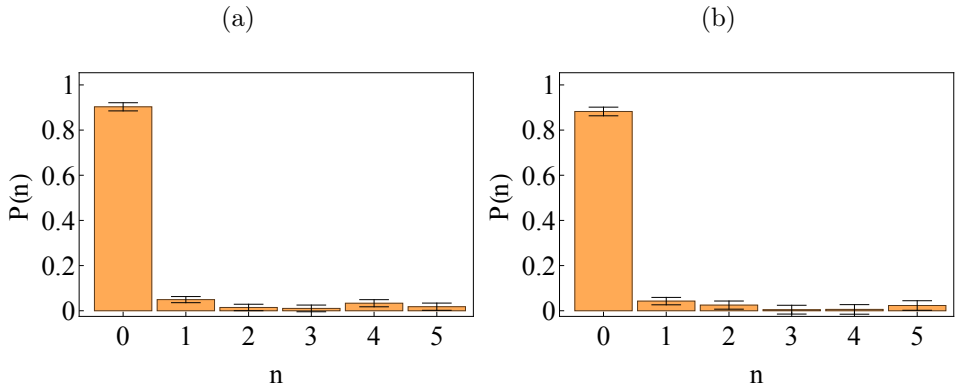

Figure 5.10: Populations deduced from the Rabi oscillation data shown in figures 5.8 and 5.9 for the (a) coherent and (b) squeezed state.

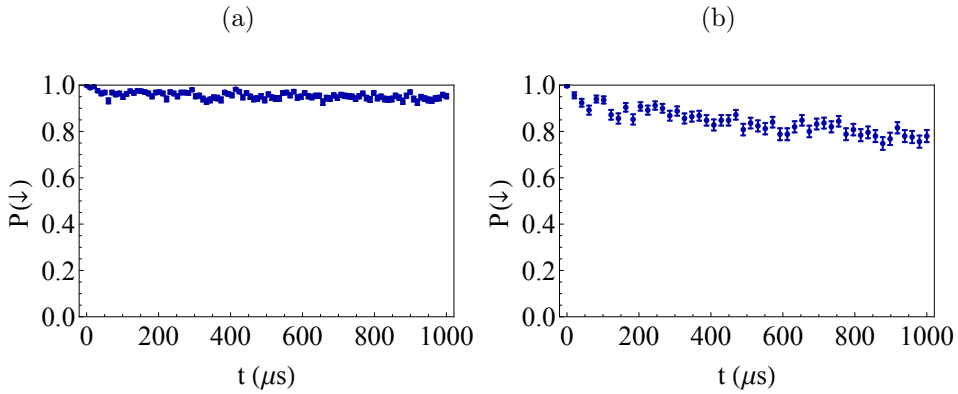

Figure 5.11: Application of the $\hat{H}_-$ Hamiltonian for the (a) coherent, (b) squeezed state.

5.2.4 Fits to Rabi oscillation data

To extract the populations $p(n)$ of the Fock states, fits to the data were performed using a fitting function of the form

$$P(\downarrow, t) = b\,t + \frac{1}{2}\sum_{n=0}^{n_{\max}} p(n)\ \left(1 + \ e^{-\gamma\sqrt{n+1}t}\cos\left(\Omega_{n,n+1}\,t\right)\right) \tag{5.7}$$

where $\Omega_{n,n+1} = \Omega_{\mathrm{R}} f(n,\eta)$ is the state-dependent Rabi frequency. Ω_{R} is a constant proportional to the square root of the laser intensity. We use a scaling function $f(n,\eta) = e^{-\eta^2/2}(1/(n+1))^{1/2}\eta L_n^1(\eta^2)$ which is known to be correct when driving the blue sideband. At low n, $f(n,\eta) \propto \sqrt{n+1}$, both for the blue sideband and for the $\hat{H}_+$ Hamiltonian. For higher values of n it is expected that the explicit form of $f(n,\eta)$ would be different for the blue sideband and $\hat{H}_+$. In the latter case, populations with $n > 0$ are not observed in the experiments.

The parameter b in the first term on the right hand side of equation 5.7 accounts for a gradual pumping of population into the state which is not involved in the dynamics of the probe Hamiltonian [DFV00]. This occurs due to the frequency noise components from the servo bumps described in section 3.4.1 which are close to resonance with the carrier transition. This pumping predominantly occurs as a direct spin flip with no effect on the motion. Thus the effect is largest when the population of the motional ground state of the basis relevant to the probe Hamiltonian is large. This is most significant for the data shown in figure 5.9, where it gives a 5% effect over the 1 ms duration of the Rabi oscillations. For the data shown in figure 5.8, this is a smaller effect, and b is fixed to zero for fitting.
Once $p(n)$ is extracted from the data, these populations are fitted with the theoretical probability distributions obtained from the general form for a displaced-squeezed state [Yue76]

$$p_{\mathrm{d}s}\left(n, r, \varphi_{\mathrm{s}}, \alpha\right) = \frac{(\tanh(r)/2)^n}{n!\cosh(r)} e^{-|\alpha|^2+|\alpha|^2\tanh(r)\cos(2\arg(\alpha)-\varphi_{\mathrm{s}})} \times \\ \times \left| H_n\left(\frac{|\alpha| e^{i(\arg(\alpha)-\varphi_{\mathrm{s}}/2)}}{\sqrt{\sinh(2r)}}\right)\right|^2 \tag{5.8}$$

where $H_n(x)$ is a Hermite polynomial, $\alpha = |\alpha|\, e^{i\arg(\alpha)}$ and $\xi = re^{i\varphi_{\mathrm{s}}}$. For the coherent state generation the limit of this expression is used as $r \to 0$, resulting in the Poisson distribution

$$p_{\mathrm{c}}(n, |\alpha|) = \frac{e^{-|\alpha|^2}|\alpha|^{2n}}{n!} \ . \tag{5.9}$$

For the squeezed vacuum state $|\alpha| = 0$ is used, giving the probability distribution

$$p_{\mathrm{s}}(n, r) = \begin{cases} \frac{(\tanh(r)/2)^n n!}{((n/2)!)^2\cosh(r)} & \text{for } n \text{ even} \\ 0 & \text{for } n \text{ odd.} \end{cases} \tag{5.10}$$

5.2.5 Limits to the Squeezed State Size

Data with a higher squeezing parameter was taken, but displaying only poor fidelities in the analysis. Example data for a squeezed state with $r = 1.41.49(7)$ and a fidelity of $F = 0.69(2)$ is shown in figures 5.12 and 5.13. Noticeable is the low contrast of the $\hat{H}_+$ analysis, indicating a low fidelity. To explain the drop in fidelity the following sections discuss several, potential harmful effects.

Validity and Limits of the Lamb-Dicke Approximation The validity of the Lamb-Dicke approximation presents a fundamental limit on the size of squeezed states which can be reached using reservoir engineering. It is possible to estimate the largest state which can be produced with high fidelity by

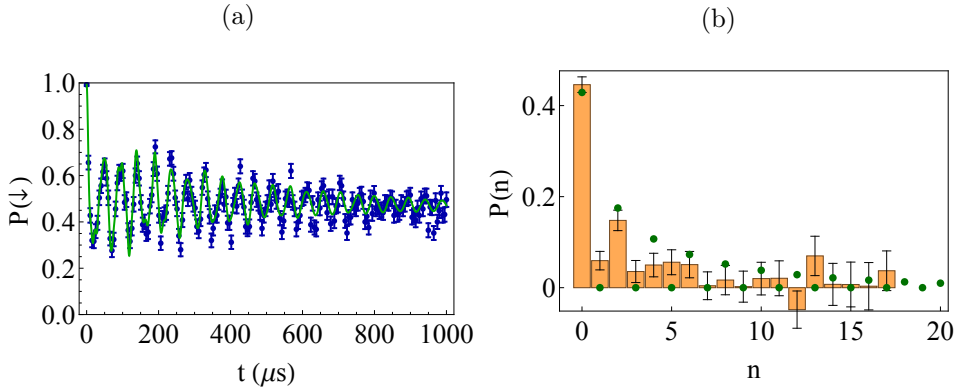

Figure 5.12: Blue sideband flopping with fit (a) and extracted populations (b). The fit results in a squeezed state size of $r = 1.49(7)$.

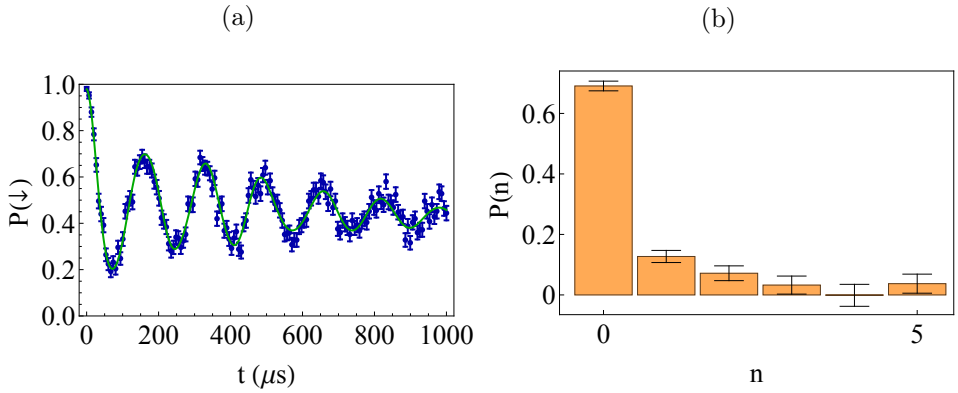

Figure 5.13: Analysis of a large squeezed state ($r = 1.49(7)$) in the engineered basis (a) with the extracted populations (b) yielding a fidelity of 0.69(2).

looking at the dark state of the resonant terms in the Hamiltonian produced in the laboratory (corresponding to $\hat{H}_-$), which is given by

$$\hat{H}_{\text{lab}} = \hbar\Omega_{n,n+1}\sinh(r)\,|n\rangle\langle n+1| \tag{5.11}$$
$$+\,\hbar\Omega_{n,n-1}\cosh(r)\,|n\rangle\langle n-1| + \text{h.c.} \tag{5.12}$$

with $\Omega_{n,n+1} = \Omega_{0,0}(1/(n+1))^{1/2}\eta L_n^1(\eta^2)$ where $L_n^\alpha(x)$ is the generalized Laguerre polynomial in x [WMI+98]. For the Lamb-Dicke parameter of the experiments ($\eta = 0.05$) the dark state fidelity with the desired squeezed state drops below 0.95 for $r = 2.9$, which is well above the regime accessed in our experiments. Population starts to accumulate in the vicinity of the Fock state for which $\Omega_{n,n+1}$ is close to or equal to zero – this means that although the theoretical fidelity is 0.95 there is already a significant increase in the variance of the squeezed quadrature compared to what would be expected for an ideal squeezed vacuum state. The maximum reduction in the squeezed vari-

ance achievable with this value of the Lamb-Dicke parameter is 21 dB. It is interesting to note that the squeezed state being dark is due to the ratio of the neighbouring sideband matrix elements $\Omega_{n,n+1}/\Omega_{n,n-1}$. Though this is strictly valid only in the Lamb-Dicke regime, it is also well approximated for significant deviations from the Lamb-Dicke $\sqrt{n}$ scaling of the matrix elements, meaning that the state still closely approximates the desired squeezed state.
The Lamb-Dicke approximation is also implicit in the assumption that the photons scattered during the internal state repumping do not induce significant changes to the motional state. This reduces the pumping rate, since it adds a diffusion process, but it does not affect the dark state in the absence of other heating mechanisms (the scattering stops once the system attains the dark state). In practice, off-resonant driving of the carrier transition results in residual internal state excitation even if the motion is in the nominal dark state. This means that the recoil due to scattering can degrade the motional steady-state fidelity. For the scattering, the relevant Lamb-Dicke parameter is that for the scattered photons, which have wavelengths of 393 nm, 397 nm and 854 nm. The higher momentum of the ultra-violet photons would be expected to introduce more problems, and an average of 3 ultraviolet photons are scattered during repumping for our setup. To gauge the influence which both effects have, J. Home has performed Monte-Carlo wavefunction simulations which include off-resonant driving of the carrier transition, and in which the momentum kick during relaxation is included using a Lindblad operator $\hat{L} = \hat{\sigma}_- e^{\chi i \eta_{393}(\hat{a}^\dagger + \hat{a})}$. Values of $\chi > 1$ were used to account for the multiple scattering events. Fidelities of 0.95 ± 1 are obtained for a squeezed state with $r = 1.38$ in the deliberately chosen extreme case where $\chi = 3$, which is similar to assuming that all 9 photons involved in the repumping pulse displace the ion in the same direction, and where this is taken to be along the oscillator axis. This most likely overestimates the effect of the recoil. Nevertheless, this fidelity is higher than that we observe in the experiment.

Motional Heating and Dephasing The rate at which a squeezed state loses overlap with itself due to fluctuating electric fields at the ion is related to the heating rate from the ground state $\Gamma_{0\to1}$ by $\Gamma_{\mathrm{sq}} = \Gamma_{0\to1}\cosh(2r)/2$ [ALKH13]. For the observed heating rate from the motional ground state of $\Gamma_{0\to1} = 10 \pm 1$ quanta s^{-1} (see section 4.6) this results in a rate of 46 quanta s^{-1} for a squeezed state with $r = 1.45$. This is slower than the timescale of decoherence observed in both the $\hat{H}_-$ and $\hat{H}_+$ data presented in section 5.2.3. Including this into the Monte-Carlo simulations using Lindblad operators $\sqrt{\Gamma_{0\to1}}\hat{a}$ and $\sqrt{\Gamma_{0\to1}}\hat{a}^\dagger$ verifies this observation.
As the motional dephasing was measured (see section 4.7) to be higher than what is expected for the measured heating rate an additional dephasing was included in the simulations with a Lindblad operator $\sqrt{\Gamma_{\mathrm{dephase}}}\hat{a}^\dagger\,\hat{a}$, where the additional dephasing is estimated from $\Gamma_{\mathrm{dephase}} = 1/(32\,\mathrm{ms}) - 2\Gamma_{0\to1}$. In simu-

lations of the $\hat{H}_+$ and $\hat{H}_-$ evolutions the loss of contrast is faster than what we observe experimentally for the squeezed state. We thus conclude that dephasing is likely to be a major factor in the decay of oscillations observed in the data. The assumption of Markovian dephasing, which enters through the use of the Lindblad operator approach may not correctly describe our experiment; the real scaling between decoherence rates for the two-state superposition and the squeezed state will depend on the characteristics of the noise which is causing this effect. We have not yet tracked this down.

Magnetic Field and Laser Intensity Fluctuations Magnetic field and intensity fluctuations were simulated by randomizing the Rabi frequencies and detuning for single runs of the simulation, finally averaging over all results. These noise components are mainly common mode for the two frequency components of the 729 nm laser and were simulated as such. As expected the fluctuations have no major effect on the preparation process, which is robust against common mode noise. The dynamics of the analysis pulse show influence, adding to the motional dephasing. They do however, not explain the low starting contrast of the Rabi-flopping shown in figure 5.13.

Extension of the Simulation to a Three Level System For simulations a two level system was used with the optical pumping implemented as direct decay from the spin-up to the spin-down level. The experimental situation though is better described by a three level system, which separates the optical pumping with the 854 nm laser and emission of a 393 nm photon and the second optical pumping step with the 397 nm and 866 nm lasers under emission of 397 nm and 866 nm photons. The decay times measured in the experiment were compared to simulations confirming that the 854 nm rate was correctly optimized.
A simulation of the three level system together with the off-resonant carrier excitation and the recoil has not yet been performed.

5.2.6 Squeezed States - Further Discussion

Dissipative Pumping Rate - Continuous Pumping

As can be seen from the Master equation 2.74 for the dissipative state preparation derived in section 2.4.2 the rate of the pumping is given by $\Gamma_{\mathrm{DSP}} = 2\Omega^2/\Gamma$. For the squeezed state, the dissipative pumping slows down as the size of squeezed state prepared is increased. The relation between the blue and red sideband Rabi frequencies and the Rabi frequency which is relevant to the pumping rate Γ_m for the squeezed state can be seen from

$$\begin{aligned}\hat{H}_{\mathrm{sq}} &= \hbar\Omega\cosh(r)\left(\hat{a}^\dagger + \tanh(r)e^{i\varphi_{\mathrm{s}}}\hat{a}\right)\hat{\sigma}_+ + \mathrm{h.c.} \\ &= \hbar\left(\Omega_{\mathrm{bsb}}e^{i\varphi_{\mathrm{bsb}}}\hat{a}^\dagger + \Omega_{\mathrm{rsb}}e^{i\varphi_{\mathrm{rsb}}}\hat{a}\right)\hat{\sigma}_+ + \mathrm{h.c.}\ . \end{aligned} \tag{5.13}$$

Thus pumping rate scales as $\Gamma_{\mathrm{DSP}} \sim \Omega_{\mathrm{bsb}}^2 / \cosh^2(r)$.

Coherent Generation of Squeezed States

An alternative approach to generating squeezed states would be to prepare the ground state, and then subsequently to apply a suitable Hamiltonian for a fixed duration. The desired Hamiltonian is

$$\hat{H} = \frac{\hbar\Omega}{2}\left(\hat{a}^{\dagger\,2} + \hat{a}^{\,2}\right), \tag{5.14}$$

which should act only on the motional state. This will produce a squeezed state with squeezing amplitude r in a time of $t = r/\Omega$. In order to generate this Hamiltonian using the 729 nm laser, one possibility is to prepare an eigenstate of the spin $\hat{\sigma}_x$ operator, then drive both second motional sidebands simultaneously. This is a modification of the methods used for generating the displacement operators used in the two-qubit gate proposed by Sørensen and Mølmer [SM00]. The strength of the second sideband is given relative to that of the first sideband by η. For the experiments described in this chapter, typical values of first sideband Rabi frequencies are $\Omega_{\mathrm{b}sb}/(2\pi) = 20$ kHz, hence the Rabi frequency for the second sideband would be $\Omega/(2\pi) = 1$ kHz. Generating a squeezed state with $r = 1.45$ would therefore take 230 µs. The $\hat{H}_+$ oscillations displayed in figure 5.9 are at less than 80% of their initial amplitude over this timescale, which is lower than the fidelity observed in 5.2.3. This indicates that the dissipative pumping results in clear benefits over the coherent generation of squeezed states.

5.2.7 Analysis of the States using a Spin-State Dependent Force

Another diagnosis technique we applied to the squeezed state is a spin-state dependent force. In these experiments a bichromatic laser beam is used addressing both red and blue sidebands simultaneously on resonance. As shown below, this creates a force with its sign depending on the spin state of the ion in the x-basis. With a initial superposition state $|\uparrow_x, 0\rangle + |\downarrow_x, 0\rangle$ the resulting state after applying the state dependent force for a time t is a Schrödinger cat state $|\uparrow_x, \alpha(t)\rangle + |\downarrow_x, -\alpha(t)\rangle$. As the displacement α has a phase and the final measurement result is sensitive to the extent of the wave function, this can be used to analyse the quadratures along the squeezed state long and short axis. For this experiment the squeezed state is again prepared by the sequential application of pre-cooling, Doppler-cooling, dissipative state preparation, spin repumping. This is followed by the application of the the Hamiltonian for the state dependent force, followed by the spin readout. The Hamiltonian, expressed in the x-basis, is given by

$$\hat{H}_D = \hbar\Omega\hat{\sigma}_x\left(\hat{a}^\dagger\, e^{-i\varphi_D/2} + \hat{a}\, e^{i\varphi_D/2}\right), \tag{5.15}$$

with Ω the strength of the coupling, $\hat{\sigma}_x = (|\uparrow\rangle\langle\downarrow| + |\downarrow\rangle\langle\uparrow|)/\sqrt{2}$ and φ_D the relative phase of the blue and red sideband laser components used to implement the Hamiltonian. Applying the Hamiltonian for a time t results in the displacement $\alpha(t) = -i\Omega \exp(-i\varphi_D/2)t/2$. Applying this Hamiltonian to a squeezed state creates *squeezed Schrödinger cat states*.
Measuring the spin state in the z-basis results in $P(\downarrow) = (1 + X)/2$, where X is the magnitude of the overlap between the two displaced wavepackets, given by

$$X(\alpha(t), \xi) = \exp\left(-2|\alpha(t)|^2 \left(e^{2r}\cos^2(\Delta\varphi) + e^{-2r}\sin^2(\Delta\varphi)\right)\right) \tag{5.16}$$

with $\Delta\varphi = \arg(\alpha(t)) - \varphi_s/2$ and φ_s the phase of the squeezed state. Measurements of this overlap are presented in figure 5.14 for three experiments. The first creates standard Schrödinger cat states from the motional ground state. The drop of the spin down population is the signature for the wavepackets losing overlap. In the second and third experiment a squeezed state is used as initial state and the force is aligned along the long and short axis of the squeezed state respectively. This results in a slower (faster) drop off the spin down population compared to the ground state, which is a direct measure of the quadratures of the squeezed state, analysing this property very intuitively. More on this type of analysis and measurements of the final squeezed Schrödinger cat states can be found in [LKdC+15, Lo].

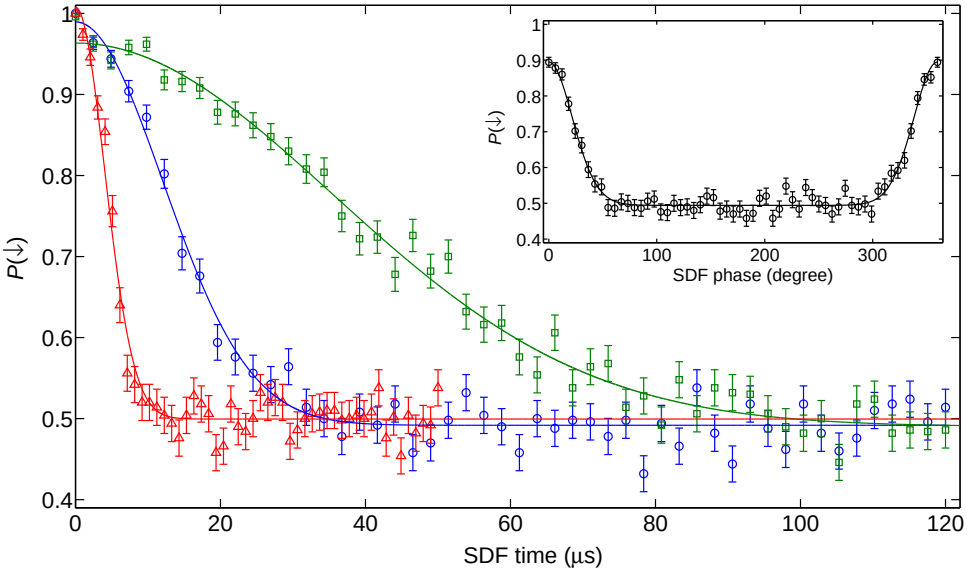

Figure 5.14: Data for the state dependent force analysis of a squeezed state with $r = 1.08(3)$. For the green data points the state dependent force was applied along the long axis of the squeezed state, for the red points along the short axis. For the blue data points the state dependent force was applied to a ground state for reference. The fits to the data confirm the squeezed state's amplitude measured by blue sideband flopping. In the inset data is shown for a fix duration (20 μs) of the state dependent force with its relative phase to the squeezed state scanned. 0° (360°) correspond to alignment of the long axis with the state dependent force, clearly showing the stable phase relationship between the state and the force applied. Image courtesy of H.-Y. Lo.

Chapter 6

Control in the Engineered Basis

This chapter is covering two experiments that use new spin-motion couplings devised from the dissipative state engineering. In section 5.2.3 they have been used to analyse the states created in their eigenbasis. Here the couplings are used to further manipulate a squeezed vacuum state, the ground states of the engineered basis. In section 6.1 excited squeezed number states are produced, walking up the state ladder in the engineered basis. In section 6.2 a superposition state of the squeezed vacuum state and the first excited squeezed number state is prepared.

6.1 Ladder states

Starting with the ground state of the engineered basis, excited states in the engineered basis can be created by application of $\hat{H}_+$ and $\hat{H}_-$ in turns for times which equal π times to transfer all population from $|n\rangle_{\hat{U}}$ to $|n+1\rangle_{\hat{U}}$, in detail:

$$\hat{U}_+(t = 2\pi/\Omega)\,|\downarrow, 0\rangle_{\hat{U}} = |\uparrow, 1\rangle_{\hat{U}} \tag{6.1}$$

$$\hat{U}_-(t = 2\pi/\Omega)\,|\uparrow, 1\rangle_{\hat{U}} = |\downarrow, 2\rangle_{\hat{U}} \tag{6.2}$$

$$\hat{U}_+(t = 2\pi/\Omega)\,|\downarrow, 2\rangle_{\hat{U}} = |\uparrow, 3\rangle_{\hat{U}} \tag{6.3}$$

etc.

with $\hat{U}_\pm(t) = \exp\left(-i\,t\,\hat{H}_\pm/\hbar\right)$. Every excited state created in this manner is analysed with a subsequent $\hat{H}_+$ (for even n states) or $\hat{H}_-$ (for odd n states) pulse for a given time followed by a measurement of the spin state. The experiment was performed by first preparing a squeezed state with the methods described in chapter 5, followed by pumping the spin to $|\downarrow\rangle$. Subsequently the necessary series of $\hat{H}_+$ and $\hat{H}_-$ pulses for a state $|n\rangle_{\hat{U}}$ is applied. Then, to analyse the state the $\hat{H}_+$ is applied for a given time if the state has even n. If the state has odd n the $\hat{H}_-$ Hamiltonian is applied instead. Finally the spin state is read out. The results for the final states $n = 0$ to 5 for a vacuum

squeezed state as starting state ($r = 1.2(1)$) are shown in figure 6.1.
The dependence of the Rabi frequencies on the n state was analysed. Figure 6.2 shows the fitted Rabi frequencies for all states. A fit to this data with the power laws

$$\Omega_n(\kappa) = \Omega_0\, n^\kappa \quad \text{and} \quad \Omega_n(\kappa) = \Omega_1\, (n-1)^\kappa \tag{6.4}$$

was performed with n the nth excited state, κ the scaling parameter and Ω_0 the Rabi frequency for the ground state and Ω_1 the Rabi frequency for the first excited state. The two different definitions of the power law are used for the $\hat{H}_+$ and $\hat{H}_-$ analysis pulse respectively as it was not possible to calibrate the base Rabi frequency Ω_0 for both to the same value. A global fit over the data with a common scaling parameter κ was performed, yielding $\kappa = 0.48(1)$, violating the scaling expected for the Lamb-Dicke regime of $\kappa = 1/2$.
The theoretical violation for the squeezed states is stronger than for the energy eigenstates as depicted in figure 6.2. This can be seen as a consequence of the squeezed state occupying higher energy eigenstates, even for low n in the engineered basis than the pure energy eigenstates do. The fitted value for κ confirms this tendency of the scaling, although it is not a good fit judging from the χ-squared test as the error bars on the data are extremely small. This might be an effect of the error bars of the single data point being underestimated as discussed in section 5.2.4. Also the data analysed with $\hat{H}_+$ shows an opposite behavior than the data analysed with $\hat{H}_-$, which might hint that the calibration issue is not resolved by using different Rabi frequencies. The mathematical construct for excited states in a transformed Fock basis were formulated in the 1990s (see e.g. [Wün91, Nie97]). To our knowledge this is the first time excited squeezed states are experimentally created and verified. Calculating the theoretical energy eigenstate populations of the states gives an insight into the intriguing nature of these operations. Figure 6.3 shows the energy eigenstate populations of the squeezed ground state and first excited squeezed number state. It is visible that the populations get transferred over up to 5 energy eigenstates within one spin flip, which would be impossible with a simple first blue sideband operation.

6.2 Superposition state

In a second experiment a superposition state of two Fock states in the engineered basis was created. The experiment was performed by first preparing a squeezed state with the methods described in chapter 5, followed by pumping

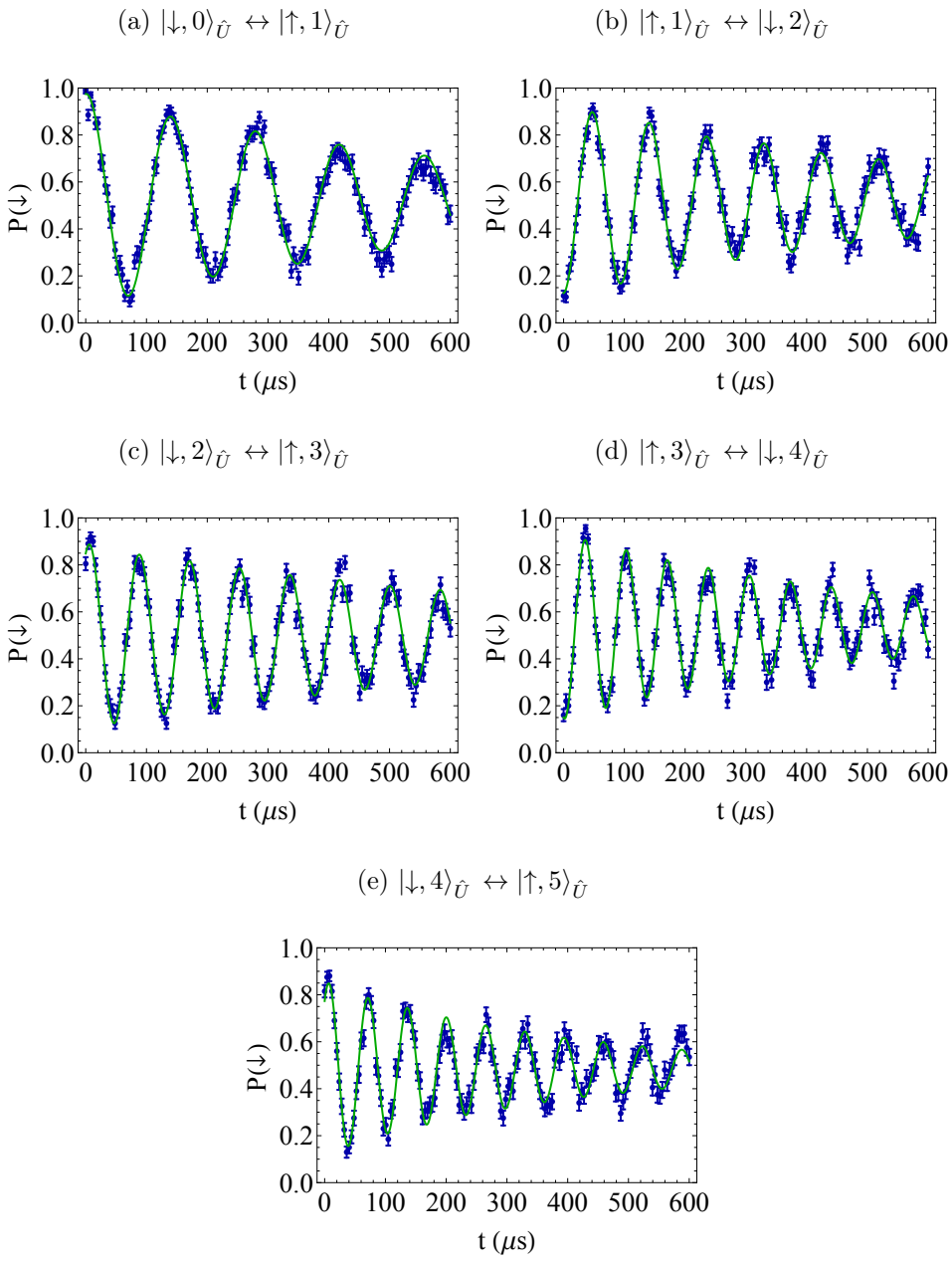

Figure 6.1: The plots show that data for the different excited squeezed states from (a) $n = 0$ to (e) $n = 4$. The Rabi frequencies obtained from the fits are $\Omega_{0,1} = 45.2(1)\,\mathrm{kHz}$, $\Omega_{1,2} = 66.6(1)\,\mathrm{kHz}$, $\Omega_{2,3} = 76.2(1)\,\mathrm{kHz}$, $\Omega_{3,4} = 93.1(1)\,\mathrm{kHz}$ and $\Omega_{4,5} = 97.3(1)\,\mathrm{kHz}$. The transfer of population is surprisingly good, the main population loss is in the first π-pulse.

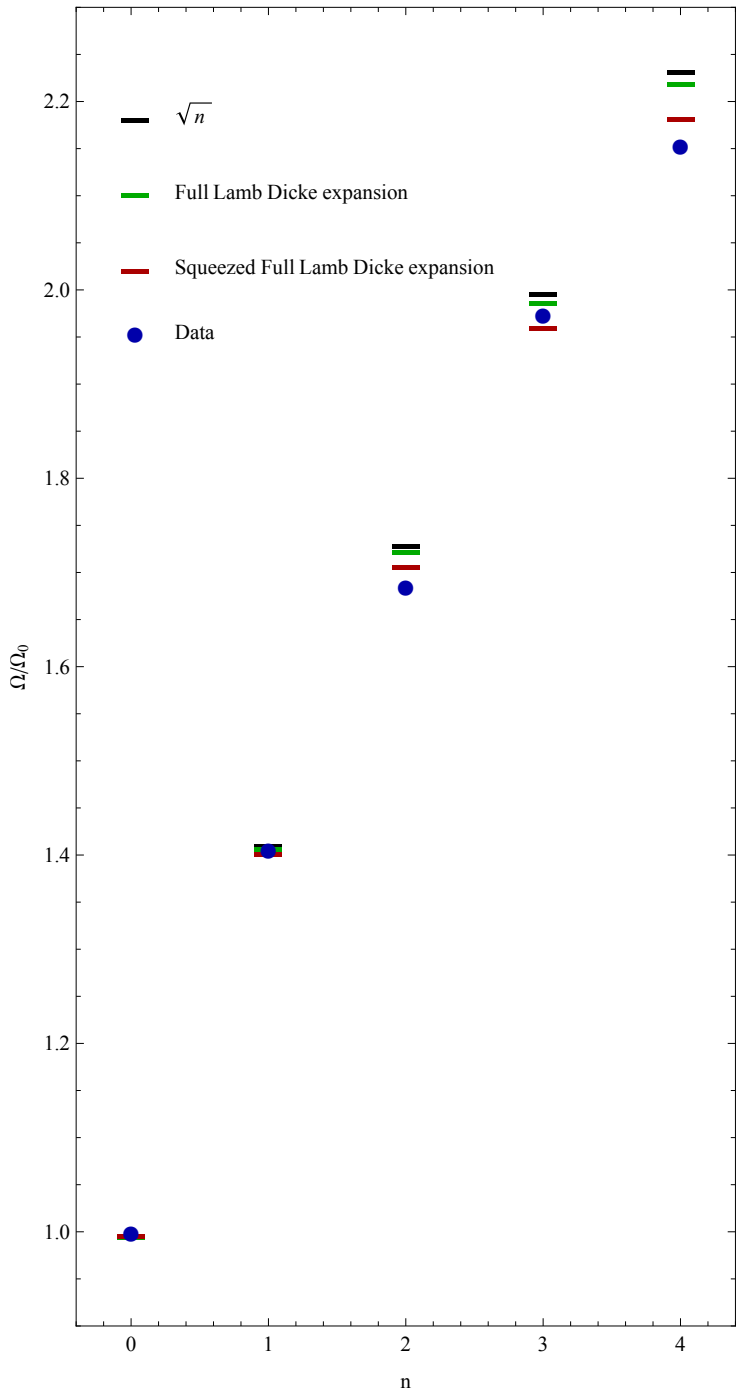

Figure 6.2: Analysis of the Rabi frequencies for the squeezed Fock states. The data for $n = 1$ and $n = 3$, analysed with $\hat{H}_-$ is scaled with the theoretical value for the full expansion of the squeezed Fock states for a better presentation and, as done in the analysis, by the Rabi frequency Ω_1 instead of Ω_0. The error bars of the data are of similar size as the data points.

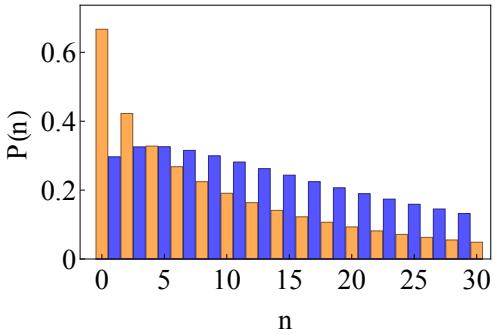

Figure 6.3: The plot shows the calculated populations of the squeezed ground state (orange) and first squeezed excited state (blue) in the energy eigenstate basis. The population of $n = 0$ for the squeezed ground state must be transferred to levels up to $n = 5$ to match the populations of the first excited squeezed number state. This happens within one spin-flip in the operations used to create the excited state, which is remarkable as no higher order sidebands are involved in this process.

the spin to $|\downarrow\rangle$. Subsequently the following operation was applied

$$\begin{aligned}\hat{U}_-(t = 2\pi/\Omega)\,\hat{U}_+(t = \pi/\Omega)\,|\downarrow, 0\rangle_{\hat{U}} \\ &= \hat{U}_-(t = 2\pi/\Omega)\left(\frac{1}{\sqrt{2}}\,|\downarrow, 0\rangle_{\hat{U}} + \frac{1}{\sqrt{2}}\,|\uparrow, 1\rangle_{\hat{U}}\right) \qquad (6.5)\\ &= \frac{1}{\sqrt{2}}\,|\downarrow, 0\rangle_{\hat{U}} + \frac{1}{\sqrt{2}}\,|\downarrow, 2\rangle_{\hat{U}} \qquad (6.6)\end{aligned}$$

resulting in the equal superposition of the two squeezed Fock states $|0\rangle_{\hat{U}}$ and $|2\rangle_{\hat{U}}$. To analyse this state the Hamiltonian $\hat{H}_+$ is applied afterwards for a given amount of time and subsequently the spin state is read out. The result is given in figure 6.4, which shows the beat of the two Rabi frequencies from the two components of the state. From the fit the populations are derived as shown in figure 6.5, which clearly show equally populated states $|0\rangle_{\hat{U}}$ and $|2\rangle_{\hat{U}}$. To our knowledge this demonstrates a squeezed Fock state superposition state for the first time.

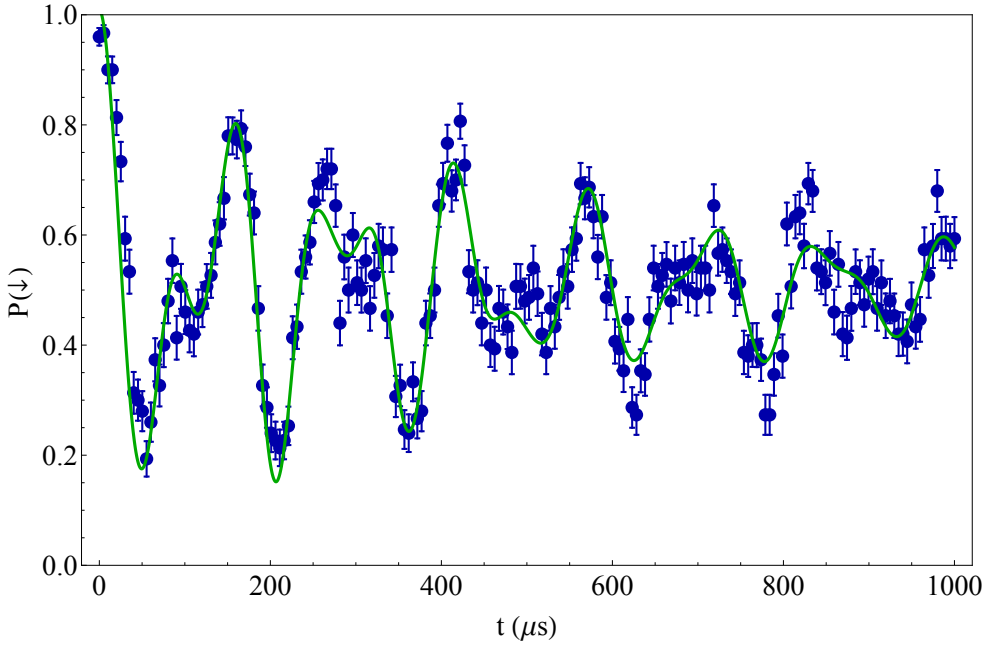

Figure 6.4: Data and fit for $\hat{H}_+$ acting on the superposition state $|\psi\rangle = (|\downarrow, 0\rangle_{\hat{U}} + |\downarrow, 2\rangle_{\hat{U}})/\sqrt{2}$ analysed using $\hat{H}_+$. The fit is performed as described in section 5.2.4.

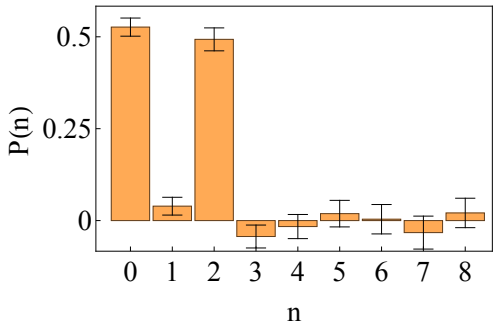

Figure 6.5: Populations for the squeezed Fock state superposition, retrieved from the fit shown in figure 6.4. Within error bounds equal populations of states $|0\rangle_{\hat{U}}$ and $|2\rangle_{\hat{U}}$ can be seen.

Chapter 7

Summary and Outlook

7.1 Summary

In many physical systems, which are used to explore the quantum domain, dissipative processes are a major cause for the decoherence of quantum states. While dissipation generally degrades control, in the experiments that were described in chapter 5, dissipation is turned into something useful. Following [CPBZ93] we used dissipative state preparation to create harmonic oscillator state superpositions of the motion of a trapped $^{40}Ca^{+}$ ion.
Traditional methods to prepare harmonic oscillator state superpositions rely on cooling the harmonic oscillator to its ground state followed by coherent operations. The oscillator is always coupled to its natural environment (typically a thermal bath), which leads to a constant decay of the oscillator's state into a thermal state, necessitating fast coherent operations to create the state.
Dissipative state preparation uses a different approach to create the desired states. Artificial dissipation in form of an effective zero temperature bath is combined with tailored spin-oscillator couplings to drive the system into the desired state. If this process is dominant over any coupling to the natural environment, it engineers the new pointer state of the system to match the desired state, making it the steady state of the process. Contrary to traditional methods, with this technique the initial state and the trajectory over which the state reaches the desired state will not matter for the final state. Once the desired state is reached it will not decay into a thermal state as long as the pumping process is in place. This is a useful feature, as quantum state superpositions are fragile constructs. Using this technique we were able to prepare squeezed, coherent and displaced squeezed states of an ion's motion.

From the structure of the coherent couplings used in the dissipative state preparation we devised novel spin-oscillator couplings, which operate directly in the eigenbasis of the prepared states. These were used for the analysis of the prepared states, enabling a phase sensitive measurement. This allowed to give

a lower bound on the fidelities of the created states with a fidelity of 0.90(2) for a coherent state with a displacement of $|\alpha| = 2.00(1)$ and a fidelity of 0.88(2) for a vacuum squeezed state with squeezing amplitude of $r = 1.45(3)$.
A second use of the new spin-oscillator couplings is the manipulation of the created states. With only two simple experiments, which were described in chapter 6, states could be formed that were never prepared before with trapped ions, and to our knowledge also not in any other system.

These new tools, dissipative state preparation and the spin-motion couplings for the manipulation of harmonic oscillator states, will allow for a number of exciting experiments. The tools for manipulating oscillator states will enable complex analysis and manipulation of these states in the future. The dissipative tools are a stepping stone towards investigations of dissipative systems. Some future possibilities are sketched as an outlook in the following section.

An alternative method, specifically addressing the analysis of squeezed states of motion was implemented. Using a spin-state dependent force common in trapped ions, the phase and quadratures of the squeezed states could be measured. This also lead to a new type of 'Schrödinger's cat'-like states. The motional wavepacket of an ion is split and pulled apart, creating the 'Schrödinger's cat' state. The two different positions of the wavepacket halves then resemble the dead and alive 'states' of Schrödinger's cat. In our version, instead of a motional ground state used as a starting state, we used squeezed states. This lead to 'squeezed Schrödinger's cat' states [LKdC$^+$15, Lo].

A major focus in the field of trapped ion quantum information lies in scaling trapped ions systems to larger numbers of qubits. The proposal of Wineland *et al.* [WMI$^+$98] for a large scale trapped ion quantum computer relies on linear ion crystals composed of two ion species moved in segmented trap arrays.
The trap built as part of this thesis and described in chapter 3 follows this proposal, with a main goal to provide improved control over mixed-species ion crystals and to have multiple connected trap zones. It is a segmented linear trap with two zones optimized for shuttling and splitting of ion crystals, which connect three zones dedicated for interactions. The trap was simulated and designed to simultaneously trap $^{40}Ca^+$ and $^9Be^+$ ions. To address the issues that mixed species ion crystals are affected worse by electrical stray fields the trap features dedicated segmented bias electrodes to provide best control to null stray fields along the full trap.
All Paul traps suffer from anomalous heating of the ion's motion, making the value of the heating rate an important benchmark for the quality of a trap. The measured heating rate of 10 quanta/s for a $^{40}Ca^+$ ion at a motional trap frequency of $\omega_m = 2\pi \times 2\,\mathrm{MHz}$ is low for the trap's dimensions, with an electrode-ion distance of $\simeq 180\,\mu\mathrm{m}$. This value is slightly undermined by an increased motional dephasing time of 32(3) ms for the Fock state superposition $(|0\rangle + |1\rangle)/\sqrt{2}$, which to date we cannot explain.

7.2 Outlook

The experiments performed as part of this thesis provide a new set of techniques for controlling and analyzing harmonic oscillator states. By expanding the system size and complexity and using the same techniques stabilization of other types of quantum states are possible, as are experiments that investigate the nature of dissipation itself. In the following I make a number of new proposals based on these techniques, which would extend the current work. Section 7.2.4 discusses the needed changes to the setup to cool the trap with LN_2.

7.2.1 Determination of the Wigner Function by Measurement in the Displaced Number State Basis

To reconstruct the Wigner function $W(\alpha)$ a convenient approach is to determine the populations of the displaced number states $|k\rangle_\alpha$, defined as

$$Q_k(\alpha) = \langle k|_\alpha \hat{\rho} |k\rangle_\alpha \tag{7.1}$$

for the kth state, with the displacement α and the motional density matrix of the ion $\hat{\rho}$. Leibfried *et al.* [LMK$^+$96] rely on a two-step process, where first the ion being in an initial motional state of interest is displaced with an electric field by $-\alpha$ and then the energy eigenstate populations are measured with the blue-sideband method as described in section 5.2.2. The populations $Q_k(\alpha)$ of the initial state are then equal to the energy eigenstates after the displacement. The value of the Wigner function for the phase space coordinate α is then given by [MCK93]

$$W(\alpha) = \frac{2}{\pi} \sum_{k=0}^{\infty} (-1)^k Q_k(\alpha). \tag{7.2}$$

In the experiment the sum will be truncated at a certain level. Repeating the experiment for different values of α gives data for a desired region of phase space.
In experiments where the phase of the motional state is defined by the phase of a laser as in our experiments, it can be hard to get a stable phase relation to electrical signals due to drifts of the optical path length. In these cases an analysis solely based on this laser would be preferred. Similar to [CLGR$^+$12] our proposed approach uses a Hamiltonian which is only based on the spin-motion interaction. By using the Hamiltonian $\hat{H}_+$ in its form for a coherent state given by the displacement α

$$\hat{H}_\alpha = \hbar\Omega \left(\hat{a}^\dagger - \alpha \mathbb{1}_m \right) \hat{\sigma}_+ + \text{h.c.}. \tag{7.3}$$

we can directly probe for the populations $Q_k(\alpha)$ without any displacement relying on electric fields. This is equivalent to a measurement in the displaced number state basis, again utilizing the new concepts described in section 2.5.3. The same technique could be used with the squeezed displaced basis. This could possibly reach higher signal-to-noise ratios for one phase space axis (with the expense of reduced resolution in the second axis) using the same number of measurements and number state truncation as for the coherent state basis. This could find usage when characterising states where one axis is of major interest, e.g. for *Schrödinger cat states*.

7.2.2 Engineering Multiple Reservoirs

The dissipative state preparation experiments described in this thesis make use of a single engineered reservoir. By increasing the number of reservoirs it is possible to prepare and stabilize more complex states, two of which are described in the sections below.
To introduce multiple reservoirs more modes of motion are needed. One solution is to use the radial modes of a single ion in addition to the axial mode. This would require an amplitude stabilization of the rf drive of the trap, as the fluctuations of the amplitude broaden the linewidth of the radial modes and lead to long-term drifts. This stabilization is currently under development. A second approach lies in adding mode ions, thus increasing the number of axial modes. This choice also has a second advantage. By adding a $^9Be^+$ ion as second ion, the reservoirs could be driven simultaneously, due to the different wavelengths addressing the spin of $^{40}Ca^+$ and $^9Be^+$.

Multimode Squeezed States

Squeezing two modes of motion would create an entangled state in a continuous-variable system, which is not a well studied domain in ion trap physics. The entanglement also makes it one of the fundamental building blocks for continuous-variable quantum computing [GKP01, BvL05]. Here we consider the definition of a two-mode squeezed state version of the two-mode vacuum squeezed state[1] is given by [CS85]

$$\hat{S}_2(\xi)\,|0\rangle_a\,|0\rangle_b \tag{7.4}$$

with the ground states of the two motional modes a and b being $|0\rangle_a$ and $|0\rangle_b$ and the two-mode squeezing operator with the complex squeezing parameter defined as $\xi = r\exp(i\theta)$ defined as

$$\hat{S}_2(\xi) = \exp\left(r\,\hat{a}\,\hat{b}\,e^{2i\theta} + r\,\hat{a}^\dagger\,\hat{b}^\dagger e^{-2i\theta}\right), \tag{7.5}$$

[1] The two mode squeezed state is not defined consistently across literature. See Bishop and Vourdas [BV88] for a unified definition.

and the destruction (creation) operators for the two modes of motion $\hat{a}$ and $\hat{b}$ ($\hat{a}^\dagger$ and $\hat{b}^\dagger$). Using the same recipe as in 2.5.2 the operators we need to implement are given by

$$\hat{K}_a = \hat{S}_2(\xi)\,\hat{a}\,\hat{S}_2^\dagger(\xi) \tag{7.6}$$
$$\hat{K}_b = \hat{S}_2(\xi)\,\hat{b}\,\hat{S}_2^\dagger(\xi), \tag{7.7}$$

which leads to [CS85]

$$\hat{K}_a = \hat{a}\,\cosh(r) + \hat{b}^\dagger\,e^{2i\theta}\sinh(r) \tag{7.8}$$
$$\hat{K}_b = \hat{b}\,\cosh(r) + \hat{a}^\dagger\,e^{2i\theta}\sinh(r). \tag{7.9}$$

With this its clear that the following two Hamiltonians need to be implemented

$$\hat{H}_1 = \hbar\,\Omega\,\hat{\sigma}_+\,\left(\hat{a}\,\cosh(r) + \hat{b}^\dagger\,e^{2i\theta}\sinh(r)\right) + \text{h.c.} \tag{7.10}$$
$$\hat{H}_2 = \hbar\,\Omega\,\hat{\sigma}_+\,\left(\hat{b}\,\cosh(r) + \hat{a}^\dagger\,e^{2i\theta}\sinh(r)\right) + \text{h.c.} \tag{7.11}$$

These would be combined with the same optical pumping as in the experiments described in chapter 5. This can be implemented as a pulsed method, by repeating cycles of the four pulses $\hat{H}_1$, *optical pumping*, $\hat{H}_2$, *optical pumping*. This way only one ion and only one pseudo-spin would be needed. Using a $^{40}Ca^+$ ion with two motional modes and the quadrupole transition as pseudo-spin this would require four different phase-synchronous laser frequencies, which we can produce with the new DDS system of our experiment.
Verification of the created states could be performed similar to the analysis in the engineered basis (see section 5.2.3) by applying one of the Hamiltonians

$$\hat{\tilde{H}}_1 = \hbar\,\Omega\,\hat{\sigma}_-\,\left(\hat{a}\,\cosh(r) + \hat{b}^\dagger\,e^{2i\theta}\sinh(r)\right) + \text{h.c.} \tag{7.12}$$
$$\hat{\tilde{H}}_2 = \hbar\,\Omega\,\hat{\sigma}_-\,\left(\hat{b}\,\cosh(r) + \hat{a}^\dagger\,e^{2i\theta}\sinh(r)\right) + \text{h.c.}. \tag{7.13}$$

Stabilizing Schrödinger-Cat States

De Matos Filho and Vogel [dMFV96] proposed a scheme to stabilize 'Schrödinger cat' superposition states by reservoir engineering. The scheme uses spin dissipation combined with the Hamiltonian

$$\hat{H}_{\text{cat}} = \hbar\,\Omega\,\left(\hat{a}^{\,2} + \alpha^2\,\mathbb{1}_m\right)\,\hat{\sigma}_+ + h.c. \tag{7.14}$$

to stabilize the motional state superposition $|\psi\rangle = 1/\sqrt{2}(|\alpha\rangle + |-\alpha\rangle)$, where $|\alpha\rangle\,(|-\alpha\rangle)$ is the motional ground state displaced by $\alpha(-\alpha)$. The use of second order sidebands in the Hamiltonian makes the used of $^{40}Ca^+$ with the quadrupole transition used for the pseudo-spin challenging, as its small Lamb-Dicke parameter leads to a strong suppression. For this reason an implementation either with a pseudo-spin implemented in the two $S_{1/2}$ Zeeman levels of

$^{40}Ca^+$ or the usage of $^9Be^+$ makes this more feasible. A problem of the scheme is that the Hamiltonian $\hat{H_{\text{cat}}}$ has two degenerate dark states

$$\left|\psi^+\right\rangle = \frac{1}{\sqrt{2}}\left(|\alpha\rangle + |-\alpha\rangle\right) \text{ and } \left|\psi^-\right\rangle = \frac{1}{\sqrt{2}}\left(|\alpha\rangle - |-\alpha\rangle\right). \tag{7.15}$$

These describe a 'positive' and a 'negative' cat state, as they are eigenstates of the photon number parity operator $\mathcal{P}$

$$\mathcal{P}\left|\psi^\pm\right\rangle = \pm\left|\psi^\pm\right\rangle \quad \text{with} \quad \mathcal{P} = \exp\left(i\pi\hat{a}^\dagger\,\hat{a}\,\right). \tag{7.16}$$

The degeneracy would lead to a mixed state as the final state of the pumping process, whose populations would depend on the initial state and the influence of the natural environment during the pumping. Our proposal is a possible counter to this issue, by introducing a second reservoir, which 'pumps' the state to the correct parity. Assume that we start with the state[2]

$$|\psi_0\rangle = \frac{1}{\sqrt{2}}\,|\downarrow\rangle\left(a\left|\psi^+\right\rangle + b\left|\psi^-\right\rangle\right) \tag{7.17}$$

with a and b being complex numbers and $\sqrt{|a|^2+|b|^2} = 1$. Now applying a $\pi/2$ carrier rotation gives

$$|\psi_1\rangle = \frac{1}{\sqrt{2}}\,|+\rangle\left(a\left|\psi^+\right\rangle + b\left|\psi^-\right\rangle\right) \tag{7.18}$$

with $|+\rangle = 1/\sqrt{2}\,(|\downarrow\rangle + |\uparrow\rangle)$ $(|-\rangle = 1/\sqrt{2}\,(|\downarrow\rangle - |\uparrow\rangle))$.
A far detuned Jaynes-Cummings Hamiltonian can be written as [HR06]

$$\hat{H}_{\text{JC}} = \hbar\,\frac{\Omega^2}{4\delta}\,\hat{\sigma}_z\,\hat{a}^\dagger\,\hat{a} \text{ with } \delta \gg \Omega, \tag{7.19}$$

with δ the detuning from resonance and Ω the Rabi frequency on resonance. Since $\hat{a}^\dagger\,\hat{a}$ is proportional to the photon number operator and with the property of the cat state $|\psi^+\rangle(|\psi^-\rangle)$ having even (odd) number of photons, this Hamiltonian may be used to entangle the two cat states with the spin[3]. Applying this Hamiltonian to the state $|\psi_1\rangle$ for a time $t = 4\pi\delta/\Omega^2$ gives

$$|\psi_2\rangle = \frac{1}{\sqrt{2}}\left(a\,|+\rangle\left|\psi^+\right\rangle + b\,|-\rangle\left|\psi^-\right\rangle\right). \tag{7.20}$$

[2]Here a superposition state is used as an example to lay out the scheme. The experiment will deal with the mixed state

$$\rho = |\downarrow\rangle * \left(a_{++}\left|\psi^+\right\rangle\left\langle\psi^+\right| + a_{+-}\left|\psi^+\right\rangle\left\langle\psi^-\right| + a_{-+}\left|\psi^-\right\rangle\left\langle\psi^+\right| + a_{--}\left|\psi^-\right\rangle\left\langle\psi^-\right|\right),$$

with random amplitudes a.

[3]This method is based on [LD97] and was heavily used in cavity quantum electrodynamics. An introduction is given in [HR06]

Subsequently applying a second $\pi/2$ pulse

$$|\psi_3\rangle = \frac{1}{2}\left(a\,|\downarrow\rangle\,\left|\psi^+\right\rangle + b\,|\uparrow\rangle\,\left|\psi^-\right\rangle\right) \tag{7.21}$$

Now that the motional states of different parity are correlated with a different spin state, it is possible to flip the parity of one to match the other. For this several options exist. One is sketched in the following.
With the action of the destruction operator $\hat{a}$ on the coherent state $|\alpha\rangle$ is given by

$$\hat{a}\ |\pm\alpha\rangle = \pm\alpha\,|\pm\alpha\rangle\,, \tag{7.22}$$

it follows that

$$\hat{a}\ \left|\psi^\pm\right\rangle = \alpha\,\left|\psi^\mp\right\rangle. \tag{7.23}$$

Thus, by making use of a red sideband π-pulse on the $S_{-1/2} \leftrightarrow D_{+3/2}$ transition we are able to flip the parity of the motional state. This results in

$$|\psi_4\rangle = \frac{1}{2}\left(|\downarrow\rangle\,a\,\left|\psi^+\right\rangle + b\ |\downarrow_2\rangle\,\left|\psi^+\right\rangle\right), \tag{7.24}$$

with $|\downarrow_2\rangle$ denoting the internal $S_{-1/2}$ state. Subsequently the the optical pumping is used to reset the internal state to $|\downarrow\rangle$ and the cat state pumping can be continued. Interleaving cat-state pumping pulses and parity pumping will produce

$$|\psi_{\text{final}}\rangle = |\downarrow\rangle\,\left|\psi^+\right\rangle \tag{7.25}$$

as the steady state of the system. We note that an identical scheme has been independently proposed in the context of cavity QED, published in [RLS$^+$15]. [LKK$^+$15]

7.2.3 Coupling of a Quantum System to a Reservoir

Along the lines of section 7.2.2 adding more ions also allows to study the coupling of systems. Here non-Markovian dynamics could be studied with one system representing a reservoir to the other system. More complex models of noise and decoherence could be investigated. It would also allow the study of the measurement processes in quantum mechanics and the role of pointer states, as the coupling of a reservoir to a quantum system and the memory time of the reservoir can be tuned, thereby crossing the quantum-classical boundary. A similar experiment has recently been performed with superconducting qubits by Raftery *et al.* [RSS$^+$14].
The basic framework of these experiments would be to use the engineered, motional mode as a reservoir and coupling the spin of a second ion to it. This

is analogous to cavity quantum electro dynamics (CQED). Here the motional mode represents the cavity, the engineered dissipation the reflectivity of the cavity mirrors and the coupling of the spin to the motional mode the coupling strength of the cavity to the atom. Contrary to CQED experiments all of these parameters can be changed in situ. In CQED a new experimental setup (different mirror coatings, different cavity design) would be needed. Even the implementation of multiple 'cavities' should be possible by adding a second reservoir on another motional mode. A first experiment could be the coupling of a spin to a squeezed reservoir as proposed in [Gar86]. To use the reservoir engineering for the implementation of this experiment was suggested by Poyatos *et al.* [PCZ96]. The experiment was realized with superconducting qubits by Murch *et al.* [MWB$^+$13], and even the experiment described in section 5.2.7 and [LKdC$^+$15] addresses this topic to some part, but no full investigation with atomic systems has been realized yet.

7.2.4 Nitrogen Cooling of the Trap

To reduce the heating rate of the trap the possibility of LN_2 cooling could be pursued. If this would have a positive effect on the the increased motional dephasing (section 4.7) is not clear. The following describes necessary technical changes. As this was a considered option in the design phase of the experiment there are already principal ideas for implementation. The top flange of the vacuum can has a free CF40 port for the attachment of a cold finger. With the Janis ST-400 flow cryostat[4] in mind, there are probably other possibilities for a cold finger. The cold finger needs then to be thermally contacted to the aluminum trap mount. The Al base of the trap mount should be replaced with a material of low heat conductivity, e.g. PEEK. One issue arising is the heat load from the atomic source ovens. Further insulation of these parts or independent mounting to the vacuum can might be necessary. For the thermal contact of the cold finger to the trap mount copper braid is recommended to reduce vibrations from the coldhead coupling to the trap. Also the vacuum connection of the cold head to the top flange should be made with an edge welded bellow, similar to those used on the imaging system.

[4] ST-400 Ultra High Vacuum (UHV) Cryostat from Janis Research (www.janis.com)

Appendix A

Appendix

A.1 Abbreviations

AOM	Acousto-optic modulator
dc	Direct current, also used as a synonym for static voltages (see footnote on page 11)
DI water	Deionized water
DDS	Direct digital synthesizer
DSP	Dissipative state preparation
DSS	Displaced squeezed state
EOM	Electro-optic modulator
FWHM	Full width half maximum
LN_2	Liquid nitrogen
NIR	Near infra-red
PTFE	Polytetrafluoroethylene, also: teflon
qccd	Quantum charge-coupled device
rms	Root mean square
rf	Radio frequency
SDF	State dependent force
UHV	Ultra high vacuum
UV	Ultra violet

Bibliography

[ABLW11] J. M. Amini, J. Britton, D. Leibfried, and D. J. Wineland, *Micro-fabricated chip traps for ions*, pp. 395–420, Wiley-VCH Verlag GmbH & Co. KGaA, 2011.

[AEM+95] M. H. Anderson, J. R. Ensher, M. R. Matthews, C. E. Wieman, and E. A. Cornell, *Observation of Bose-Einstein condensation in a dilute atomic vapor*, Science **269** (1995), no. 5221, 198–201.

[AGH+11] D. Allcock, L. Guidoni, T. P. Harty, C. Ballance, M. Blain, A. Steane, and D. Lucas, *Reduction of heating rate in a microfabricated ion trap by pulsed-laser cleaning*, New J. Phys. **13** (2011), 123023.

[AGMO76] G. Alzetta, A. Gozzini, L. Moi, and G. Orriols, *An experimental method for the observation of r.f. transitions and laser beat resonances in oriented Na vapour*, Il Nuovo Cimento B Series 11 **36** (1976), no. 1, 5–20 (English).

[ALKH13] J. Alonso, F. M. Leupold, B. C. Keitch, and J. P. Home, *Quantum control of the motional states of trapped ions through fast switching of trapping potentials*, New Journal of Physics **15** (2013), no. 2, 023001.

[BDS+03] M. D. Barrett, B. DeMarco, T. Schaetz, D. Leibfried, J. Britton, J. Chiaverini, W. M. Itano, B. Jelenkovic, J. D. Jost, C. Langer, T. Rosenband, and D. J. Wineland, *Sympathetic cooling of Be^+ and Mg^+ for quantum logic*, Phys. Rev. A **68** (2003), no. 042302.

[Ben95] C. H. Bennett, *Quantum information and computation*, Physics Today (1995), 24–30.

[BGL+12] R. Bowler, J. Gaebler, Y. Lin, T. R. Tan, D. Hanneke, J. D. Jost, J. P. Home, D. Leibfried, and D. J. Wineland, *Coherent diabatic ion transport and separation in a multizone trap array*, Phys. Rev. Lett. **109** (2012), 080502.

[BHW+04] A. Blais, R.-S. Huang, A. Wallraff, S. M. Girvin, and R. J. Schoelkopf, *Cavity quantum electrodynamics for superconducting electrical circuits: An architecture for quantum computation*, Phys. Rev. A **69** (2004), 062320.

[Bla10] R. B. Blakestad, *Transport of trapped-ion qubits within a scalable quantum processor*, Ph.D. thesis, University of Colorado, 2010.

[BMB+98] D. J. Berkeland, J. D. Miller, J. C. Bergquist, W. M. Itano, and D. J. Wineland, *Minimization of ion micromotion in a Paul trap*, Journal of Applied Physics **83** (1998), no. 10, 5025–5033.

[BP02] H.-P. Breuer and F. Petruccione, *The theory of open quantum systems*, Oxford University Press, 2002.

[BV88] R. Bishop and A. Vourdas, *General two-mode squeezed states*, Zeitschrift für Physik B Condensed Matter **71** (1988), no. 4, 527–529 (English).

[BvL05] S. Braunstein and P. van Loock, *Quantum information with continuous variables*, Rev. Mod. Phys. **77** (2005), 513.

[CBPZ93] J. I. Cirac, R. Blatt, A. S. Parkins, and P. Zoller, *Preparation of fock states by observation of quantum jumps in an ion trap*, Phys. Rev. Lett. **70** (1993), 6.

[CHK+10] C. W. Chou, D. B. Hume, J. C. J. Koelemeij, D. J. Wineland, and T. Rosenband, *Frequency comparison of two high-accuracy Al^+ optical clocks*, Phys. Rev. Lett. **104** (2010), 070802.

[CLGR+12] J. Casanova, C. López, J. García-Ripoll, C. Roos, and E. Solano, *Quantum tomography in position and momentum space*, The European Physical Journal D **66** (2012), no. 8 (English).

[CMdMFD01] A. R. R. Carvalho, P. Milman, R. L. de Matos Filho, and L. Davidovich, *Decoherence and pointer engineering and quantum state protection*, Phys. Rev. Lett. **86** (2001), 22.

[CPBZ93] J. I. Cirac, A. S. Parkins, R. Blatt, and P. Zoller, *"dark" squeezed states of the motion of a trapped ion*, Phys. Rev. Lett. **70** (1993), 556–559.

[CS85] C. M. Caves and B. L. Schumaker, *New formalism for two-photon quantum optics. i. quadrature phases and squeezed states*, Phys. Rev. A **31** (1985), 3068–3092.

[DBMM04] L.-M. Duan, B. B. Blinov, D. L. Moehring, and C. Monroe, *Scalable trapped ion quantum computation with a probabilistic ion-photon mapping*, quant-ph/0401020.

[Deh68] H. Dehmelt, *Radiofrequency spectroscopy of stored ions i: Storage*, Advances in Atomic and Molecular Physics, vol. 3, Academic Press, 1968, pp. 53 – 72.

[Deu85] D. Deutsch, *Quantum theory and the Church-Turing principle and the universal quantum computer*, Proc. R. Soc. Lond. A **400** (1985), 97–117.

[DFV00] C. Di Fidio and W. Vogel, *Damped rabi oscillations of a cold trapped ion*, Phys. Rev. A **62** (2000), 031802.

[DHK+83] R. Drever, J. Hall, F. Kowalski, J. Hough, G. Ford, A. Munley, and H. Ward, *Laser phase and frequency stabilization using an optical resonator*, Applied Physics B **31** (1983), 97–105 (English).

[Die82] D. Dieks, *Communication by EPR devices*, Physics Letters A **92** (1982), no. 6, 271 – 272.

[Dir28] P. A. M. Dirac, *The quantum theory of the electron*, Proceedings of the Royal Society of London A: Mathematical, Physical and Engineering Sciences **117** (1928), no. 778, 610–624.

[DMA+95] K. B. Davis, M. O. Mewes, M. R. Andrews, N. J. van Druten, D. S. Durfee, D. M. Kurn, and W. Ketterle, *Bose-Einstein condensation in a gas of sodium atoms*, Phys. Rev. Lett. **75** (1995), 3969–3973.

[dMFV96] R. L. de Matos Filho and W. Vogel, *Even and odd coherent states of the motion of a trapped ion*, Phys. Rev. Lett. **76** (1996), 608–611.

[DMK+08] S. Diehl, A. Micheli, A. Kantian, B. Kraus, H. Büchler, and P. Zoller, *Quantum states and phases in driven open quantum systems with cold atoms*, Nature Physics **4** (2008), 878.

[DMN13] S. J. Devitt, W. J. Munro, and K. Nemoto, *Quantum error correction for beginners*, Reports on Progress in Physics **76** (2013), no. 7, 076001.

[DNM+11] N. Daniilidis, S. Narayanan, S. A. Möller, R. Clark, T. E. Lee, P. J. Leek, A. Wallraff, S. Schulz, F. Schmidt-Kaler, and H. Häffner, *Fabrication and heating rate study of microscopic surface electrode ion traps*, New Journal of Physics **13** (2011), no. 1, 013032.

[DOS+06] L. Deslauriers, S. Olmschenk, D. Stick, W. K. Hensinger, J. Sterk, and C. Monroe, *Scaling and suppression of anomalous heating in ion traps*, Phys. Rev. Lett. **97** (2006), 103007.

[Fey82] R. P. Feynman, *Simulating physics with computers*, International Journal of Theoretical Physics **21** (1982), 467.

[Fis13] K. Fisher, *Coherent control laser system for the quantum state manipulation of trapped ions*, Master's thesis, Eidgenössische Technische Hochschule Zürich, 2013.

[Flü14] C. Flühmann, *Stabilizing laser and magnetic fields for quantum information experiments*, Master's thesis, Eidgenössische Technische Hochschule Zürich, 2014.

[Gar86] C. W. Gardiner, *Inhibition of atomic phase decays by squeezed light: A direct effect of squeezing*, Phys. Rev. Lett. **56** (1986), 1917–1920.

[GKP01] D. Gottesman, A. Kitaev, and J. Preskill, *Encoding a qubit in an oscillator*, Phys. Rev. A **64** (2001), 012310.

[GLM06] V. Giovannetti, S. Lloyd, and L. Maccone, *Quantum metrology*, Phys. Rev. Lett. **96** (2006), 010401.

[GLM11] ———, *Advances in quantum metrology*, Nat Photon **5** (2011), no. 4, 222–229.

[GME+02] M. Greiner, O. Mandel, T. Esslinger, T. W. Haensch, and I. Bloch, *Quantum phase transition from a superfluid to a mott insulator in a gas of ultracold atoms*, Nature **415** (2002), 39–44.

[GMM+08] K. Goda, O. Miyakawa, E. E. Mikhailov, S. Saraf, R. Adhikari, K. McKenzie, R. Ward, S. Vass, A. J. Weinstein, and N. Mavalvala, *A quantum-enhanced prototype gravitational-wave detector*, Nat Phys **4** (2008), no. 6, 472–476.

[GRB+01] S. Gulde, D. Rotter, P. Barton, F. Schmidt-Kaler, R. Blatt, and W. Hogervorst, *Simple and efficient photoionization loading of ions for precision ion-trapping experiments*, Appl. Phys. B **73** (2001), 861.

[GT07] N. Gisin and R. Thew, *Quantum communication*, Nat Photon **1** (2007), no. 3, 165–171.

[Hab12] R. Hablutzel, *Novel atom sources and ultrafast electronic switches for trapped-ion quantum information experiments*, Master's thesis, Eidgenössische Technische Hochschule Zürich, 2012.

[HAB+14] T. P. Harty, D. T. C. Allcock, C. J. Ballance, L. Guidoni, H. A. Janacek, N. M. Linke, D. N. Stacey, and D. M. Lucas, *High-fidelity preparation, gates, memory, and readout of a trapped-ion quantum bit*, Phys. Rev. Lett. **113** (2014), 220501.

[Hah50] E. L. Hahn, *Spin echoes*, Phys. Rev. **80** (1950), 580–594.

[HCW+12] D. A. Hite, Y. Colombe, A. C. Wilson, K. R. Brown, U. Warring, R. Jördens, J. D. Jost, K. S. McKay, D. P. Pappas, D. Leibfried, and D. J. Wineland, *100-fold reduction of electric-field noise in an ion trap cleaned with In Situ argon-ion-beam bombardment*, Phys. Rev. Lett. **109** (2012), 103001.

[Hem14] C. Hempel, *Digital quantum simulation, schrödinger cat state spectroscopy and setting up a linear ion trap*, Ph.D. thesis, Leopold-Franzens-Universität Innsbruck, 2014.

[HHJ+09] J. P. Home, D. Hanneke, J. D. Jost, J. M. Amini, D. Leibfried, and D. J. Wineland, *Complete methods set for scalable ion trap quantum information processing*, Science **325** (2009), 1227.

[Hom06] J. P. Home, *Entanglement of two trapped-ion spin qubits*, Ph.D. thesis, Oxford University, 2006.

[Hom13] ———, *Chapter 4 - quantum science and metrology with mixed-species ion chains*, Advances in Atomic, Molecular, and Optical Physics (P. R. B. Ennio Arimondo and C. C. Lin, eds.), Advances In Atomic, Molecular, and Optical Physics, vol. 62, Academic Press, 2013, pp. 231 – 277.

[HR06] S. Haroche and J.-M. Raimond, *Exploring the quantum: Atoms and cavities and photons*, Oxford University Press, (2006).

[HS75] T. W. Haensch and A. L. Schawlow, *Cooling of gases by laser radiation*, Optics Communications **13** (1975), no. 1, 68 – 69.

[HS06] J. P. Home and A. Steane, *Electrode configurations for fast separation of trapped ions*, Quantum Information and Computation **6** (2006), 289.

[IHBW90] W. M. Itano, D. J. Heinzen, J. J. Bollinger, and D. J. Wineland, *Quantum zeno effect*, PhysRevA **41** (1990), 2295.

[IW82] W. M. Itano and D. J. Wineland, *Laser cooling of ions stored in harmonic and penning traps*, Phys. Rev. A **25** (1982), 35–54.

[JLH+14] P. Jurcevic, B. P. Lanyon, P. Hauke, C. Hempel, P. Zoller, R. Blatt, and C. F. Roos, *Quasiparticle engineering and entanglement propagation in a quantum many-body system*, Nature **511** (2014), no. 7508, 202–205.

[Jos10] J. D. Jost, *Entangled mechanical oscillators*, Ph.D. thesis, University of Colorado, 2010.

[KBD+08] B. Kraus, H. P. Büchler, S. Diehl, A. Kantian, A. Micheli, and P. Zoller, *Preparation of entangled states by quantum markov processes*, Phys. Rev. A **78** (2008), 042307.

[KCW02] D. Kielpinski, C.Monroe, and D. Wineland, *Architecture for a large-scale ion-trap quantum computer*, Nature **417** (2002), 709–711.

[KKM+00] D. Kielpinski, B. E. King, C. J. Myatt, C. A. Sackett, Q. A. Turchette, W. M. Itano, C. Monroe, and D. J. Wineland, *Sympathetic cooling of trapped ions for quantum logic*, Phys. Rev. A **61** (2000), no. 032310.

[KLK+15] D. Kienzler, H.-Y. Lo, B. Keitch, L. de Clercq, F. Leupold, F. Lindenfelser, M. Marinelli, V. Negnevitsky, and J. P. Home, *Quantum harmonic oscillator state synthesis by reservoir engineering*, Science **347** (2015), no. 6217, 53–56.

[KLM+01] H. J. Kimble, Y. Levin, A. B. Matsko, K. S. Thorne, and S. P. Vyatchanin, *Conversion of conventional gravitational-wave interferometers into quantum nondemolition interferometers by modifying their input and/or output optics*, Phys. Rev. D **65** (2001), 022002.

[KMJ+11] H. Krauter, C. A. Muschik, K. Jensen, W. Wasilewski, J. M. Petersen, J. I. Cirac, and E. S. Polzik, *Entanglement generated by dissipation and steady state entanglement of two macroscopic objects*, Phys. Rev. Lett. **107** (2011), 080503.

[KMR+01] D. Kielpinski, V. Meyer, M. A. Rowe, C. A. Sackett, W. M. Itano, C. Monroe, and D. J. Wineland, *A decoherence-free quantum memory using trapped ions*, Science **291** (2001), no. 5506, 1013–1015.

[KRS+14] H. Kaufmann, T. Ruster, C. T. Schmiegelow, F. Schmidt-Kaler, and U. G. Poschinger, *Dynamics and control of fast ion crystal splitting in segmented paul traps*, New Journal of Physics **16** (2014), no. 7, 073012.

[KYG+07] J. Koch, T. M. Yu, J. Gambetta, A. A. Houck, D. I. Schuster, J. Majer, A. Blais, M. H. Devoret, S. M. Girvin, and R. J. Schoelkopf, *Charge-insensitive qubit design derived from the Cooper pair box*, Phys. Rev. A **76** (2007), 042319.

[LAK+14] H.-Y. Lo, J. Alonso, D. Kienzler, B. Keitch, L. de Clercq, V. Negnevitsky, and J. Home, *All-solid-state continuous-wave laser systems for ionization, cooling and quantum state manipulation of beryllium ions*, Applied Physics B **114** (2014), no. 1-2, 17–25 (English).

[Lan05] C. E. Langer, *High fidelity quantum information processing with trapped ions*, Ph.D. thesis, University of Colorado, 2005.

[LB13] D. A. Lidar and T. A. Brun, *Quantum error correction*, Cambridge University Press, 2013.

[LBMW03] D. Leibfried, R. Blatt, C. Monroe, and D. Wineland, *Quantum dynamics of single trapped ions*, Rev. Mod. Phys. **75** (2003), 281–324.

[LD97] L. G. Lutterbach and L. Davidovich, *Method for direct measurement of the wigner function in cavity qed and ion traps*, Phys. Rev. Lett. **78** (1997), 2547–2550.

[Lei14] D. Leibfried, Private communication, 2014.

[LGA+08] J. Labaziewicz, Y. Ge, P. Antohi, D. Leibrandt, K. R. Brown, and I. L. Chuang, *Suppression of heating rates in cryogenic surface-electrode ion traps*, Phys. Rev. Lett. **100** (2008), 013001.

[LGR+13] Y. Lin, J. P. Gaebler, F. Reiter, T. R. Tan, R. Bowler, A. S. Sorensen, D. Leibfried, and D. J. Wineland, *Dissipative production of a maximally entangled steady state of two quantum bits*, Nature **504** (2013), no. 7480, 415–418.

[LGT+13] Y. Lin, J. Gaebler, T. Tan, R. Bowler, J. Jost, D. Leibfried, and D. Wineland, *Sympathetic electromagnetically-induced-transparency laser cooling of motional modes in an ion chain*, Phys. Rev. Lett. **110** (2013), 153002.

[Lin11] F. Lindenfelser, *Laser stabilization for quantum information experiments with trapped ions*, Master's thesis, Eidgenössische Technische Hochschule Zürich, 2011.

[LKdC+15] H.-Y. Lo, D. Kienzler, L. de Clercq, M. Marinelli, V. Negnevitsky, B. Keitch, and J. P. Home, *Spin-motion entanglement and state diagnosis with squeezed oscillator wavepackets*, arxiv:1412.7100 (2015).

[LKK+15] F. Lindenfelser, B. Keitch, D. Kienzler, D. Bykov, P. Uebel, M. A. Schmidt, P. S. J. Russell, and J. P. Home, *An ion trap built with photonic crystal fibre technology*, Review of Scientific Instruments **86** (2015), no. 3, –.

[LMK+96] D. Leibfried, D. M. Meekhof, B. E. King, C. Monroe, W. M. Itano, and D. J. Wineland, *Experimental determination of the motional quantum state of a trapped atom*, Phys. Rev. Lett. **77** (1996), 4281–4285.

[Lo] H.-Y. Lo, *To be published*, Ph.D. thesis, Eidgenössische Technische Hochschule Zürich.

[LRH+04] D. M. Lucas, A. Ramos, J. P. Home, M. J.McDonnell, S. Nakayama, J.-P. Stacey, S. C. W. andD. N. Stacey, and A. M. Steane, *Isotope-selective photo-ionisation for calcium ion trapping*, Phys. Rev. A **69** (2004), 012711.

[Luc12] D. M. Lucas, Private communication, 2012.

[Mar13] M. Marinelli, *Simulations for one ion experiments*, Semester thesis, Eidgenössische Technische Hochschule Zürich, 2013.

[MCK93] H. Moya-Cessa and P. L. Knight, *Series representation of quantum-field quasiprobabilities*, Phys. Rev. A **48** (1993), 2479–2481.

[MJYH94] L.-S. Ma, P. Jungner, J. Ye, and J. L. Hall, *Delivering the same optical frequency at two places: accurate cancellation of phase noise introduced by an optical fiber or other time-varying path*, Optics letters **19** (1994), no. 21, 1777–1779.

[MKT+00] C. J. Myatt, B. E. King, Q. A. Turchette, C. A. S. Kielpinski, W. M. Itano, C. Monroe, and D. J. Wineland, *Decoherence of quantum superpositions through coupling to engineered reservoirs*, Nature **403** (2000), 269–273.

[MKV+09] T. Monz, K. Kim, A. S. Villar, P. Schindler, M. Chwalla, M. Riebe, C. F. Roos, H. Häffner, W. Hänsel, M. Hennrich, and R. Blatt, *Realization of universal ion-trap quantum computation with decoherence-free qubits*, Phys. Rev. Lett. **103** (2009), 200503.

[MMK+95] C. Monroe, D. M. Meekhof, B. E. King, S. R. Jefferts, W. M. Itano, D. J. Wineland, and P. Gould, *Resolved-sideband Raman cooling of a bound atom to the 3D zero-point energy*, Phys. Rev. Lett. **75** (1995), no. 22, 4011.

[MMK+96] D. M. Meekhof, C. Monroe, B. E. King, W. M. Itano, and D. J. Wineland, *Generation of nonclassical motional states of a trapped atom*, Phys. Rev. Lett. **76** (1996), 1796.

[MMKW96] C. Monroe, D. M. Meekhof, B. E. King, and D. J. Wineland, *A Schrödinger cat superposition state of an atom*, Science **272** (1996), 1131.

[MS59] W. Macalpine and R. Schildknecht, *Coaxial resonators with helical inner conductor*, Proceedings of the IRE **47** (1959), no. 12, 2099–2105.

[MSB+11] T. Monz, P. Schindler, J. T. Barreiro, M. Chwalla, D. Nigg, W. A. Coish, M. Harlander, W. Hänsel, M. Hennrich, and R. Blatt, *14-qubit entanglement: Creation and coherence*, Phys. Rev. Lett. **106** (2011), 130506.

[MWB+13] K. W. Murch, S. J. Weber, K. M. Beck, E. Ginossar, and I. Siddiqi, *Reduction of the radiative decay of atomic coherence in squeezed vacuum*, Nature **499** (2013), no. 7456, 62–65.

[MYH08] D. Meiser, J. Ye, and M. J. Holland, *Spin squeezing in optical lattice clocks via lattice-based qnd measurements*, New Journal of Physics **10** (2008), no. 7, 073014.

[Nie97] M. M. Nieto, *Displaced and squeezed number states*, Physics Letters A **229** (1997), no. 3, 135 – 143.

[Nob12] Nobelprize.org, *The nobel prize in physics 2012*, 2012, http://www.nobelprize.org/nobel_prizes/physics/laureates/2012/.

[OSRT13] C. F. Ockeloen, R. Schmied, M. F. Riedel, and P. Treutlein, *Quantum metrology with a scanning probe atom interferometer*, Phys. Rev. Lett. **111** (2013), 143001.

[Pau90] W. Paul, *Electromagnetic traps for charged and neutral particles*, Rev. Mod. Phys. **62** (1990), no. 3, 531–540.

[PCZ96] J. F. Poyatos, J. I. Cirac, and P. Zoller, *Quantum reservoir engineering with laser cooled trapped ions*, Phys. Rev. Lett. **77** (1996), 4728.

[PWC+96] J. F. Poyatos, R. Walser, J. I. Cirac, P. Zoller, and R. Blatt, *Motion tomography of a single trapped ion*, Phys. Rev. A **53** (1996), R1966–R1969.

[Ram98] N. Ramsey, *Spectroscopy with coherent radiation: selected papers of norman ramsey with commentary*, World Scientific and Singapore, 1998.

[RGL+14] P. Richerme, Z.-X. Gong, A. Lee, C. Senko, J. Smith, M. Foss-Feig, S. Michalakis, A. V. Gorshkov, and C. Monroe, *Non-local propagation of correlations in quantum systems with long-range interactions*, Nature **511** (2014), no. 7508, 198–201.

[RLS+15] A. Roy, Z. Leghtas, A. D. Stone, M. Devoret, and M. Mirrahimi, *Continuous generation and stabilization of mesoscopic field superposition states in a quantum circuit*, Phys. Rev. A **91** (2015), 013810.

[Roh09] F. Rohde, *Remote ion traps for quantum networking: Two-photon interference and correlations*, Ph.D. thesis, Universitat Politecnica de Catalunya, 2009.

[Roo00] C. Roos, *Controlling the quantum state of trapped ions*, Ph.D. thesis, Universität Innsbruck, 2000.

[RSS+14] J. Raftery, D. Sadri, S. Schmidt, E. Türeci, H. and A. Houck, A. *Observation of a dissipation-induced classical to quantum transition*, Phys. Rev. X **4** (2014), 031043.

[Sch35] E. Schrödinger, *Die gegenwärtige Situation in der Quantenmechanik*, Naturwissenschaften **23** (1935), no. 48, 807–812 (German), Reprinted in English in [WZ83].

[Sch01] W. Schleich, *Quantum optics in phase space*, Wiley, New York, 2001.

[Sep12] M. Sepiol, *Stabilization of a 729 nm laser to an ultra-high finesse reference cavity*, Master's thesis, Eidgenössische Technische Hochschule Zürich, 2012.

[SHL+13] S. Shankar, M. Hatridge, Z. Leghtas, K. M. Sliwa, A. Narla, U. Vool, S. M. Girvin, L. Frunzio, M. Mirrahimi, and M. H. Devoret, *Autonomously stabilized entanglement between two superconducting quantum bits*, Nature **504** (2013), no. 7480, 419–422.

[Sho94] P. W. Shor, *Polynomial-time algorithms for prime factorisation and discrete logarithms on a quantum computer*, Proceedings of the 35th annual symposium on foundations of computer science, IEEE Computer Society Press, 1994, pp. 124–134.

[Sho95] ———, *Scheme for reducing decoherence in quantum computer memory*, Phys. Rev. A **52** (1995), R2493–6.

[SKEM+01] F. Schmidt-Kaler, J. Eschner, G. Morigi, C. Roos, D. Leibfried, A. Mundt, and R. Blatt, *Laser cooling with electromagnetically induced transparency: application to trapped samples of ions or neutral atoms*, Applied Physics B **73** (2001), no. 8, 807–814 (English).

[SM99] A. Sørensen and K. Mølmer, *Spin-spin interaction and spin squeezing in an optical lattice*, Phys. Rev. Lett. **83** (1999), 2274–2277.

[SM00] A. Sørensen and K. Mølmer, *Entanglement and quantum computation with ions in thermal motion*, Phys. Rev. A **62** (2000), 022311.

[SPM+10] K. Singer, U. Poschinger, M. Murphy, P. Ivanov, F. Ziesel, T. Calarco, and F. Schmidt-Kaler, *Colloquium*, Rev. Mod. Phys. **82** (2010), 2609–2632.

[SRL+05] P. O. Schmidt, T. Rosenband, C. Langer, W. M. Itano, J. C. Bergquist, and D. J. Wineland, *Spectroscopy using quantum logic*, Science **309** (2005), 749–752.

[Ste96] A. M. Steane, *Error correcting codes in quantum theory*, Phys. Rev. Lett. **77** (1996), 793–797.

[TDL+11] J. D. Teufel, T. Donner, D. Li, J. W. Harlow, M. S. Allman, K. Cicak, A. J. Sirois, J. D. Whittaker, K. W. Lehnert, and R. W. Simmonds, *Sideband cooling of micromechanical motion to the quantum ground state*, Nature **475** (2011), no. 7356, 359–363.

[TKK+00] Q. A. Turchette, D. Kielpinski, B. E. King, D. Leibfried, D. M. Meekhof, C. J. Myatt, M. A. Rowe, C. A. Sackett, C. S. Wood, W. M. Itano, C. Monroe, and D. J. Wineland, *Heating of trapped ions from the quantum ground state*, Phys. Rev. A **61** (2000), 063418.

[TMK+00] Q. A. Turchette, C. J. Myatt, B. E. King, C. A. Sackett, D. Kielpinski, W. M. Itano, C. Monroe, and D. J. Wineland, *Decoherence and decay of motional quantum states of a trapped atom coupled to engineered reservoirs*, Phys. Rev. A **62** (2000), 053807.

[VAC+02] D. Vion, A. Aassime, A. Cottet, P. Joyez, H. Pothier, C. Urbina, D. Esteve, and M. H. Devoret, *Manipulating the quantum state of an electrical circuit*, Science **296** (2002), no. 5569, 886–889.

[VWC09] F. Verstraete, M. M. Wolf, and J. I. Cirac, *Quantum computation, quantum state engineering and quantum phase transitions driven by dissipation*, Nature Physics **5** (2009), 633–636.

[WD75] D. J. Wineland and H. G. Demelt, Bull. Am. Phys. Soc. **20** (1975), 637.

[WDW78] D. J. Wineland, R. E. Drullinger, and F. L. Walls, *Radiation-pressure cooling of bound resonant absorbers*, Phys. Rev. Lett. **40** (1978), 1639–1642.

[Web05] S. Webster, *Raman sideband cooling and coherent manipulation of trapped ions*, D.phil̇thesis, Oxford University, 2005.

[Win11] D. J. Wineland, Private communication, 2011.

[WJ06] J. Wrachtrup and F. Jelezko, *Processing quantum information in diamond*, Journal of Physics: Condensed Matter **18** (2006), no. 21, S807.

[WMI+98] D. J. Wineland, C. Monroe, W. M. Itano, D. Leibfried, B. E. King, and D. M. Meekhof, *Experimental issues in coherent quantum-state manipulation of trapped atomic ions*, J. Res. Natl. Inst. Stand. Technol. **103** (1998), 259–328.

[WON+07] F. Waldermann, P. Olivero, J. Nunn, K. Surmacz, Z. Wang, D. Jaksch, R. Taylor, I. Walmsley, M. Draganski, P. Reichart, A. Greentree, D. Jamieson, and S. Prawer, *Creating diamond color centers for quantum optical applications*, Diamond and Related Materials **16** (2007), no. 11, 1887 – 1895.

[Wün91] A. Wünsche, *Displaced fock states and their connection to quasiprobabilities*, Quantum Optics: Journal of the European Optical Society Part B **3** (1991), no. 6, 359.

[WZ82] W. K. Wootters and W. H. Zurek, *A single quantum cannot be cloned*, Nature **299** (1982), no. 5886, 802–803.

[WZ83] J. A. Wheeler and W. H. Zurek, *Quantum theory of measurement*, Princeton University Press, Princeton NJ, 1983.

[Yue76] H. P. Yuen, *Two-photon coherent states of the radiation field*, Phys. Rev. A **13** (1976), 2226–2243.

[Zur91] W. H. Zurek, *Decoherence and the transition from quantum to classical*, Physics Today (1991), 36–44.

[Zur03] W. H. Zurek, *Decoherence, einselection, and the quantum origins of the classical*, Rev. Mod. Phys. **75** (2003), 715–775.

Daniel Kienzler
Burstwiesenstasse 67, 8055 Zürich
danielki@phys.ethz.ch

Curriculum Vitae

Born on 19.03.1983 in Stuttgart, Germany

2003 – 2007	Undergraduate Studies at Humboldt Universität zu Berlin (HUB) in Physics
2007 – 2008	Erasmus Student at Eidgenössische Technische Hochschule Zürich (ETHZ)
2008 – 2009	Work for external Diploma Thesis at ETHZ, Institute for Particle Physics "Characterization, simulation and analysis of data taken with the MAGIC telescope at increased background light levels" supervisors: Prof. Dr. T. Lohse, Prof. Dr. A. Biland
11.2009	Diploma in Physics (dipl. phys.), HUB
03.2010 – 08.2010	Internship at University of Nottingham supervisor: Prof. Dr. Peter Krüger
Since 09.2010	PhD studies at ETHZ, Institute for Quantum Electronics supervisor: Prof. Dr. J. P. Home

Publications

“Quantum harmonic oscillator state synthesis by reservoir engineering“
D. Kienzler, H-Y. Lo, B. Keitch, L. de Clercq, F. Leupold, F. Lindenfelser, M. Marinelli, V. Negnevitsky and J. P. Home.
Science **347** (2015), no. 6217, 53–56

“Spin-motion entanglement and state diagnosis with squeezed oscillator wavepackets“
H.-Y. Lo, D. Kienzler, L. de Clercq, M. Marinelli, V. Negnevitsky, B. Keitch, J. P. Home
arxiv:1412.7100 (2015)

“An ion trap built with photonic crystal fibre technology“
F. Lindenfelser, B. Keitch, D. Kienzler, D. Bykov, P. Uebel, M. A. Schmidt, P. St.J. Russell, J. P. Home
Review of Scientific Instruments **86** (2015), no. 3

"All solid-state continuous-wave laser systems for ionization, cooling and quantum state manipulation of beryllium ions"
H-Y. Lo, J. Alonso, D. Kienzler, B. C. Keitch, L. E. de-Clercq, V. Negnevitsky and J. P. Home
Applied Physics B **114** (2014), no. 1-2, 17–25